Cronfa - Swansea University Open Access Repository

_____

This is an author produced version of a paper published in:
Computer Methods in Applied Mechanics and Engineering

Cronfa URL for this paper:
http://cronfa.swan.ac.uk/Record/cronfa48583

_____

Paper:

Garcia-Blanco, E., Ortigosa, R., Gil, A., Lee, C. & Bonet, J. (2019). A new computational framework for electro-activation in cardiac mechanics. *Computer Methods in Applied Mechanics and Engineering*
http://dx.doi.org/10.1016/j.cma.2019.01.042

A new computational framework for electro-activation in cardiac mechanics

Emilio Garcia-Blanco†, Rogelio Ortigosa†1, Antonio J. Gil†2, Chun Hean Lee†, Javier Bonet‡

†*Zienkiewicz Centre for Computational Engineering, College of Engineering*
Swansea University, Bay Campus, SA1 8EN, United Kingdom

‡*University of Greenwich, London, SE10 9LS, United Kingdom*

Abstract

This paper presents a novel computational framework for the numerical simulation of the electromechanical response of the myocardium during the cardiac cycle. The paper presents the following main novelties. (1) Two new mixed formulations, *tailor-made* for active stress and active strain coupling approaches, have been developed and used in conjunction with two different ionic models, namely Bueno-Orovio [1] and Ten Tusscher [2]. Taking as a reference the mixed formulations introduced by Bonet *et al.* [3] in the context of nonlinear elasticity, the proposed formulations include as unknown fields the geometry and the transmembrane potential (and possibly a Lagrange multiplier enforcing weakly the incompressibility constraint) as well as the deformation gradient tensor, its cofactor, its determinant, the gradient of the transmembrane potential and their respective work conjugates. The Finite Element implementation of these formulations is shown in this paper, where a static condensation procedure is presented in order to yield an extremely competitive computational approach. (2) A comprehensive and rigorous study of different ionic models (i.e Bueno-Orovio and Ten Tusscher) and electromechanical activation couplings (i.e active strain and active stress) has been carried out. (3) An analytical and numerical analysis of the possible loss of ellipticity and polyconvexity of one of the most widely used constitutive models in the context of cardiac mechanics is carried out in this paper, putting forward possible polyconvexifications of the existing model. (4) In addition, an invariant representation of Guccione's constitutive model is proposed. Finally, a series of numerical examples are included in order to demonstrate the applicability and robustness of the proposed formulations.

Keywords: Cardiac electromechanics, Mixed Formulations, Polyconvexity, Finite Elements.

1. Introduction

Cardiovascular diseases, such as heart infarction or dysrhythmia, represent the main cause of death in the world [4–6]. Over the last decade, the computational modelling of the complex physical phenomena occurring in the human heart have become an area of increasing scientific interest as this can aid by: (a) providing augmented simulation-based diagnosis tools for patients or innovative surgery techniques for clinicians; (b) gaining better understanding of the mechanisms driving the behaviour of the cardiac muscle both from the physiological and pathological standpoints.

Three aspects are crucial in order to correctly characterise the response of the heart, namely: (a) its passive or purely mechanical behaviour; (b) its electrophysiology; (c) its electric activation,

---

[1]Corresponding author: r.ortigosa@swansea.ac.uk
[2]Corresponding author: a.j.gil@swansea.ac.uk

responsible for the electrically driven contraction of the heart. Regarding the first aspect, namely the passive behaviour of the heart, it must be emphasised that the cardiac myocardium is an extremely complex and heterogeneous material with a strongly anisotropic behaviour which can be described via a set of collagen sheets and fibres [7]. To this aim, Diffusion Tensor Magnetic Resonance Imaging (DT-MRI) constitutes a very promising approach [8], although uncertainties related to *in vivo* measures may lead to unphysiological stress fields [9, 10]. Instead, the use of rule-based models or human atlases obtained through statistical treatment of *ex vivo* DT-MRI scans is preferred [11–13]. In addition, as experimentally reported by Vossoughi *et al.* [14], the cardiac muscle (or myocardium) is traditionally modelled as a nearly or truly incompressible hyperelastic material although recent investigations [15–17] question these assumptions.

A suitable invariant-based definition of the strain energy encapsulating the passive response of the myocardium must be chosen to describe its passive response, replicating both its anisotropic and incompressible behaviour. Since the pioneering work of Demiray [18], several constitutive models have been proposed [19–24]. In order to ensure a physically admissible behaviour of a constitutive model, this must satisfy the ellipticity condition [25]. A class of functions that satisfy ellipticity is that of polyconvexity [3, 26–33], where the strain energy is defined as a convex multivariable function of the deformation gradient tensor, its cofactor and its determinant. However, to the best of the authors' knowledge, polyconvex constitutive models have not been defined yet for the characterisation of the myocardium.

The second of the three aspects mentioned, namely the electrophysiology of the heart, has also been an intensive area of research [34, 35]. The heart fibres contract as a result of electrical stimuli (pulse) initiated in the sinoatrial node, located in the right atrium, and propagated over the heart tissue. This electric pulse produces a sharp rise (depolarisation) followed by a sudden fall (repolarisation) of the transmembrane electric potential in a process known as cardiac action potential [7]. As a result of the depolarisation, a wide range of ion interchanges (electric fluxes) take place across the cell membrane, triggering the cross-bridge cycle [7] in the muscle fibres and leading to the repolarisation of the cell membrane.

The resemblance of the cardiac action potential with propagation of waves enables this phenomenon to be mathematically modelled by means of a convection-diffusion-reaction equation where the source term encapsulates the cellular ion exchange (electric fluxes). For this purpose, a mathematical model named as bidomain model [36–38], was conceived to describe the cardiac action potential by considering two independent electric potentials, namely those in the inner and outer parts of the cell. However, an alternative and simpler approach known as monodomain model [39], where only the transmembrane potential is considered, is usually preferred [10, 40–42].

In the Nobel-price winning contributions of Hodgkin and Huxley, the electric fluxes (embedded in the aforementioned source term) were described via a set of ordinary differential equations linking the transmembrane potential with a set of gating variables representing the opening state of the ion channels [34]. Since then, a wide spectrum of more advanced models were developed [43–47]. Priebe and Beuckelmann [48] developed the first human ventricular model able to reproduce physiological and pathological behaviour. In this model, ion concentrations were, in addition to the gating variables in the original model of Hodgkin and Huxley, linked to the transmembrane potential. Moreover, Ten Tusscher *et al.* [2, 49] improved the previous model by considering additional experimental data performed in human ventricular myocytes. Finally, Bueno-Orovio *et al.* [1] proposed a more simplified model, known as the minimal model, convenient from the computational standpoint. Only the Ten Tusscher and Bueno-Orovio models will be considered in this paper.

The third aspect mentioned, namely the electro-mechanical activation of the heart, occurs as a result of the interaction of calcium ions with Troponin-C during the cross-bridge dynamics [7]. This can be phenomenologically described by means of the so called activation models. Two possible approaches can be followed for the definition of activation models, namely active stress

[20] or active strain approaches [50]. Within the first approach, Nash and Panfilov proposed an evolution equation for active cardiomyocite concentration stress [51, 52]. Within the second approach, Rossi *et al.* [10] proposed an evolution equation for the electric stretches of the active part of the multiplicatively decomposed deformation gradient tensor.

The computational modelling of the human heart is intrinsically challenging. Even if the three critical aspects described above, namely the passive and active responses of the heart as well as its electrical activation, are perfectly characterised, reliability of the results obtained via numerical simulation can be seriously compromised. Specifically, a computational implementation in terms of displacements and electric potential based on low order Finite Elements, very commonly used among researchers in this area [10, 53], are prone to exhibit parasitic behaviour characterised by shear locking and volumetric locking [32, 54–57], the latter arising in incompressible scenarios.

In order to circumvent these shortcomings of low order Finite Element implementations, a new mixed formulation is presented in this paper based on a series of recent publications by Gil and Ortigosa in the context of nonlinear elasticity and electro-mechanics [31, 58–60]. In this formulation, not only displacements and electric potential (and potentially a pressure-type Lagrange multiplier) are included as unknown fields. In addition, the deformation gradient tensor, its cofactor and its determinant and their respective work conjugates (stress variables) in conjunction with the electric potential gradient and its work conjugate are considered as unknown variables, adding more flexibility into the formulation. In order not to compromise the computational efficiency of the formulation, discontinuous functional spaces across elements are chosen for the extra fields, which enable to condense them out via a static condensation procedure, resulting in an extremely competitive computational approach.

The paper is organised as follows. Section 2 introduces some basic principles of kinematics. Section 3 presents the governing equations describing the motion of the heart and the evolution of the transmembrane potential. In Section 4, relevant aspects concerning the passive response of the myocardium, its electrophysiology and the coupling between the mechanics and the electric physics are presented. Based on the work of Gil and Ortigosa [31, 58–60], Section 5 introduces a new mixed formulation in the context of cardiac mechanics and its Finite Element implementation is described in Section 6. A series of examples are included in Section 7 in order to assess the robustness and accuracy of the proposed formulation. Finally, Section 8 provides some concluding remarks and a summary of the key contributions of this paper.

2. Kinematics

Let us consider the motion of a continuum (in this context representing the human myocardium) defined by a volume Ω_0 with boundary $\partial\Omega_0$ in its initial configuration with outward normal $\boldsymbol{N}$. After the motion, the continuum occupies a final configuration defined by a domain Ω with boundary $\partial\Omega$ with outward normal $\boldsymbol{n}$. The pseudo-time (t) dependent mapping field $\boldsymbol{\phi}$ links a material particle from initial configuration $\boldsymbol{X} \in \Omega_0$ to final configuration $\boldsymbol{x} \in \Omega$ according to $\boldsymbol{x} = \boldsymbol{\phi}(\boldsymbol{X}, t)$. The deformation gradient tensor $\boldsymbol{F_x}$, its cofactor $\boldsymbol{H_x}$ ($\boldsymbol{H_x} := \mathrm{Cof}\boldsymbol{F_x}$) and its determinant $J_{\boldsymbol{x}}$ ($J_{\boldsymbol{x}} := \det\boldsymbol{F_x}$) can be defined as

$$\boldsymbol{F_x} = \boldsymbol{\nabla}_0 \boldsymbol{x}; \qquad \boldsymbol{H_x} = \frac{1}{2}\boldsymbol{F_x} \times \boldsymbol{F_x}; \qquad J_{\boldsymbol{x}} = \frac{1}{3}\boldsymbol{H_x} : \boldsymbol{F_x}, \tag{1}$$

where $\boldsymbol{\nabla}_0 (\bullet)$ denotes the Lagrangian (initial configuration) gradient operator. For any two second order tensors $\boldsymbol{A}$ and $\boldsymbol{B}$, $\times$ in $(1)_b$ denotes the tensor cross product operation introduced in de Boer [61] and latter used in the context of nonlinear continuum mechanics [3, 33], defined as $(\boldsymbol{A} \times \boldsymbol{B})_{iI} = \mathcal{E}_{ijk}\mathcal{E}_{IJK}A_{jJ}B_{kK}$.

As shown in Figure 1, $\{\boldsymbol{F_x}, \boldsymbol{H_x}, J_{\boldsymbol{x}}\}$ represent the kinematic measures relating the differential fibre, area and volume elements from initial $\{d\boldsymbol{X}, d\boldsymbol{A}, dV\}$ to final $\{d\boldsymbol{x}, d\boldsymbol{a}, dv\}$ configuration.
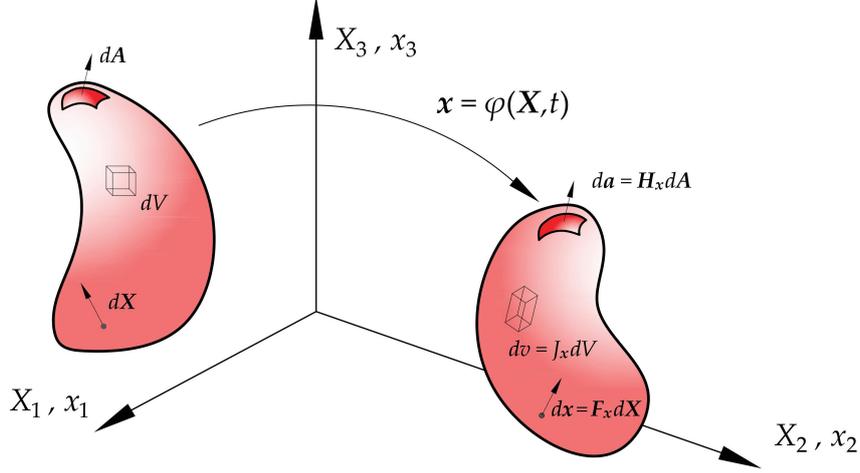
Figure 1: Motion map of the continuum Ω_0 and the kinematic measures $\boldsymbol{F_x}, \boldsymbol{H_x}, J_{\boldsymbol{x}}$.

For virtual and incremental variations of $\boldsymbol{x}$, namely $\delta\boldsymbol{x}$ and $\Delta\boldsymbol{x}$, use of equation (1) allows to evaluate the first and second directional derivatives of $\{\boldsymbol{F_x}, \boldsymbol{H_x}, J_{\boldsymbol{x}}\}$ as

$$D\boldsymbol{F_x}[\delta\boldsymbol{x}] = \boldsymbol{\nabla}_0\delta\boldsymbol{x}; \qquad D\boldsymbol{H_x}[\delta\boldsymbol{x}] = \boldsymbol{F_x} \times \boldsymbol{\nabla}_0\delta\boldsymbol{x}; \qquad DJ_{\boldsymbol{x}}[\delta\boldsymbol{x}] = \boldsymbol{H_x} : \boldsymbol{\nabla}_0\delta\boldsymbol{x};$$
$$D^2\boldsymbol{F_x}[\delta\boldsymbol{x}; \Delta\boldsymbol{x}] = \boldsymbol{0}; \qquad D^2\boldsymbol{H_x}[\delta\boldsymbol{x}; \Delta\boldsymbol{x}] = \boldsymbol{\nabla}_0\delta\boldsymbol{x} \times \boldsymbol{\nabla}_0\Delta\boldsymbol{x}; \qquad D^2J_{\boldsymbol{x}}[\delta\boldsymbol{x}; \Delta\boldsymbol{x}] = \boldsymbol{F_x} : (\boldsymbol{\nabla}_0\delta\boldsymbol{x} \times \boldsymbol{\nabla}_0\Delta\boldsymbol{x}).$$
(2)

3. Governing equations

In this section, the coupled system of partial differential equations governing the motion $\boldsymbol{x}$ and the evolution of transmembrane potential ϕ in the heart will be described. The first corresponds to the conservation of linear momentum (*mechanics*)[3], which can be expressed in a Lagrangian setting as

$$\left.\begin{array}{rll} \mathrm{DIV}\boldsymbol{P} + \boldsymbol{b}_0 = & \boldsymbol{0} & \text{in } \Omega_0 \times [\,0\,,\,T\,] \\ \boldsymbol{P}\boldsymbol{N} = & \boldsymbol{t}_0 & \text{on } \partial_t\Omega_0 \times [\,0\,,\,T\,] \\ \boldsymbol{x} = & \boldsymbol{\phi_x} & \text{on } \partial_{\boldsymbol{x}}\Omega_0 \times [\,0\,,\,T\,] \end{array}\right\}$$
(3)

with $\partial\Omega_0 = \partial_{\boldsymbol{x}}\Omega_0 \cup \partial_t\Omega_0$. In equation (3), $\boldsymbol{P}$ represents the first Piola-Kirchhoff stress tensor $\boldsymbol{b}_0$, a body force per unit undeformed volume and $\boldsymbol{t}_0$, a surface force per unit of undeformed area. In addition, the satisfaction of rotational equilibrium leads to the condition $\boldsymbol{P}\boldsymbol{F}_{\boldsymbol{x}}^T = \boldsymbol{F_x}\boldsymbol{P}^T$. The second governing equation represents the time-dependent evolution of the transmembrane potential ϕ (*electric*). When considering a monodomain approach [39, 40, 62], this can be expressed in a Lagrangian setting as

$$\left.\begin{array}{rll} \mathrm{DIV}\boldsymbol{Q} + f_\phi = & \dot{\phi} & \text{in } \Omega_0 \times [\,0\,,\,T\,] \\ \boldsymbol{Q} \cdot \boldsymbol{N} = & 0 & \text{on } \partial\Omega_0 \times [\,0\,,\,T\,] \\ \phi = & \phi_0\,(\boldsymbol{X}) & \text{in } \Omega_0 \end{array}\right\}$$
(4)

where $\phi_0\,(\boldsymbol{X})$ denotes the resting potential (initial conditions) and zero Neumann boundary condition are applied on the boundary $\partial\Omega_0$. Moreover, the vector $\boldsymbol{Q}$ represents the electric flux across the cell membrane [53] and f_ϕ, the electrical source term.

---

[3]It is customary to neglect inertial effects in equation (3) (*quasi-statics*).

4. Constitutive equations

For the closure of the governing equations defined by (3) and (4), constitutive laws are needed for the definition of the first Piola-Kirchhoff stress tensor $\boldsymbol{P}$ (3), the electric flux $\boldsymbol{Q}$ (4) and the electrical source term f_ϕ (4).

4.1. Passive response of the heart

The passive response of the heart, encapsulated in the strain energy $\Psi\left(\boldsymbol{\nabla}_0\boldsymbol{x}\right)$, can be mathematically described by means of an invariant representation of $\Psi\left(\boldsymbol{\nabla}_0\boldsymbol{x}\right)$ in terms of the main kinematic entities $\{\boldsymbol{F_x}, \boldsymbol{H_x}, J_{\boldsymbol{x}}\}$, namely

$$\Psi\left(\boldsymbol{\nabla}_0\boldsymbol{x}\right) = W\left(\boldsymbol{F_x}, \boldsymbol{H_x}, J_{\boldsymbol{x}}\right). \tag{5}$$

The energy functional $\Psi\left(\boldsymbol{\nabla}_0\boldsymbol{x}\right)$ in (5) has to describe the underlying anisotropic structure of the cardiac tissue, characterised by a spatially varying set of muscle fibres defined by the unitary direction $\boldsymbol{f}_0$ in the initial configuration. These muscle fibres are embedded into the collagen sheets, characterised by the perpendicular unitary normal $\boldsymbol{s}_0$ in the initial configuration. This enables to define the triad $\{\boldsymbol{f}_0, \boldsymbol{s}_0, \boldsymbol{n}_0\}$ at each Lagrangian particle $\boldsymbol{X} \in \Omega_0$ (refer to Figure 2). Furthermore, the functional $\Psi\left(\boldsymbol{\nabla}_0\boldsymbol{x}\right)$ needs to account for the incompressible or nearly incompressible nature of the heart tissue [14, 62, 63].
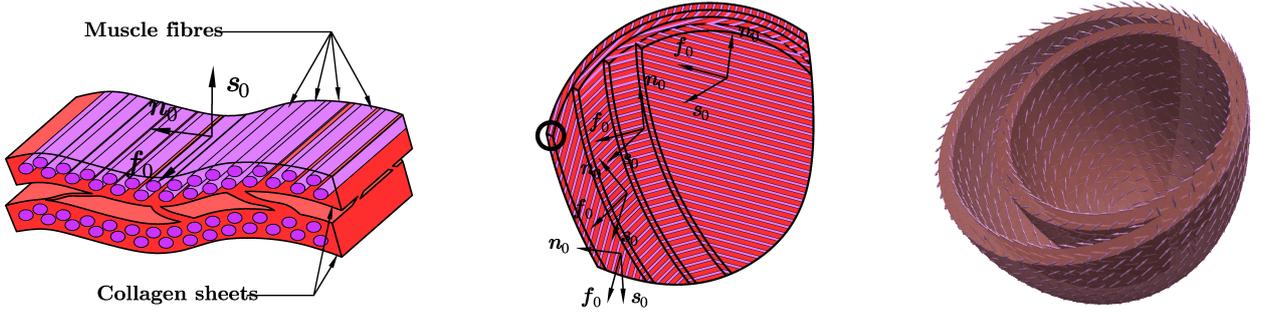
Figure 2: Anisotropic structure of the cardiac tissue. Representation of the triad $\{\boldsymbol{f}_0, \boldsymbol{s}_0, \boldsymbol{n}_0\}$ in the Lagrangian setting (left), accounting for their spatial variability (centre). Idealised set of ventricles (right).

Anisotropy and incompressibility can be embedded into the extended representation of Ψ, namely W (5), by means of an additive decomposition into its isotropic-deviatoric, volumetric and anisotropic contributions, denoted as $\hat{W}$, U and W^{ani} respectively, as

$$W\left(\boldsymbol{F_x}, \boldsymbol{H_x}, J_{\boldsymbol{x}}, \boldsymbol{f}_0, \boldsymbol{s}_0\right) = \hat{W}\left(\boldsymbol{F_x}, \boldsymbol{H_x}, J_{\boldsymbol{x}}\right) + U\left(J_{\boldsymbol{x}}\right) + W^{\mathrm{ani}}\left(\boldsymbol{F_x}, \boldsymbol{H_x}, J_{\boldsymbol{x}}, \boldsymbol{f}_0, \boldsymbol{s}_0\right), \tag{6}$$

where only $\hat{W}$ depends on the isochoric components of $\{\boldsymbol{F_x}, \boldsymbol{H_x}, J_{\boldsymbol{x}}\}$ [64–67] namely

$$\hat{W}\left(\boldsymbol{F_x}, \boldsymbol{H_x}, J_{\boldsymbol{x}}\right) = W\left(\hat{\boldsymbol{F}}_{\boldsymbol{x}}, \hat{\boldsymbol{H}}_{\boldsymbol{x}}, 1\right); \qquad \hat{\boldsymbol{F}}_{\boldsymbol{x}} = J_{\boldsymbol{x}}^{-1/3}\boldsymbol{F_x}; \qquad \hat{\boldsymbol{H}}_{\boldsymbol{x}} = J_{\boldsymbol{x}}^{-2/3}\boldsymbol{H_x}. \tag{7}$$

For the purely mechanical physics (no coupling with the transmembrane potential ϕ), the first Piola-Kirchhoff stress tensor $\boldsymbol{P}$ is obtained as

$$\boldsymbol{P} = \partial_{\boldsymbol{\nabla}_0\boldsymbol{x}}\Psi\left(\boldsymbol{\nabla}_0\boldsymbol{x}\right). \tag{8}$$

Alternatively, the extended representation W enables to obtain

$$\boldsymbol{P} : \boldsymbol{\nabla}_0\delta\boldsymbol{x} = DW[\delta\boldsymbol{x}] = \left(\partial_{\boldsymbol{F_x}}W + \partial_{\boldsymbol{H_x}}W \times \boldsymbol{F_x} + \partial_{J_{\boldsymbol{x}}}W\boldsymbol{H_x}\right) : \boldsymbol{\nabla}_0\delta\boldsymbol{x}, \tag{9}$$

where use of equation (1) has been made in above equation (9). Comparison of equations (8) and (9) enables to obtain an alternative expression for the first Piola-Kirchhoff stress tensor as

$$\boldsymbol{P} = \partial_{\boldsymbol{F_x}} W + \partial_{\boldsymbol{H_x}} W \times \boldsymbol{F_x} + \partial_{J_{\boldsymbol{x}}} W \boldsymbol{H_x}, \tag{10}$$

The ellipticity (rank-one convexity) or material stability of the strain energy $\Psi(\boldsymbol{\nabla}_0 \boldsymbol{x})$ guarantees the well-posedness of equation (3). This condition is directly related to the tangent operator of the strain energy $\Psi(\boldsymbol{\nabla}_0 \boldsymbol{x})$, i.e.

$$D^2\Psi[\delta\boldsymbol{x}; \Delta\boldsymbol{x}] = D\left(\boldsymbol{P} : \boldsymbol{\nabla}_0 \delta\boldsymbol{x}\right)[\Delta\boldsymbol{x}] = \boldsymbol{\nabla}_0\delta\boldsymbol{x} : \boldsymbol{\mathcal{C}} : \boldsymbol{\nabla}_0\Delta\boldsymbol{x}; \qquad \boldsymbol{\mathcal{C}} = \partial^2_{\boldsymbol{\nabla}_0 \boldsymbol{x} \boldsymbol{\nabla}_0 \boldsymbol{x}}\Psi, \tag{11}$$

where $\boldsymbol{\mathcal{C}}$ represents the fourth order elasticity tensor. Alternatively, the tangent operator can be equivalently obtained in terms of the extended representation $W(\boldsymbol{F_x}, \boldsymbol{H_x}, J_{\boldsymbol{x}})$ as

$$D^2W[\delta\boldsymbol{x}; \Delta\boldsymbol{x}] = D\left(\boldsymbol{P} : \boldsymbol{\nabla}_0 \delta\boldsymbol{x}\right)[\Delta\boldsymbol{x}] = \begin{bmatrix} \boldsymbol{\nabla}_0\delta\boldsymbol{x} : \\ \boldsymbol{F_x} \times \boldsymbol{\nabla}_0\delta\boldsymbol{x} : \\ \boldsymbol{H_x} : \boldsymbol{\nabla}_0\delta\boldsymbol{x} \end{bmatrix}^T \begin{bmatrix} \mathbb{H}_W \end{bmatrix} \begin{bmatrix} : \boldsymbol{\nabla}_0\Delta\boldsymbol{x} \\ : \boldsymbol{F_x} \times \boldsymbol{\nabla}_0\Delta\boldsymbol{x} \\ \boldsymbol{H_x} : \boldsymbol{\nabla}_0\Delta\boldsymbol{x} \end{bmatrix} \\ + \left(\partial_{\boldsymbol{H_x}} W + \partial_{J_{\boldsymbol{x}}} W \boldsymbol{F_x}\right) : \left(\boldsymbol{\nabla}_0\delta\boldsymbol{x} \times \boldsymbol{\nabla}_0\Delta\boldsymbol{x}\right), \tag{12}$$

where $\left[\mathbb{H}_W\right]$ represents the Hessian operator of W, namely

$$\left[\mathbb{H}_W\right] = \begin{bmatrix} \partial^2_{\boldsymbol{F_x}\boldsymbol{F_x}} W & \partial^2_{\boldsymbol{F_x}\boldsymbol{H_x}} W & \partial^2_{\boldsymbol{F_x}J_{\boldsymbol{x}}} W \\ \partial^2_{\boldsymbol{H_x}\boldsymbol{F_x}} W & \partial^2_{\boldsymbol{H_x}\boldsymbol{H_x}} W & \partial^2_{\boldsymbol{H_x}J_{\boldsymbol{x}}} W \\ \partial^2_{J_{\boldsymbol{x}}\boldsymbol{F_x}} W & \partial^2_{J_{\boldsymbol{x}}\boldsymbol{H_x}} W & \partial^2_{J_{\boldsymbol{x}}J_{\boldsymbol{x}}} W \end{bmatrix}. \tag{13}$$

Comparison of (11) and (12) enables to additively decompose $\boldsymbol{\mathcal{C}}$ into a purely material contribution $\boldsymbol{\mathcal{C}}_m$ (depending upon second derivatives of W) and a geometrical contribution $\boldsymbol{\mathcal{C}}_g$ (emerging from the inherent non-linearity of $\{\boldsymbol{H_x}, J_{\boldsymbol{x}}\}$), namely $\boldsymbol{\mathcal{C}} = \boldsymbol{\mathcal{C}}_m + \boldsymbol{\mathcal{C}}_g$, with

$$\boldsymbol{\mathcal{C}}_m = \partial^2_{\boldsymbol{F_x}\boldsymbol{F_x}} W + \boldsymbol{F_x} \times \partial^2_{\boldsymbol{H_x}\boldsymbol{H_x}} W \times \boldsymbol{F_x} + \partial^2_{J_{\boldsymbol{x}}J_{\boldsymbol{x}}} W \boldsymbol{H_x} \otimes \boldsymbol{H_x} + \partial^2_{\boldsymbol{F_x}\boldsymbol{H_x}} W \times \boldsymbol{F_x} + \boldsymbol{F_x} \times \partial^2_{\boldsymbol{H_x}\boldsymbol{F_x}} W$$
$$+ \partial^2_{\boldsymbol{F_x}J_{\boldsymbol{x}}} W \otimes \boldsymbol{H_x} + \boldsymbol{H_x} \otimes \partial^2_{J_{\boldsymbol{x}}\boldsymbol{F_x}} W + \boldsymbol{F_x} \times \partial^2_{\boldsymbol{H_x}J_{\boldsymbol{x}}} W \otimes \boldsymbol{H_x} + \boldsymbol{H_x} \otimes \partial^2_{J_{\boldsymbol{x}}\boldsymbol{H_x}} W \times \boldsymbol{F_x}; \tag{14}$$
$$\boldsymbol{\mathcal{C}}_g = \boldsymbol{\mathcal{I}} \times \left(\partial_{\boldsymbol{H_x}} W + \partial_{J_{\boldsymbol{x}}} W \boldsymbol{F_x}\right),$$

with $\mathcal{I}_{iIjJ} = \delta_{ij}\delta_{IJ}$ and $(\boldsymbol{\mathcal{A}} \times \boldsymbol{A})_{iIjJ} = \mathcal{E}_{jpq}\mathcal{E}_{JPQ}\mathcal{A}_{iIpP}A_{qQ}$ and $(\boldsymbol{A} \times \boldsymbol{\mathcal{A}})_{iIjJ} = \mathcal{E}_{ipq}\mathcal{E}_{IPQ}A_{pP}\mathcal{A}_{qQjJ}$, for $\boldsymbol{\mathcal{A}} \in \mathbb{R}^{3\times3\times3\times3}$ and $\boldsymbol{A} \in \mathbb{R}^{3\times3}$.

The ellipticity condition requires that, for $\boldsymbol{\nabla}_0\delta\boldsymbol{x} = \boldsymbol{\nabla}_0\Delta\boldsymbol{x} = \boldsymbol{u} \otimes \boldsymbol{V}$, with $\boldsymbol{u}, \boldsymbol{V} \in \mathbb{R}^3$ and $\boldsymbol{u} \neq \boldsymbol{0}$, $\boldsymbol{V} \neq \boldsymbol{0}$, the tangent operator in (11) and (12) is positive, namely

$$\mathcal{I}_W = (\boldsymbol{u} \otimes \boldsymbol{V}) : \boldsymbol{\mathcal{C}} : (\boldsymbol{u} \otimes \boldsymbol{V}) = \begin{bmatrix} \boldsymbol{u} \otimes \boldsymbol{V} : \\ \boldsymbol{F_x} \times (\boldsymbol{u} \otimes \boldsymbol{V}) : \\ \boldsymbol{H_x} : (\boldsymbol{u} \otimes \boldsymbol{V}) \end{bmatrix}^T \begin{bmatrix} \mathbb{H}_W \end{bmatrix} \begin{bmatrix} : \boldsymbol{u} \otimes \boldsymbol{V} \\ : \boldsymbol{F_x} \times (\boldsymbol{u} \otimes \boldsymbol{V}) \\ \boldsymbol{H_x} : (\boldsymbol{u} \otimes \boldsymbol{V}) \end{bmatrix} \geq 0. \tag{15}$$

In above equation (15), the contribution from the geometrical component $\boldsymbol{\mathcal{C}}_g$ vanishes, i.e. $(\boldsymbol{u} \otimes \boldsymbol{V}) : \boldsymbol{\mathcal{C}}_g : (\boldsymbol{u} \otimes \boldsymbol{V}) = 0$, as shown in References [58]. A sufficient condition for (15) to hold is the positive definiteness of the acoustic tensor $\boldsymbol{\mathcal{C}_{VV}}$, defined as

$$(\boldsymbol{\mathcal{C}_{VV}})_{ij} = (\boldsymbol{\mathcal{C}})_{iIjJ} V_I V_J; \quad \forall \boldsymbol{V} \in \mathbb{R}^3; \; \boldsymbol{V} \neq \boldsymbol{0}. \tag{16}$$

Alternatively, a more restrictive sufficient condition for (15) to hold is the positive definiteness of $\left[\mathbb{H}_W\right]$. This is automatically satisfied if the strain energy functional $\Psi(\boldsymbol{\nabla}_0 \boldsymbol{x})$ (5) is sufficiently differentiable and polyconvex [26, 27, 29, 30, 68], namely if its extended representation $W(\boldsymbol{F_x}, \boldsymbol{H_x}, J_{\boldsymbol{x}})$ is convex with respect to its arguments, i.e.

$$W(\boldsymbol{A}_3, \boldsymbol{B}_3, C_3) \leq \lambda W(\boldsymbol{A}_1, \boldsymbol{B}_1, C_1) + (1 - \lambda) W(\boldsymbol{A}_2, \boldsymbol{B}_2, C_2); \qquad \forall \lambda \in [0, 1], \tag{17}$$

$\forall \boldsymbol{A}_1, \boldsymbol{A}_2, \boldsymbol{B}_1, \boldsymbol{B}_2 \in \mathbb{R}^{3\times3}$ and $C_1, C_2 \in \mathbb{R}$ and $\boldsymbol{A}_3 = \lambda\boldsymbol{A}_1 + (1 - \lambda)\boldsymbol{A}_2$, $\boldsymbol{B}_3 = \lambda\boldsymbol{B}_1 + (1 - \lambda)\boldsymbol{B}_2$ and $C_3 = \lambda C_1 + (1 - \lambda) C_2$.

4.1.1. An example for the passive response

As an example, let us consider the classical invariant-based representation of the strain energy proposed by Holzapfel-Ogden [24] for the characterisation of the passive response of the myocardium. In this energy, each one of the terms introduced in equation (6) are

$$\hat{W}(\boldsymbol{F_x}, J_{\boldsymbol{x}}) = \frac{a}{2b}e^{b\left(\hat{I}I_{\boldsymbol{F_x}}-3\right)}; \qquad\qquad U\left(J_{\boldsymbol{x}}\right) = \frac{\kappa}{2}\left(J_{\boldsymbol{x}}-1\right)^2;$$

$$W^{\mathrm{ani}}\left(\boldsymbol{F_x}, \boldsymbol{f}_0, \boldsymbol{s}_0\right) = \frac{a_f}{2b_f}\left(e^{b_f\langle I_{4,\boldsymbol{f}_0}-1\rangle^2}-1\right) + \frac{a_s}{2b_s}\left(e^{b_s\langle I_{4,\boldsymbol{s}_0}-1\rangle^2}-1\right) + \frac{a_{fs}}{2b_{fs}}\left(e^{b_{fs}I_{8,\boldsymbol{f}_0\boldsymbol{s}_0}^2}-1\right), \quad (18)$$

where $\{a, \kappa, a_f, a_s, a_{fs}, b_f, b_s, b_{fs}\}$ are positive material constants and $\langle\bullet\rangle$ represents the Macaulay brackets $\langle\bullet\rangle = \left(\bullet + |\bullet|\right)/2$ to prevent fibres from working in contraction [69, 70], $II_{(\bullet)}$ denotes the second invariant of $(\bullet)$ and with the anisotropic invariants $I_{4,\boldsymbol{f}_0}, I_{4,\boldsymbol{s}_0}, I_{8,\boldsymbol{f}_0\boldsymbol{s}_0}$ defined as

$$I_{4,\boldsymbol{f}_0} = \boldsymbol{F_x}\boldsymbol{f}_0 \cdot \boldsymbol{F_x}\boldsymbol{f}_0; \qquad I_{4,\boldsymbol{s}_0} = \boldsymbol{F_x}\boldsymbol{s}_0 \cdot \boldsymbol{F_x}\boldsymbol{s}_0; \qquad I_{8,\boldsymbol{f}_0\boldsymbol{s}_0} = \boldsymbol{F_x}\boldsymbol{f}_0 \cdot \boldsymbol{F_x}\boldsymbol{s}_0. \qquad (19)$$

For the specific constitutive model defined in (18), the elements of the set $\{\partial_{\boldsymbol{F_x}}W, \partial_{\boldsymbol{H_x}}W, \partial_{J_{\boldsymbol{x}}}W\}$ featuring in the definition of $\boldsymbol{P}$ in (10) are

$$\partial_{\boldsymbol{F_x}}W = ae^{b\left(\hat{I}I_{\boldsymbol{F_x}}-3\right)}J_{\boldsymbol{x}}^{-\frac{2}{3}}\boldsymbol{F_x} + 2a_fe^{b_f\left\langle I_{4,\boldsymbol{f}_0}-1\right\rangle^2}\left\langle I_{4,\boldsymbol{f}_0}-1\right\rangle\boldsymbol{F_x}\boldsymbol{f}_0\otimes\boldsymbol{f}_0+$$

$$+ 2a_se^{b_s\left\langle I_{4,\boldsymbol{s}_0}-1\right\rangle^2}\left\langle I_{4,\boldsymbol{s}_0}-1\right\rangle\boldsymbol{F_x}\boldsymbol{s}_0\otimes\boldsymbol{s}_0 + a_{fs}e^{b_{fs}I_{8,\boldsymbol{f}_0\boldsymbol{s}_0}^2}I_{8,\boldsymbol{f}_0\boldsymbol{s}_0}\left(\boldsymbol{F_x}\boldsymbol{f}_0\otimes\boldsymbol{s}_0 + \boldsymbol{F_x}\boldsymbol{s}_0\otimes\boldsymbol{f}_0\right);$$

$$\partial_{\boldsymbol{H_x}}W = \boldsymbol{0};$$

$$\partial_{J_{\boldsymbol{x}}}W = -\frac{a}{3}J_{\boldsymbol{x}}^{-1}\hat{I}I_{\boldsymbol{F_x}}e^{b\left(\hat{I}I_{\boldsymbol{F_x}}-3\right)} + U'\left(J_{\boldsymbol{x}}\right).$$

$$(20)$$

The energy functional in (18) is not elliptic and, hence, not polyconvex. This is shown in Appendix A, where the following expression for the ellipticity indicator $\mathcal{I}_W$ (15) has been obtained

$$\mathcal{I}_W \geq -2a_{fs}e^{b_{fs}I_{8,\boldsymbol{f}_0\boldsymbol{s}_0}^2}I_{8,\boldsymbol{f}_0\boldsymbol{s}_0}\left(\boldsymbol{u}\cdot\boldsymbol{u}\right)|\left(\boldsymbol{V}\cdot\boldsymbol{f}_0\right)\left(\boldsymbol{V}\cdot\boldsymbol{s}_0\right)|. \qquad (21)$$

From (21), it can be concluded that the only term responsible for the possible loss of ellipticity of the model in (18) is that associated with the non-elliptic invariant $I_{8,\boldsymbol{f}_0\boldsymbol{s}_0}$. $\mathcal{I}_W$ (15) might adopt negative values throughout the deformation due to this term. Negative values of $\mathcal{I}_W$ (21) for any given $\boldsymbol{u}, \boldsymbol{V} \in \mathbb{R}^3$, $\boldsymbol{u}, \boldsymbol{V} \neq \boldsymbol{0}$ can induce loss of positive definiteness of the acoustic tensor $\mathcal{C}_{\boldsymbol{VV}}$ in (16), leading to loss of ellipticity and, hence, loss of polyconvexity. A numerical study of the possible loss of ellipticity and polyconvexity of this model will be carried out in Section 7.6.

Remark 1. Notice that it is possible to (poly)-convexify the invariant $I_{8,\boldsymbol{f}_0\boldsymbol{s}_0}$ via its convexified counterpart $I_{8,\boldsymbol{f}_0\boldsymbol{s}_0}^{\star}$ defined as

$$I_{8,\boldsymbol{f}_0\boldsymbol{s}_0}^{\star} = \left(\alpha\boldsymbol{F_x}\boldsymbol{f}_0 + \beta\boldsymbol{F_x}\boldsymbol{s}_0\right)\cdot\left(\alpha\boldsymbol{F_x}\boldsymbol{f}_0 + \beta\boldsymbol{F_x}\boldsymbol{s}_0\right) - \left(\alpha^2 + \beta^2\right), \qquad (22)$$

where the dimensionless parameters $\{\alpha, \beta\}$ would have to be defined via material characterisation. Replacing $I_{8,\boldsymbol{f}_0\boldsymbol{s}_0}$ with $I_{8,\boldsymbol{f}_0\boldsymbol{s}_0}^{\star}$ in (18) yields a polyconvexification of this constitutive model. The specific choice of $\alpha = 1$ and $\beta = -1$ is of special interest as the resulting invariant represents the stretch or shortening of the hypotenuse of the right-angled triangle with adjacent sides defined by the unit vectors $\boldsymbol{f}_0$ and $\boldsymbol{s}_0$.

In the following sections, two well-known approaches describing the coupling of the strain energy W in equation (18) with the electro-activation will be presented.

4.1.2. Coupling of first Piola-Kirchhoff stress tensor with the transmembrane potential ϕ: active stress approach

In the active stress approach [20, 51, 52], an additive decomposition of $\boldsymbol{P}$ is defined in terms of a coupled (active) $\boldsymbol{P}_{\text{Active}}$ contribution and a purely mechanical (passive) $\boldsymbol{P}_{\text{Passive}}$ contribution as

$$\boldsymbol{P} = \boldsymbol{P}_{\text{Active}} + \boldsymbol{P}_{\text{Passive}}; \quad \boldsymbol{P}_{\text{Active}} = T_a \boldsymbol{F_x} \boldsymbol{f}_0 \otimes \boldsymbol{f}_0; \quad \boldsymbol{P}_{\text{Passive}} = \partial_{\boldsymbol{F_x}} W + \partial_{\boldsymbol{H_x}} W \times \boldsymbol{F_x} + \partial_{J_x} W \boldsymbol{H_x}, \tag{23}$$

where T_a repressents the active cardiomyocite contraction stress and the passive term $\boldsymbol{P}_{\text{Passive}}$ adopts an identical representation to that in (10). Evolution equations relating T_a with the transmembrane potential ϕ will be presented in section 4.3.1.

In this approach, the tangent operator of the active contribution $\boldsymbol{P}_{\text{Active}}$ can be written as

$$D\left(\boldsymbol{P}_{\text{Active}} : \boldsymbol{\nabla}_0 \delta \boldsymbol{x}\right)[\Delta \boldsymbol{x}] = \boldsymbol{\nabla}_0 \delta \boldsymbol{x} : \left[T_a \boldsymbol{\mathcal{T}}_{\boldsymbol{f}_0 \boldsymbol{f}_0}\right] : \boldsymbol{\nabla}_0 \Delta \boldsymbol{x}; \qquad \left(\boldsymbol{\mathcal{T}}_{\boldsymbol{f}_0 \boldsymbol{f}_0}\right)_{iIjJ} = \delta_{ij} \left(\boldsymbol{f}_0\right)_I \left(\boldsymbol{f}_0\right)_J. \tag{24}$$

Therefore, in addition to the material and geometrical components $\boldsymbol{\mathcal{C}}_m$ and $\boldsymbol{\mathcal{C}}_g$, the elasticity tensor includes an additional active contribution $\boldsymbol{\mathcal{C}}_{T_a}$ as

$$\boldsymbol{\mathcal{C}} = \boldsymbol{\mathcal{C}}_m + \boldsymbol{\mathcal{C}}_g + \boldsymbol{\mathcal{C}}_{T_a}; \qquad \boldsymbol{\mathcal{C}}_{T_a} = T_a \boldsymbol{\mathcal{T}}_{\boldsymbol{f}_0 \boldsymbol{f}_0}. \tag{25}$$

The ellipticity condition for the active stress approach[4] can then be written as

$$(\boldsymbol{u} \otimes \boldsymbol{V}) : \boldsymbol{\mathcal{C}} : (\boldsymbol{u} \otimes \boldsymbol{V}) = \begin{bmatrix} \boldsymbol{u} \otimes \boldsymbol{V} : \\ \boldsymbol{F_x} \times (\boldsymbol{u} \otimes \boldsymbol{V}) : \\ \boldsymbol{H_x} : (\boldsymbol{u} \otimes \boldsymbol{V}) \end{bmatrix}^T \left[\widetilde{\mathbb{H}}_W\right] \begin{bmatrix} : \boldsymbol{u} \otimes \boldsymbol{V} \\ : \boldsymbol{F_x} \times (\boldsymbol{u} \otimes \boldsymbol{V}) \\ \boldsymbol{H_x} : (\boldsymbol{u} \otimes \boldsymbol{V}) \end{bmatrix} \geq 0, \tag{26}$$

with

$$\left[\widetilde{\mathbb{H}}_W\right] = \left[\mathbb{H}_W\right] + \begin{bmatrix} T_a \boldsymbol{f}_0 \otimes \boldsymbol{f}_0 & \boldsymbol{0}_{3\times3} & \boldsymbol{0}_{3\times1} \\ \boldsymbol{0}_{3\times3} & \boldsymbol{0}_{3\times3} & \boldsymbol{0}_{3\times1} \\ \boldsymbol{0}_{1\times3} & \boldsymbol{0}_{1\times3} & 0 \end{bmatrix}. \tag{27}$$

Crucially, positive values of T_a (associated with contractions along the fibre $\boldsymbol{f}_0$) guarantee the ellipticity of the active contribution $\boldsymbol{P}_{\text{Active}}$ in (23)$_b$. Furthermore, positive values of T_a can help *stabilising* the loss of ellipticity induced by the energetic contribution associated with the invariant $I_{8,\boldsymbol{f}_0 \boldsymbol{s}_0}$ in (18) (refer to end of Section 4.1.1).

4.1.3. Coupling of stresses with the transmembrane potential ϕ: active strain approach

The second approach for the coupling of the mechanical and electrical physics, known as active strain [10, 50, 62], is based on a multiplicative decomposition of the deformation gradient tensor $\boldsymbol{F_x}$ into its elastic (passive) $\boldsymbol{F_x}^E$ and coupled (active) $\boldsymbol{F}^A$ contributions (refer to Figure 3), namely

$$\boldsymbol{F_x} = \boldsymbol{F_x}^E \boldsymbol{F}^A. \tag{28}$$

In this approach, the coupling is embedded into the active component $\boldsymbol{F}^A$, related to the electrically activated stretches $\left\{\gamma_{\boldsymbol{f}_0}, \gamma_{\boldsymbol{s}_0}, \gamma_{\boldsymbol{n}_0}\right\}$ along the fibres $\{\boldsymbol{f}_0, \boldsymbol{s}_0, \boldsymbol{n}_0\}$, defined as

$$\boldsymbol{F}^A = \boldsymbol{I} + \gamma_{\boldsymbol{f}_0} \boldsymbol{f}_0 \otimes \boldsymbol{f}_0 + \gamma_{\boldsymbol{s}_0} \boldsymbol{s}_0 \otimes \boldsymbol{s}_0 + \gamma_{\boldsymbol{n}_0} \boldsymbol{n}_0 \otimes \boldsymbol{n}_0. \tag{29}$$

Evolution equations relating $\gamma_{\boldsymbol{f}_0}$ with the transmembrane potential ϕ will be presented in Section 4.3.2. The $\{\gamma_{\boldsymbol{s}_0}, \gamma_{\boldsymbol{n}_0}\}$ are usually related to $\gamma_{\boldsymbol{f}_0}$ (see Remark 2).

---

[4] Taking $\boldsymbol{\nabla}_0 \delta \boldsymbol{x} = \boldsymbol{\nabla}_0 \Delta \boldsymbol{x} = \boldsymbol{u} \otimes \boldsymbol{V}$.
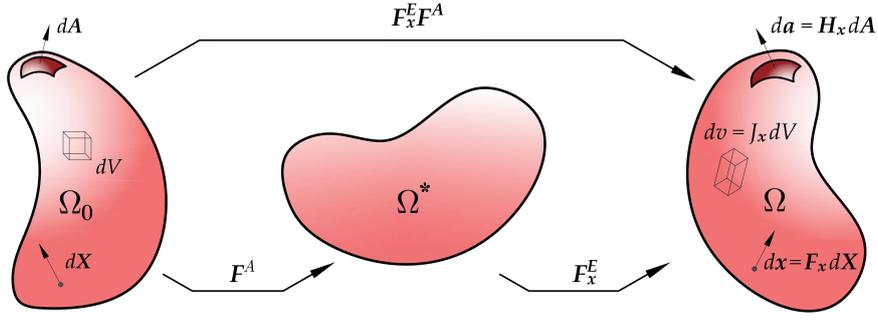
Figure 3: Multiplicative decomposition of the deformation gradient tensor $\boldsymbol{F_x}$ for the active strain approach.

Remark 2. It is customary [62, 71] to assume that $\det \boldsymbol{F}^A = 1$. Therefore, the widely used assumption of equal values for $\{\gamma_{\boldsymbol{f}_0}, \gamma_{\boldsymbol{s}_0}\}$ enables to relate both to $\gamma_{\boldsymbol{f}_0}$ as

$$\gamma_{\boldsymbol{s}_0} = \gamma_{\boldsymbol{n}_0} = \frac{1}{\sqrt{1 + \gamma_{\boldsymbol{f}_0}}} - 1. \tag{30}$$

Nevertheless, the latter assumption fails to correctly reproduce the heart wall thickness reduction during a heartbeat [16]. In order to circumvent this shortcoming, Rossi *et al.* [10] proposed an alternative definition of $\{\gamma_{\boldsymbol{f}_0}, \gamma_{\boldsymbol{s}_0}\}$ (compatible with $\det \boldsymbol{F}^A = 1$) as

$$\gamma_{\boldsymbol{n}_0} = 4\gamma_{\boldsymbol{f}_0}; \qquad \gamma_{\boldsymbol{s}_0} = \frac{1}{\left(1 + \gamma_{\boldsymbol{f}_0}\right)\left(1 + \gamma_{\boldsymbol{n}_0}\right)} - 1. \tag{31}$$

In the active strain approach, the coupling is achieved after a redefinition of the strain energy Ψ, which must depend on the elastic components of $\boldsymbol{F_x}$, namely

$$\Psi\left(\boldsymbol{\nabla}_0 \boldsymbol{x}, \boldsymbol{F}^A\right) = W\left(\boldsymbol{F}_{\boldsymbol{x}}^E, \boldsymbol{H}_{\boldsymbol{x}}^E, J_{\boldsymbol{x}}^E\right), \tag{32}$$

with $\{\boldsymbol{F}_{\boldsymbol{x}}^E, \boldsymbol{H}_{\boldsymbol{x}}^E, J_{\boldsymbol{x}}^E\}$ defined as

$$\boldsymbol{F}_{\boldsymbol{x}}^E = \boldsymbol{F_x} \boldsymbol{F}^{A-1}; \qquad \boldsymbol{H}_{\boldsymbol{x}}^E = \boldsymbol{H_x} \boldsymbol{H}^{A-1}; \qquad J_{\boldsymbol{x}}^E = J_{\boldsymbol{x}} J^{A-1}, \tag{33}$$

and

$$\boldsymbol{H}^A = \frac{1}{2}\boldsymbol{F}^A \times \boldsymbol{F}^A; \qquad J^A = \frac{1}{3}\boldsymbol{H}^A : \boldsymbol{F}^A. \tag{34}$$

This enables to re-express the strain energy in (32) in terms of the strain measures $\{\boldsymbol{F_x}, \boldsymbol{H_x}, J_{\boldsymbol{x}}\}$ and its active counterparts $\{\boldsymbol{F}^A, \boldsymbol{H}^A, J^A\}$ as

$$\Psi\left(\boldsymbol{\nabla}_0\boldsymbol{x}\right) = W\left(\boldsymbol{F}_{\boldsymbol{x}}^E, \boldsymbol{H}_{\boldsymbol{x}}^E, J_{\boldsymbol{x}}^E\right) = W^E\left(\boldsymbol{F_x}, \boldsymbol{H_x}, J_{\boldsymbol{x}}, \boldsymbol{F}^{A-1}, \boldsymbol{H}^{A-1}, J^{A-1}\right). \tag{35}$$

The re-expression of the strain energy in terms of $\{\boldsymbol{F_x}, \boldsymbol{H_x}, J_{\boldsymbol{x}}\}$ leads to an expression for $\boldsymbol{P}$ as

$$\boldsymbol{P} = \partial_{\boldsymbol{F_x}} W^E + \partial_{\boldsymbol{H_x}} W^E \times \boldsymbol{F_x} + \partial_{J_{\boldsymbol{x}}} W^E \boldsymbol{H_x}. \tag{36}$$

The tangent operator of W^E is

$$D^2 W[\delta\boldsymbol{x}; \Delta\boldsymbol{x}] = D^2 W^E[\delta\boldsymbol{x}; \Delta\boldsymbol{x}] = \begin{bmatrix} \boldsymbol{\nabla}_0\delta\boldsymbol{x} : \\ \boldsymbol{F_x} \times \boldsymbol{\nabla}_0\delta\boldsymbol{x} : \\ \boldsymbol{H_x} : \boldsymbol{\nabla}_0\delta\boldsymbol{x} \end{bmatrix}^T \left[\mathbb{H}_{W^E}\right] \begin{bmatrix} : \boldsymbol{\nabla}_0\Delta\boldsymbol{x} \\ : \boldsymbol{F_x} \times \boldsymbol{\nabla}_0\Delta\boldsymbol{x} \\ \boldsymbol{H_x} : \boldsymbol{\nabla}_0\Delta\boldsymbol{x} \end{bmatrix} \\ + \left(\partial_{\boldsymbol{H_x}} W^E + \partial_{J_{\boldsymbol{x}}} W^E \boldsymbol{F_x}\right) : \left(\boldsymbol{\nabla}_0\delta\boldsymbol{x} \times \boldsymbol{\nabla}_0\Delta\boldsymbol{x}\right), \tag{37}$$

9

where $\left[\mathbb{H}_{W^E}\right]$ represents the Hessian operator of W^E. The ellipticity indicator $\mathcal{I}_W$ can now be expressed as

$$\mathcal{I}_W = (\boldsymbol{u} \otimes \boldsymbol{V}) : \boldsymbol{\mathcal{C}}_{W^E} : (\boldsymbol{u} \otimes \boldsymbol{V}) = \begin{bmatrix} \boldsymbol{u} \otimes \boldsymbol{V} : \\ \boldsymbol{F_x} \times (\boldsymbol{u} \otimes \boldsymbol{V}) : \\ \boldsymbol{H_x} : (\boldsymbol{u} \otimes \boldsymbol{V}) \end{bmatrix}^T \left[\mathbb{H}_{W^E}\right] \begin{bmatrix} : \boldsymbol{u} \otimes \boldsymbol{V} \\ : \boldsymbol{F_x} \times (\boldsymbol{u} \otimes \boldsymbol{V}) \\ \boldsymbol{H_x} : (\boldsymbol{u} \otimes \boldsymbol{V}) \end{bmatrix} \geq 0. \quad (38)$$

In this approach, the consideration of the strain energy W^E as in (35) leads to re-expression of the model in equation (18) as

$$\hat{W}^E(\boldsymbol{F_x}, J_{\boldsymbol{x}}, \boldsymbol{F}^{A^{-1}}) = \frac{a}{2b} e^{b\left(\hat{I}\hat{I}^E_{\boldsymbol{F_x}} - 3\right)}; \qquad\qquad U^E\left(J_{\boldsymbol{x}} J^{A^{-1}}\right) = \frac{\kappa}{2}\left(J_{\boldsymbol{x}} J^{A^{-1}} - 1\right)^2;$$

$$W^{E\,\mathrm{ani}}\left(\boldsymbol{F_x}, \boldsymbol{F}^{A^{-1}}, \boldsymbol{f}_0, \boldsymbol{s}_0\right) = \frac{a_f}{2b_f}\left(e^{b_f\langle I^E_{4,\boldsymbol{f}_0}-1\rangle^2} - 1\right) + \frac{a_s}{2b_s}\left(e^{b_s\langle I^E_{4,\boldsymbol{s}_0}-1\rangle^2} - 1\right) + \frac{a_{fs}}{2b_{fs}}\left(e^{b_{fs} I^E_{8,\boldsymbol{f}_0\boldsymbol{s}_0}{}^2} - 1\right),$$

$$(39)$$

with

$$\hat{I}\hat{I}^E_{\boldsymbol{F_x}} = J_{\boldsymbol{x}}^{-2/3} J^{A2/3}\left(\boldsymbol{F_x}\boldsymbol{F}^A\right) : \left(\boldsymbol{F_x}\boldsymbol{F}^{A^{-1}}\right); \qquad\qquad I^E_{4,\boldsymbol{f}_0} = \left(\boldsymbol{F_x}\boldsymbol{F}^{A^{-1}}\boldsymbol{f}_0\right) \cdot \left(\boldsymbol{F_x}\boldsymbol{F}^{A^{-1}}\boldsymbol{f}_0\right);$$

$$I^E_{4,\boldsymbol{s}_0} = \left(\boldsymbol{F_x}\boldsymbol{F}^{A^{-1}}\boldsymbol{s}_0\right) \cdot \left(\boldsymbol{F_x}\boldsymbol{F}^{A^{-1}}\boldsymbol{s}_0\right); \qquad\qquad I^E_{8,\boldsymbol{f}_0\boldsymbol{s}_0} = \left(\boldsymbol{F_x}\boldsymbol{F}^{A^{-1}}\boldsymbol{f}_0\right) \cdot \left(\boldsymbol{F_x}\boldsymbol{F}^{A^{-1}}\boldsymbol{s}_0\right). \qquad (40)$$

For the specific constitutive model defined in (18), the elements of the set $\{\partial_{\boldsymbol{F_x}}W, \partial_{\boldsymbol{H_x}}W, \partial_{J_{\boldsymbol{x}}}W\}$ featuring in the definition of $\boldsymbol{P}$ in (36) are

$$\partial_{\boldsymbol{F_x}}W^E = a e^{b\left(II^E_{\boldsymbol{F_x}} - 3\right)} J_{\boldsymbol{x}}^{-\frac{2}{3}} J^{A\frac{2}{3}}\left(\boldsymbol{F_x}\boldsymbol{F}^{A^{-1}}\boldsymbol{F}^{A^{-T}}\right) + 2a_f e^{b_f\left\langle I^E_{4,\boldsymbol{f}_0}-1\right\rangle^2}\left\langle I_{4,\boldsymbol{f}_0} - 1\right\rangle\left(\boldsymbol{F_x}\boldsymbol{F}^{A^{-1}}\boldsymbol{f}_0 \otimes \boldsymbol{F}^{A^{-1}}\boldsymbol{f}_0\right) +$$

$$+ 2a_s e^{b_s\left\langle I^E_{4,\boldsymbol{s}_0}-1\right\rangle^2}\left\langle I^E_{4,\boldsymbol{s}_0} - 1\right\rangle\left(\boldsymbol{F_x}\boldsymbol{F}^{A^{-1}}\boldsymbol{s}_0 \otimes \boldsymbol{F}^{A^{-1}}\boldsymbol{s}_0\right)$$

$$+ a_{fs} e^{b_{fs} I^E_{8,\boldsymbol{f}_0\boldsymbol{s}_0}{}^2} I^E_{8,\boldsymbol{f}_0\boldsymbol{s}_0}\left(\boldsymbol{F_x}\boldsymbol{F}^{A^{-1}}\boldsymbol{f}_0 \otimes \boldsymbol{s}_0 + \boldsymbol{F_x}\boldsymbol{F}^{A^{-1}}\boldsymbol{s}_0 \otimes \boldsymbol{f}_0\right);$$

$$\partial_{\boldsymbol{H_x}}W^E = \boldsymbol{0};$$

$$\partial_{J_{\boldsymbol{x}}}W^E = -\frac{a}{3} J_{\boldsymbol{x}}^{-1} \hat{I}\hat{I}^E_{\boldsymbol{F_x}} e^{b\left(\hat{I}\hat{I}^E_{\boldsymbol{F_x}} - 3\right)} + J^{A^{-1}} U'\left(J_{\boldsymbol{x}}^{-1}\right).$$

$$(41)$$

Remark 3. The isotropic invariant isochoric contribution $\hat{W}$ in (18) has been replaced in (39) by its elastic counterpart $\hat{W}^E$. Notice that $\hat{W}^E$ depends upon invariant $\hat{I}\hat{I}^E_{\boldsymbol{F_x}}$ in (40), which can be written as

$$\hat{I}\hat{I}^E_{\boldsymbol{F_x}} = J_{\boldsymbol{x}}^{-2/3} J^{A2/3}\left(\boldsymbol{F_x}\boldsymbol{F}^{A^{-1}}\right) : \left(\boldsymbol{F_x}\boldsymbol{F}^{A^{-1}}\right) = J_{\boldsymbol{x}}^{-2/3} J^{A2/3}\left(\boldsymbol{C}^{A^{-1}} : \boldsymbol{F_x}^T\boldsymbol{F_x}\right), \qquad (42)$$

with $\boldsymbol{C}^{A^{-1}} = \boldsymbol{F}^{A^{-1}}\boldsymbol{F}^{A^{-T}}$. In this case, $\boldsymbol{C}^{A^{-1}}$ plays a similar role to that of a structured tensor used to embed anisotropy.

4.2. Electrophysiology of the heart

The objective of this section is to briefly describe the phenomenological aspects underlying the governing equation (4). Specifically, the definition of the flux vector $\boldsymbol{Q}$ and the source term f_ϕ will be presented. In analogy with the Fick's Law, it is customary [1, 2, 10, 48, 49, 51, 53, 62] to relate $\boldsymbol{Q}$ with the material gradient of the transmembrane potential ϕ as

$$\boldsymbol{Q} = \boldsymbol{D}\boldsymbol{\nabla}_0\phi, \qquad (43)$$

where $\boldsymbol{D}$ represents the second order conductivity tensor [53], defined in terms of the electrical conductivities d_{iso} and d_{ani} [10, 53, 62] as

$$\boldsymbol{D} = d_{\text{iso}} J^{-2} \boldsymbol{H}_{\boldsymbol{x}}^T \boldsymbol{H}_{\boldsymbol{x}} + d_{\text{ani}} \boldsymbol{f}_0 \otimes \boldsymbol{f}_0. \tag{44}$$

The source term f_ϕ depends on the transmembrane potential ϕ, gating variables[5] and ion concentrations [34, 43–45]. Both sets of (scalar) gate and ion concentration variables are represented by the vector $\boldsymbol{q} \in \mathbb{R}^{n_q}$, with n_q the total number of gate numbers and ion concentrations. The evolution equations for $\boldsymbol{q}$ can be mathematically modelled via a set of first order differential equations [1, 2, 34, 48, 49], allowing them to be treated as internal variables, as

$$\dot{\boldsymbol{q}}(\phi) = \boldsymbol{g}(\phi, \boldsymbol{q}(\phi)), \tag{45}$$

with $\boldsymbol{g} : \mathbb{R}^{n_q+1} \to \mathbb{R}^{n_q}$. It is customary to assume an additive decomposition of the source term as

$$f_\phi(\phi) = \tilde{f}_\phi(\phi, \boldsymbol{q}(\phi)); \qquad \tilde{f}_\phi(\phi, \boldsymbol{q}(\phi)) = I_{\text{stim}} + I_{\text{sum}}(\phi, \boldsymbol{q}(\phi)), \tag{46}$$

with $I_{\text{sum}} : \mathbb{R}^{n_q+1} \to \mathbb{R}$. The first term I_{stim} in $(46)_b$ enables the initial propagation of the electrical wave (4). The choice of the ionic model dictates the form of the nonlinear term I_{sum} in $(46)_b$. Two ionic models are considered in this paper. In the first, known as Bueno-Orovio model [1], I_{sum} is defined as

$$I_{\text{sum}} = I_{\text{fi}} + I_{\text{si}} + I_{\text{so}}, \tag{47}$$

where I_{fi}, I_{si} and I_{so} represent three electrical currents which depend linearly on three gating variables[6]. The reader is referred to [1] for the expressions of each of the current contributions of I_{sum} in (47). Finally, the evolution equations for $\boldsymbol{q}$ $(45)_b$, also linear in this case, can be found in [1]. The second model considered, namely the Ten Tusscher model [2, 49], incorporates a more complex representation of I_{sum}, additively decomposed as

$$I_{\text{sum}} = I_{\text{Na}} + I_{\text{bNa}} + I_{\text{NaK}} + I_{\text{NaCa}} + I_{\text{K1}} + I_{\text{Kr}} + I_{\text{Ks}} + I_{\text{pK}} + I_{\text{t0}} + I_{\text{CaL}} + I_{\text{bCa}} + I_{\text{pCa}}, \tag{48}$$

where each electrical current is nonlinearly related to thirteen gating variables and four ion concentrations. The reader is referred to [2, 49] for the expressions of each of the current contributions of I_{sum} in (48). In addition, the evolution equations for $\boldsymbol{q}$ $(45)_b$, can be found in [49].

4.3. Electro-Mechanical activation of the heart

This section presents the mechanism responsible for the coupling between the mechanical physics with the transmembrane potential ϕ. Specifically, evolution equations for T_a and $\gamma_{\boldsymbol{f}_0}$ for both active stress and active strain approaches in Sections 4.1.2 and 4.1.3 will be presented.

4.3.1. Active stress approach

In the case of active stress, the evolution equations for T_a can be expressed as

$$\dot{T}_a = h_{T_a}(\phi, \boldsymbol{q}(\phi)), \tag{49}$$

with $h_{T_a} : \mathbb{R}^{n_q+1} \to \mathbb{R}$. The model proposed by Nash and Panfilov [51] considers the following expression for h_{T_a} (49)

$$h_{T_a} = \varepsilon(u)(k_{T_a} u - T_a); \qquad \varepsilon(u) = \begin{cases} 1 & \text{if } u > 0 \\ 10 & \text{if } u < 0 \end{cases}; \qquad u = \frac{(\phi + 84)}{85.7} \text{(mV)}, \tag{50}$$

---

[5]Gate variables represent the probability of a gate in the cell membrane associated with a specific ion to be open.

[6]Therefore, the vector $\boldsymbol{q}$ exclusively includes these three gating variables.

where k_{T_a} is a constant with dimensions of stress [51]. Alternatively, Wong *et al.* [53] adapted the model in (50) to be used in conjunction with the Ten Tusscher model in (48). In this case, the evolution equation for T_a depends on the calcium concentration c_{Ca} as

$$h_{T_a} = \varepsilon\left(c_{\text{Ca}}\right)\left(\eta\left(c_{\text{Ca}} - c_{\text{Ca},0}\right) - T_a\right); \qquad \varepsilon\left(c_{\text{Ca}}\right) = \varepsilon_0 + \left(\varepsilon_\infty - \varepsilon_0\right)e^A; \qquad A = -e^{-\xi\left(c_{\text{Ca}} - c_{\text{Ca}}^{\text{crit}}\right)}, \quad (51)$$

where $\{\varepsilon_0, \varepsilon_\infty, \xi, \eta\}$ constants and $\{c_{\text{Ca},0}, c_{\text{Ca}}^{\text{crit}}\}$, the resting and critical calcium concentrations respectively (refer to [53]).

4.3.2. Active strain approach

In the case of active strain, the evolution equations for $\gamma_{\boldsymbol{f}_0}$ can be expressed as

$$\dot{\gamma}_{\boldsymbol{f}_0} = h_{\gamma_{\boldsymbol{f}_0}}\left(\phi, \boldsymbol{q}\left(\phi\right)\right), \qquad (52)$$

with $= h_{\gamma_{\boldsymbol{f}_0}} : \mathbb{R}^{n_q+1} \to \mathbb{R}$. In reference [10], Rossi *et al.* proposed the following thermodynamically consistent expression for the function $h_{\gamma_{\boldsymbol{f}_0}}$ in (52)

$$h_{\gamma_{\boldsymbol{f}_0}} = \frac{1}{\hat{\mu}_A c_{\text{Ca}}^2}\left(F_A + \frac{2I_{4,\boldsymbol{f}_0}}{\left(1 + \gamma_{\boldsymbol{f}_0}\right)^3} - 2I_{4,\boldsymbol{f}_0}\right), \qquad (53)$$

where $\hat{\mu}_A$ represents a viscous-type term, c_{Ca} denotes the calcium concentration and F_A is the dimensionless active force along the fibre direction $\boldsymbol{f}_0$, defined as

$$F_A = \alpha\left(c_{\text{Ca}} - c_{\text{Ca},0}\right)^2 \chi_{[l_{\min}, l_{\max}]}\left(\mathcal{F}\left(l\right)\right); \qquad \chi_{[l_{\min}, l_{\max}]}\left(\mathcal{F}\left(l\right)\right) = \begin{cases} \mathcal{F}\left(l\right) & \text{if } l \in [l_{\min}, l_{\max}] \\ 0 & \text{if } l \notin [l_{\min}, l_{\max}] \end{cases};$$

$$l = I_{4,\boldsymbol{f}_0}l_0; \qquad\qquad\qquad \mathcal{F}\left(l\right) = \frac{d_0}{2} + \sum_{n=1}^{3} d_n \cos\left(nl\right) + e_n \sin\left(nl\right). \qquad (54)$$

In (54), α represents the active force of a sarcomere, $c_{\text{Ca},0}$, the resting calcium concentration, $\{l_{\min}, l_{\max}\}$, the minimum and maximum measured sarcomere lengths and $\{d_0, d_n, e_n\}$, constants calibrated to match the experimental data reported in reference [72].

Remark 4. Notice in equations (53) and (54)$_a$ that both $\dot{\gamma}_{\boldsymbol{f}_0}$ and F_A depend on the calcium concentration c_{Ca}. In principle, this precludes the use of the Bueno-Orovio model in (47) as this model does not incorporate ionic concentrations as part of the internal variables $\boldsymbol{q}$ (45). In order to circumvent this drawback, some authors [10] use a simplified approach where the calcium concentration c_{Ca} is assumed to be equivalent to the internal variable s in [1]. This simplification allows the use of the Bueno-Orovio model in conjunction with the active strain approach.

---

5. Variational formulation for cardiac electro-mechanics

5.1. Standard three-field $\boldsymbol{x}$-ϕ-p formulation

In this section, the weak forms associated with the governing equations in Section 3 will be presented for the case of truly incompressibility. These include the conservation of linear momentum equation (3), denoted as $\mathcal{W}_{\boldsymbol{x}}$; the monodomain model for the evolution of the transmembrane potential (4), denoted as $\mathcal{W}_\phi$; and the incompressibility constraint (i.e. $J = 1$), denoted as $\mathcal{W}_p$. In this formulation, the unknown fields are $\{\boldsymbol{x}, \phi, p\} \in \mathbb{V}^{\boldsymbol{x}} \times \mathbb{V}^\phi \times \mathbb{V}^p$, as

$$\begin{aligned} \mathbb{V}^{\boldsymbol{x}} &= \left\{\boldsymbol{x} : \Omega_0 \to \mathbb{R}^3; \quad \left(\boldsymbol{x}\right)_i \in H^1\left(\Omega_0\right)\right\}; \\ \mathbb{V}^\phi &= \left\{\phi : \Omega_0 \to \mathbb{R}; \quad \phi \in H^1\left(\Omega_0\right)\right\}; \\ \mathbb{V}^p &= \left\{p : \Omega_0 \to \mathbb{R}; \quad p \in \mathbb{L}_2\left(\Omega_0\right)\right\}, \end{aligned} \qquad (55)$$

where p represents the Lagrange multiplier field for the weak enforcement of the incompressibility constraint. Let the virtual variations of $\{\boldsymbol{x}, \phi, p\}$ be defined as $\{\delta\boldsymbol{x}, \delta\phi, \delta p\} \in \mathbb{V}_0^{\boldsymbol{x}} \times \mathbb{V}^\phi \times \mathbb{V}^p$, with

$$\mathbb{V}_0^{\boldsymbol{x}} = \{\boldsymbol{x} \in \mathbb{V}^{\boldsymbol{x}}, \quad \boldsymbol{x} = \boldsymbol{0} \text{ on } \partial_{\boldsymbol{x}}\Omega_0\}. \tag{56}$$

The weak forms $\{\mathcal{W}_{\boldsymbol{x}}, \mathcal{W}_\phi, \mathcal{W}_p\}$ can then be written as

$$\mathcal{W}_{\boldsymbol{x}}(\boldsymbol{x}, \phi, p) = \int_{\Omega_0} (\boldsymbol{P} + p\boldsymbol{H}_{\boldsymbol{x}}) : \boldsymbol{\nabla}_0 \delta\boldsymbol{x} \, d\Omega_0 - \int_{\Omega_0} \delta\boldsymbol{x} \cdot \boldsymbol{b}_0 \, d\Omega_0 - \int_{\partial\Omega_0} \delta\boldsymbol{x} \cdot \boldsymbol{t}_0 \, d\Gamma = 0;$$

$$\mathcal{W}_\phi(\boldsymbol{x}, \phi) = \int_{\Omega_0} \delta\phi \frac{\partial\phi}{\partial t} \, d\Omega_0 + \int_{\Omega_0} \boldsymbol{\nabla}_0 \delta\phi \cdot \boldsymbol{Q} \, d\Omega_0 - \int_{\Omega_0} \delta\phi f_\phi \, d\Omega_0 = 0; \tag{57}$$

$$\mathcal{W}_p(\boldsymbol{x}) = \int_{\Omega_0} \delta p \, (J_{\boldsymbol{x}} - 1) \, d\Omega_0 = 0,$$

with $\boldsymbol{P}$ as in (23) for active stress or as in (10) for active strain and with $\boldsymbol{Q}$ defined as in (43)-(44).

5.2. New mixed formulations for cardiac electro-mechanics

Following the work by the authors in [3, 58, 73, 74] in the context of nonlinear elasticity and electro-elasticity, new tailor-made mixed variational formulations will be presented for cardiac electro-mechanics.

5.2.1. Mixed formulation for active stress approach

A new mixed formulation is presented for the active stress approach, named **MFA-T_a**. In this formulation, the unknown fields are $\{\boldsymbol{x}, \phi, p\} \in \mathbb{V}^{\boldsymbol{x}} \times \mathbb{V}^\phi \times \mathbb{V}^p$ (as in the three-field formulation in Section 5.1) and an additional set of fields denoted as $\{\boldsymbol{F}, \boldsymbol{H}, J, \boldsymbol{A}\} \in \mathbb{V}^{\boldsymbol{F}} \times \mathbb{V}^{\boldsymbol{H}} \times \mathbb{V}^J \times \mathbb{V}^{\boldsymbol{A}}$ and their work conjugates $\{\boldsymbol{\Sigma_F}, \boldsymbol{\Sigma_H}, \Sigma_J, \boldsymbol{\Sigma_A}\} \in \mathbb{V}^{\boldsymbol{F}} \times \mathbb{V}^{\boldsymbol{H}} \times \mathbb{V}^J \times \mathbb{V}^{\boldsymbol{A}}$, with

$$\begin{aligned}
\mathbb{V}^{\boldsymbol{F}} &= \left\{\boldsymbol{F} : \Omega_0 \to \mathbb{R}^{3\times3}; \quad (\boldsymbol{F})_{iI} \in \mathbb{L}_2(\Omega_0)\right\}; \\
\mathbb{V}^{\boldsymbol{H}} &= \left\{\boldsymbol{H} : \Omega_0 \to \mathbb{R}^{3\times3}; \quad (\boldsymbol{H})_{iI} \in \mathbb{L}_2(\Omega_0)\right\}; \\
\mathbb{V}^J &= \left\{J : \Omega_0 \to \mathbb{R}; \qquad J \in \mathbb{L}_2(\Omega_0)\right\}; \\
\mathbb{V}^{\boldsymbol{A}} &= \left\{\boldsymbol{H} : \Omega_0 \to \mathbb{R}^3; \qquad (\boldsymbol{A})_I \in \mathbb{L}_2(\Omega_0)\right\},
\end{aligned} \tag{58}$$

where both set of fields are forced to converge weakly to the following set of fields

$$\{\boldsymbol{F}, \boldsymbol{H}, J, \boldsymbol{A}\} \rightharpoonup \{\boldsymbol{F}_{\boldsymbol{x}}, \boldsymbol{H}_{\boldsymbol{x}}, J_{\boldsymbol{x}}, \boldsymbol{\nabla}_0\phi\}; \qquad \{\boldsymbol{\Sigma_F}, \boldsymbol{\Sigma_H}, \Sigma_J, \boldsymbol{\Sigma_A}\} \rightharpoonup \{\partial_{\boldsymbol{F}}W, \partial_{\boldsymbol{H}}W, \partial_J W, \boldsymbol{DA}\}. \tag{59}$$

Notice that equation $(59)_a$ represents the compatibility conditions whereas $(59)_b$ represents the constitutive equations. In this formulation, the weak forms $\{\mathcal{W}_{\boldsymbol{x}}, \mathcal{W}_\phi, \mathcal{W}_p\}$ are expressed as

$$\mathcal{W}_{\boldsymbol{x}}(\boldsymbol{x}, \phi, p, \boldsymbol{F}, \boldsymbol{\Sigma_F}, \boldsymbol{\Sigma_H}, \Sigma_J) = \int_{\Omega_0} (\boldsymbol{P} + p\boldsymbol{H}_{\boldsymbol{x}}) : \boldsymbol{\nabla}_0 \delta\boldsymbol{x} \, d\Omega_0 + \int_{\Omega_0} \delta\boldsymbol{x} \cdot \boldsymbol{b}_0 \, d\Omega_0 - \int_{\partial\Omega_0} \delta\boldsymbol{x} \cdot \boldsymbol{t}_0 \, d\Gamma;$$

$$\mathcal{W}_\phi(\phi, \boldsymbol{\Sigma_A}) = \int_{\Omega_0} \delta\phi \frac{\partial\phi}{\partial t} \, d\Omega_0 + \int_{\Omega_0} \boldsymbol{\nabla}_0 \delta\phi \cdot \boldsymbol{\Sigma_A} \, d\Omega_0 - \int_{\Omega_0} \delta\phi f_\phi \, d\Omega_0;$$

$$\mathcal{W}_p(\boldsymbol{x}) = \int_{\Omega_0} \delta p \, (J_{\boldsymbol{x}} - 1) \, d\Omega_0, \tag{60}$$

where $\boldsymbol{P}$ $(60)_a$ adopts a similar expression to that in (23) but now in terms of the unknown fields $\{\boldsymbol{\Sigma_F}, \boldsymbol{\Sigma_H}, \Sigma_J, \boldsymbol{F}, \boldsymbol{H}, J\}$ as

$$\boldsymbol{P} = \boldsymbol{\Sigma_F} + \boldsymbol{\Sigma_H} \boldsymbol{\times} \boldsymbol{F}_{\boldsymbol{x}} + \Sigma_J \boldsymbol{H}_{\boldsymbol{x}} + T_a(\phi) \boldsymbol{F}\boldsymbol{f}_0 \otimes \boldsymbol{f}_0. \tag{61}$$

Eight additional weak forms denoted as $\{\mathcal{W}_{\boldsymbol{\Sigma}_F}, \mathcal{W}_{\boldsymbol{\Sigma}_H}, \mathcal{W}_{\Sigma_J}, \mathcal{W}_{\boldsymbol{\Sigma}_A}\}$ and $\{\mathcal{W}_F, \mathcal{W}_H, \mathcal{W}_J, \mathcal{W}_F\}$ enforcing equation (59) are part of this formulation and are defined as

$$\mathcal{W}_{\boldsymbol{\Sigma}_F}(\boldsymbol{x}, \boldsymbol{F}) = \int_{\Omega_0} \delta\boldsymbol{\Sigma}_F : (\boldsymbol{F}_x - \boldsymbol{F})\, d\Omega_0; \qquad \mathcal{W}_F(\boldsymbol{F}, \boldsymbol{H}, J, \boldsymbol{\Sigma}_F) = \int_{\Omega_0} \delta\boldsymbol{F} : (\partial_F W - \boldsymbol{\Sigma}_F)\, d\Omega_0;$$

$$\mathcal{W}_{\boldsymbol{\Sigma}_H}(\boldsymbol{x}, \boldsymbol{H}) = \int_{\Omega_0} \delta\boldsymbol{\Sigma}_H : (\boldsymbol{H}_x - \boldsymbol{H})\, d\Omega_0; \qquad \mathcal{W}_H(\boldsymbol{F}, \boldsymbol{H}, J, \boldsymbol{\Sigma}_H) = \int_{\Omega_0} \delta\boldsymbol{H} : (\partial_H W - \boldsymbol{\Sigma}_H)\, d\Omega_0;$$

$$\mathcal{W}_{\Sigma_J}(\boldsymbol{x}, J) = \int_{\Omega_0} \delta\Sigma_J\, (J_x - J)\, d\Omega_0; \qquad \mathcal{W}_J(\boldsymbol{F}, \boldsymbol{H}, J, \Sigma_J) = \int_{\Omega_0} \delta J\, (\partial_J W - \Sigma_J)\, d\Omega_0;$$

$$\mathcal{W}_{\boldsymbol{\Sigma}_A}(\phi, \boldsymbol{A}) = \int_{\Omega_0} \delta\boldsymbol{\Sigma}_A \cdot (\boldsymbol{\nabla}_0\phi - \boldsymbol{A})\, d\Omega_0; \qquad \mathcal{W}_A(\boldsymbol{H}, J, \boldsymbol{A}, \boldsymbol{\Sigma}_A) = \int_{\Omega_0} \delta\boldsymbol{A} \cdot (\boldsymbol{D}\boldsymbol{A} - \boldsymbol{\Sigma}_A)\, d\Omega_0, \tag{62}$$

where the strain energy W depends on the fields $\{\boldsymbol{F}, \boldsymbol{H}, J\}$ and not on $\{\boldsymbol{F}_x, \boldsymbol{H}_x, J_x\}$ as in (5). Moreover, $\{\delta\boldsymbol{F}, \delta\boldsymbol{H}, \delta J, \delta\boldsymbol{A}\} \in \mathbb{V}^F \times \mathbb{V}^H \times \mathbb{V}^J \times \mathbb{V}^A$ and $\{\delta\boldsymbol{\Sigma}_F, \delta\boldsymbol{\Sigma}_H, \delta\Sigma_J, \delta\boldsymbol{\Sigma}_A\} \in \mathbb{V}^F \times \mathbb{V}^H \times \mathbb{V}^J \times \mathbb{V}^A$ in (62). Finally, $\boldsymbol{D}$ in $(62)_i$ adopts an equivalent expression to that in (44) in terms of $\{\boldsymbol{H}, J\}$ as

$$\boldsymbol{D}(\boldsymbol{H}, J) = d_{\mathrm{iso}} J^{-2} \boldsymbol{H}^T \boldsymbol{H} + d_{\mathrm{ani}} \boldsymbol{f}_0 \otimes \boldsymbol{f}_0. \tag{63}$$

5.2.2. Mixed formulation for active strain approach

The mixed formulation presented in Section 5.2.1 will be adapted to the active strain approach in this section. In this formulation, named as **MFA-γ**, the weak forms $\mathcal{W}_\phi$ and $\mathcal{W}_p$ are completely equivalent to those in (60). However, the multiplicative nature of the deformation gradient tensor in (28) introduces a different dependence of the weak form $\mathcal{W}_x$ which, on the contrary to its counterpart in (60), does not depend on the fields $\{\phi, \boldsymbol{F}\}$, i.e.

$$\mathcal{W}_x(\boldsymbol{x}, p, \boldsymbol{\Sigma}_F, \boldsymbol{\Sigma}_H, \Sigma_J) = \int_{\Omega_0} (\boldsymbol{P} + p\boldsymbol{H}_x) : \boldsymbol{\nabla}_0 \delta\boldsymbol{x}\, d\Omega_0 + \int_{\Omega_0} \delta\boldsymbol{x} \cdot \boldsymbol{b}_0\, d\Omega_0 - \int_{\partial\Omega_0} \delta\boldsymbol{x} \cdot \boldsymbol{t}_0\, d\Gamma, \tag{64}$$

where $\boldsymbol{P}$ is now expressed similarly to (10) as

$$\boldsymbol{P} = \boldsymbol{\Sigma}_F + \boldsymbol{\Sigma}_H \times \boldsymbol{F}_x + \Sigma_J \boldsymbol{H}_x. \tag{65}$$

For this formulation, the weak forms (and their dependence) associated with the compatibility equations, namely $\{\mathcal{W}_{\boldsymbol{\Sigma}_F}, \mathcal{W}_{\boldsymbol{\Sigma}_H}, \mathcal{W}_{\Sigma_J}, \mathcal{W}_{\boldsymbol{\Sigma}_A}\}$, are equivalent to those in the active stress approach in (62). However, the multiplicative nature of the deformation gradient tensor in (28) introduces a different dependence of the weak forms associated with the constitutive equations, namely

$$\mathcal{W}_F(\phi, \boldsymbol{F}, \boldsymbol{H}, J, \boldsymbol{\Sigma}_F) = \int_{\Omega_0} \delta\boldsymbol{F} : \left(\partial_F W^E - \boldsymbol{\Sigma}_F\right) d\Omega_0;$$

$$\mathcal{W}_H(\phi, \boldsymbol{F}, \boldsymbol{H}, J, \boldsymbol{\Sigma}_H) = \int_{\Omega_0} \delta\boldsymbol{H} : \left(\partial_H W^E - \boldsymbol{\Sigma}_H\right) d\Omega_0; \tag{66}$$

$$\mathcal{W}_J(\phi, \boldsymbol{F}, \boldsymbol{H}, J, \Sigma_J) = \int_{\Omega_0} \delta J \left(\partial_J W^E - \Sigma_J\right) d\Omega_0,$$

where W^E depends on the fields $\{\boldsymbol{F}, \boldsymbol{H}, J, \boldsymbol{F}^A, \boldsymbol{H}^A, J^A\}$ and not on $\{\boldsymbol{F}_x, \boldsymbol{H}_x, J_x, \boldsymbol{F}^A, \boldsymbol{H}^A, J^A\}$ as in (35). Notice in above equation (66) the extra dependence with respect to the field ϕ (due to the dependence of W with respect to the active contribution of the deformation gradient tensor $\boldsymbol{F}^A$, see equation (28)) in contrast to those in (60).

6. Computational implementation

6.1. General remarks

As standard in Finite Elements, the domain Ω_0 described in Section 2 and representing the myocardium is sub-divided into a finite of non-overlapping elements $e \in \mathbb{E}$ such that

$$\Omega_0 \approx \Omega_0^h = \bigcup_{e \in \mathbb{E}} \Omega_0^e. \tag{67}$$

The unknown fields in the mixed formulations in Sections 5.2.1 band 5.2.2 are discretised using the following functional spaces $\{\boldsymbol{x}, \phi, p\} \in \mathbb{V}^{\boldsymbol{x}^h} \times \mathbb{V}^{\phi^h} \times \mathbb{V}^{p^h}$ and $\{\boldsymbol{F}, \boldsymbol{H}, J, \boldsymbol{A}\} \in \mathbb{V}^{\boldsymbol{F}^h} \times \mathbb{V}^{\boldsymbol{H}^h} \times \mathbb{V}^{J^h} \times \mathbb{V}^{\boldsymbol{A}^h}$ and $\{\boldsymbol{\Sigma}_{\boldsymbol{F}}, \boldsymbol{\Sigma}_{\boldsymbol{H}}, \Sigma_J, \boldsymbol{\Sigma}_{\boldsymbol{A}}\} \in \mathbb{V}^{\boldsymbol{F}^h} \times \mathbb{V}^{\boldsymbol{H}^h} \times \mathbb{V}^{J^h} \times \mathbb{V}^{\boldsymbol{A}^h}$, with

$$
\begin{aligned}
\mathbb{V}^{\boldsymbol{x}^h} &= \Big\{\boldsymbol{x} \in \mathbb{V}^{\boldsymbol{x}}; \quad \boldsymbol{x} = \sum_{a=1}^{n_{\boldsymbol{x}}} \boldsymbol{x}_a N_a^{\boldsymbol{x}}\Big\}; & \mathbb{V}^{\phi^h} &= \Big\{\phi^h \in \mathbb{V}^{\phi}; \quad \phi = \sum_{a=1}^{n_{\phi}} \phi_a N_a^{\phi}\Big\}; \\
\mathbb{V}^{p^h} &= \Big\{p^h \in \mathbb{V}^{p}; \quad p = \sum_{a=1}^{n_p} p_a N_a^{p}\Big\}; & \mathbb{V}^{\boldsymbol{F}^h} &= \Big\{\boldsymbol{F}^h \in \mathbb{V}^{\boldsymbol{F}}; \quad \boldsymbol{F} = \sum_{a=1}^{n_{\boldsymbol{F}}} \boldsymbol{F}_a N_a^{\boldsymbol{F}}\Big\}; \\
\mathbb{V}^{\boldsymbol{H}^h} &= \Big\{\boldsymbol{H}^h \in \mathbb{V}^{\boldsymbol{H}}; \quad \boldsymbol{H} = \sum_{a=1}^{n_{\boldsymbol{H}}} \boldsymbol{H}_a N_a^{\boldsymbol{H}}\Big\}; & \mathbb{V}^{J^h} &= \Big\{J^h \in \mathbb{V}^{J}; \quad J = \sum_{a=1}^{n_J} J_a N_a^{J}\Big\}; \\
\mathbb{V}^{\boldsymbol{A}^h} &= \Big\{\boldsymbol{A}^h \in \mathbb{V}^{\boldsymbol{A}}; \quad \boldsymbol{A} = \sum_{a=1}^{n_{\boldsymbol{A}}} \boldsymbol{A}_a N_a^{\boldsymbol{A}}\Big\},
\end{aligned}
\tag{68}
$$

where a denotes the nodes used for the interpolation of the above variables and $n_{(\bullet)}$, the number of nodes associated with the variable $(\bullet)$. The functional spaces used for the virtual (and incremental) variations of the unknown fields are $\{\delta\boldsymbol{x}, \delta\phi, \delta p\} \in \mathbb{V}_0^{\boldsymbol{x}^h} \times \mathbb{V}^{\phi^h} \times \mathbb{V}^{p^h}$ and $\{\delta\boldsymbol{F}, \delta\boldsymbol{H}, \delta J, \delta\boldsymbol{A}\} \in \mathbb{V}^{\boldsymbol{F}^h} \times \mathbb{V}^{\boldsymbol{H}^h} \times \mathbb{V}^{J^h} \times \mathbb{V}^{\boldsymbol{A}^h}$ and $\{\delta\boldsymbol{\Sigma}_{\boldsymbol{F}}, \delta\boldsymbol{\Sigma}_{\boldsymbol{H}}, \delta\Sigma_J, \delta\boldsymbol{\Sigma}_{\boldsymbol{A}}\} \in \mathbb{V}^{\boldsymbol{F}^h} \times \mathbb{V}^{\boldsymbol{H}^h} \times \mathbb{V}^{J^h} \times \mathbb{V}^{\boldsymbol{A}^h}$, with

$$\mathbb{V}_0^{\boldsymbol{x}^h} = \{\boldsymbol{x} \in \mathbb{V}^{\boldsymbol{x}^h}; \quad \boldsymbol{x} = \boldsymbol{0}; \text{ on } \partial_t \Omega_0\}. \tag{69}$$

In order to avoid an excessive computational cost associated with the large number of unknown fields in this mixed formulation, a piecewise discontinuous interpolation of the fields $\{\boldsymbol{F}, \boldsymbol{H}, J, \boldsymbol{A}\}$ and $\{\boldsymbol{\Sigma}_{\boldsymbol{F}}, \boldsymbol{\Sigma}_{\boldsymbol{H}}, \Sigma_J, \boldsymbol{\Sigma}_{\boldsymbol{A}}\}$ is carried out in this work, which enables to condense out these fields using standard static condensation procedure. Specifically, two new Finite Elements have been used in this work, denoted as ELEM1 and ELEM2. In the first, a quadratic tetrahedral element for $\boldsymbol{x}$ and ϕ is used in conjunction with a discontinuous linear interpolation for the fields $\{\boldsymbol{F}, \boldsymbol{H}, \boldsymbol{A}\}$ and their work conjugates and a constant interpolation for $\{J, \Sigma_J, p\}$. In the second, a quadratic tetrahedral element for $\boldsymbol{x}$ and ϕ where only the interpolation of $\boldsymbol{x}$ is enhanced with five bubble functions in analogy to the $P_2^+ P_1^D$ Crouzeix-Raviart [75, 76]. Additionaly, a discontinuous quadratic interpolation is used for the fields $\{\boldsymbol{F}, \boldsymbol{H}\}$ and their work conjugates and a linear interpolation for all the remaining fields. Notice that the superscript D in the definition of both elements is associated with the discontinuous nature of a particular field. Figure 4 summarises the different Finite Element spaces employed for both elements.

6.2. Finite Element semi-discretisation

In this section, the Finite Element implementation of the set of weak forms associated with the mixed formulation **MFA-γ** in Section 5.2.2 will be presented. Standard Finite Element discretisation enables the discrete form of the weak forms $\{\mathcal{W}_{\boldsymbol{x}}, \mathcal{W}_{\phi}, \mathcal{W}_p\}$ in (60) to be expressed as

$$\mathcal{W}_{\boldsymbol{x}} = \sum_{a=1}^{n_{\boldsymbol{x}}} \boldsymbol{R}_{\boldsymbol{x}}^a \cdot \delta\boldsymbol{x}^a; \qquad \mathcal{W}_{\phi} = \sum_{a=1}^{n_{\phi}} R_{\phi}^a \delta\phi^a; \qquad \mathcal{W}_p = \sum_{a=1}^{n_p} R_p^a \delta p^a; \tag{70}$$

15

ELEM1	
$\boldsymbol{x}$	P_2
ϕ	P_2
p	P_0
$\{\boldsymbol{F}, \boldsymbol{\Sigma_F}\}$	P_1^D
$\{\boldsymbol{H}, \boldsymbol{\Sigma_H}\}$	P_1^D
$\{J, \Sigma_J\}$	P_0
$\{\boldsymbol{A}, \boldsymbol{\Sigma_A}\}$	P_1^D

ELEM2	
$\boldsymbol{x}$	P_2^+
ϕ	P_2
p	P_1^D
$\{\boldsymbol{F}, \boldsymbol{\Sigma_F}\}$	P_2^D
$\{\boldsymbol{H}, \boldsymbol{\Sigma_H}\}$	P_2^D
$\{J, \Sigma_J\}$	P_1^D
$\{\boldsymbol{A}, \boldsymbol{\Sigma_A}\}$	P_1^D

Figure 4: Summary of the interpolation types for each variable in the different mixed variables formulations assessed in this manuscript. The superscript + denotes the use of a Crouzeix-Raviart element type [75].

with the associated residuals $R_{\boldsymbol{x}}^a$, R_ϕ^a and R_p^a defined as

$$
\boldsymbol{R}_{\boldsymbol{x}}^a = \int_{\Omega_0} (\boldsymbol{P} + p\boldsymbol{H_x})\, \boldsymbol{\nabla}_0 N_{\boldsymbol{x}}^a \, d\Omega_0 + \int_{\Omega_0} N_{\boldsymbol{x}}^a \boldsymbol{b}_0 \, d\Omega_0 - \int_{\partial\Omega_0} N_{\boldsymbol{x}}^a \boldsymbol{t}_0 \, d\Gamma;
$$

$$
R_\phi^a = \int_{\Omega_0} N_\phi^a \frac{\partial\phi}{\partial t} \, d\Omega_0 + \int_{\Omega_0} \boldsymbol{\nabla}_0 N_\phi^a \cdot \boldsymbol{\Sigma_A} \, d\Omega_0 - \int_{\Omega_0} N_\phi^a f_\phi \, d\Omega_0; \tag{71}
$$

$$
R_p^a = \int_{\Omega_0} N_p^a (J_{\boldsymbol{x}} - 1) \, d\Omega_0.
$$

Similarly, the discrete form of the compatibility equations and the constitutive equations enables their associated residuals $\{\boldsymbol{R}_{\boldsymbol{\Sigma_F}}, \boldsymbol{R}_{\boldsymbol{\Sigma_H}}, R_{\Sigma_J}, \boldsymbol{R}_{\boldsymbol{\Sigma_A}}\}$ and $\{\boldsymbol{R_F}, \boldsymbol{R_H}, R_J, \boldsymbol{R_A}\}$ to be defined as

$$
\boldsymbol{R}_{\boldsymbol{\Sigma_F}}^a = \int_{\Omega_0} N_{\boldsymbol{F}}^a (\boldsymbol{F_x} - \boldsymbol{F}) \, d\Omega_0; \qquad \boldsymbol{R}_{\boldsymbol{F}}^a = \int_{\Omega_0} N_{\boldsymbol{F}}^a (\partial_{\boldsymbol{F}} W - \boldsymbol{\Sigma_F}) \, d\Omega_0;
$$

$$
\boldsymbol{R}_{\boldsymbol{\Sigma_H}}^a = \int_{\Omega_0} N_{\boldsymbol{H}}^a (\boldsymbol{H_x} - \boldsymbol{H}) \, d\Omega_0; \qquad \boldsymbol{R}_{\boldsymbol{H}}^a = \int_{\Omega_0} N_{\boldsymbol{H}}^a (\partial_{\boldsymbol{H}} W - \boldsymbol{\Sigma_H}) \, d\Omega_0;
$$

$$
R_{\Sigma_J}^a = \int_{\Omega_0} N_J^a (J_{\boldsymbol{x}} - J) \, d\Omega_0; \qquad R_J^a = \int_{\Omega_0} N_J^a (\partial_J W - \Sigma_J) \, d\Omega_0; \tag{72}
$$

$$
\boldsymbol{R}_{\boldsymbol{\Sigma_A}}^a = \int_{\Omega_0} N_{\boldsymbol{A}}^a (\boldsymbol{\nabla}_0 \phi - \boldsymbol{A}) \, d\Omega_0; \qquad \boldsymbol{R}_{\boldsymbol{A}}^a = \int_{\Omega_0} N_{\boldsymbol{A}}^a (\boldsymbol{DA} - \boldsymbol{\Sigma_A}) \, d\Omega_0.
$$

Let us denote $\boldsymbol{\mathcal{U}} = \{\boldsymbol{x}, \phi, p, \boldsymbol{\mathcal{Y}}, \boldsymbol{\Sigma_{\mathcal{Y}}}\}$, with $\boldsymbol{\mathcal{Y}} = \{\boldsymbol{F}, \boldsymbol{H}, J, \boldsymbol{A}\}$ and $\boldsymbol{\Sigma_{\mathcal{Y}}} = \{\boldsymbol{\Sigma_F}, \boldsymbol{\Sigma_H}, \Sigma_J, \boldsymbol{\Sigma_A}\}$. Consistent linearisation of the above residuals with respect to the incremental variations $\Delta\boldsymbol{\mathcal{U}}$ leads to the following Newton-Raphson-based update algorithm

$$
\boldsymbol{K}(\boldsymbol{\mathcal{U}}_k)\, \Delta\boldsymbol{\mathcal{U}} = -\boldsymbol{R}(\boldsymbol{\mathcal{U}}_k); \qquad \boldsymbol{\mathcal{U}}_{k+1} = \boldsymbol{\mathcal{U}}_k + \Delta\boldsymbol{\mathcal{U}}, \tag{73}
$$

where the stiffness matrix $\boldsymbol{K}$, emerging as a result of the consistent linearisation of the residuals in equations (71) and (72), before static condensation is carried out can be expressed as

$$
\boldsymbol{K} = \begin{bmatrix} \boldsymbol{K}_{\boldsymbol{xx}} & \boldsymbol{0} & \boldsymbol{K}_{\boldsymbol{x}p} & \boldsymbol{0} & \boldsymbol{K}_{\boldsymbol{x}\Sigma_{\mathcal{Y}}} \\ \boldsymbol{0} & \boldsymbol{K}_{\phi\phi} & \boldsymbol{0} & \boldsymbol{0} & \boldsymbol{K}_{\phi\Sigma_{\mathcal{Y}}} \\ \boldsymbol{K}_{\boldsymbol{x}p}^T & \boldsymbol{0} & \boldsymbol{0} & \boldsymbol{0} & \boldsymbol{0} \\ \boldsymbol{0} & \boldsymbol{K}_{\boldsymbol{\mathcal{Y}}\phi} & \boldsymbol{0} & \boldsymbol{K}_{\boldsymbol{\mathcal{Y}}\boldsymbol{\mathcal{Y}}} & \boldsymbol{K}_{\boldsymbol{\mathcal{Y}}\Sigma_{\mathcal{Y}}} \\ \boldsymbol{K}_{\boldsymbol{x}\Sigma_{\mathcal{Y}}}^T & \boldsymbol{K}_{\phi\Sigma_{\mathcal{Y}}}^T & \boldsymbol{0} & \boldsymbol{K}_{\boldsymbol{\mathcal{Y}}\Sigma_{\mathcal{Y}}}^T & \boldsymbol{0} \end{bmatrix}. \tag{74}
$$

The expression of each of the components of $\boldsymbol{K}$ in above equation (74) will be presented in the following derivations. As shown in reference [60], the stiffness matrix $\boldsymbol{K}_{\boldsymbol{xx}}$, corresponding to

the linearisation of $\boldsymbol{R}_{\boldsymbol{x}}^a$ in $(71)_a$ with respect to $\Delta \boldsymbol{x}$ is obtained as

$$\boldsymbol{K}_{\boldsymbol{xx}}^{ab} = \boldsymbol{\mathcal{E}} : \int_{\Omega_0} \left(\boldsymbol{\Sigma_H} + (\Sigma_J + p) \, \boldsymbol{F_x} \right) \left(\boldsymbol{\nabla}_0 N_{\boldsymbol{x}}^a \times \boldsymbol{\nabla}_0 N_{\boldsymbol{x}}^b \right) d\Omega_0. \tag{75}$$

In addition, the linearisation of $\boldsymbol{R}_{\boldsymbol{x}}$ with respect to Δp leads to the stiffness matrix contribution $\boldsymbol{K}_{\boldsymbol{x}p}$, obtained as

$$\boldsymbol{K}_{\boldsymbol{x}p}^{ab} = \int_{\Omega_0} N_p^b \left(\boldsymbol{H_x} \boldsymbol{\nabla}_0 N_{\boldsymbol{x}}^a \right) d\Omega_0. \tag{76}$$

Moreover, the linearisation of this residual, namely $\boldsymbol{R}_{\boldsymbol{x}}$, with respect to the set $\boldsymbol{\Sigma_y}$ leads to the stiffness contribution $\boldsymbol{K}_{\boldsymbol{x}\boldsymbol{\Sigma_y}}$ defined as

$$\boldsymbol{K}_{\boldsymbol{x}\boldsymbol{\Sigma_y}}^{ab} = \int_{\Omega_0} \left[\begin{array}{cccc} \left(\boldsymbol{I} \otimes \boldsymbol{\nabla}_0 N_{\boldsymbol{x}}^a \right) N_{\boldsymbol{F}}^b & \mathcal{E}_{ijk} \left[\left(\boldsymbol{F_x} \boldsymbol{\times} \boldsymbol{\nabla}_0 N_{\boldsymbol{x}}^a \right) N_{\boldsymbol{H}}^b \right]_{kI} & N_J^b \left(\boldsymbol{H_x} \boldsymbol{\nabla}_0 N_{\boldsymbol{x}}^a \right) & \boldsymbol{0} \end{array} \right] d\Omega_0. \tag{77}$$

The linearisation of the residual $\boldsymbol{R}_{\phi}$ in equation $(71)_b$ leads to the stiffness contribution $\boldsymbol{K}_{\phi\phi}$. In the case of using a backward-Euler time integrator for the (time dependent) first term on the right hand side of this equation, $\boldsymbol{K}_{\phi\phi}$ can be obtained as

$$\boldsymbol{K}_{\phi\phi}^{ab} = \int_{\Omega_0} N_{\phi}^a N_{\phi}^b \frac{1}{\Delta t} d\Omega_0 + \int_{\Omega_0} N_{\phi}^a N_{\phi}^b \frac{Df_{\phi}}{D\phi} d\Omega_0, \tag{78}$$

where the derivation of $\frac{Df_{\phi}}{D\phi}$ can be found in Remark 4. . In addition, the linearisation of residual $\boldsymbol{R}_{\phi}$ respect to to the work conjugate $\boldsymbol{\Sigma_A}$ leads to the following expression

$$\boldsymbol{K}_{\phi\boldsymbol{\Sigma_A}}^{ab} = \int_{\Omega_0} \boldsymbol{\nabla}_0 N_{\phi}^a N_{\boldsymbol{A}}^b d\Omega_0. \tag{79}$$

Linearisation of the residual $\boldsymbol{R}_{\boldsymbol{y}}$ with respect to $\boldsymbol{\Sigma_y}$ leads to the stiffness $\boldsymbol{K}_{\boldsymbol{y}\boldsymbol{\Sigma_y}}$, defined as

$$\boldsymbol{K}_{\boldsymbol{y}\boldsymbol{\Sigma_y}}^{ab} = -\int_{\Omega_0} \left[\begin{array}{cccc} N_{\boldsymbol{F}}^a N_{\boldsymbol{F}}^b \boldsymbol{\mathcal{I}} & \boldsymbol{0} & \boldsymbol{0} & \boldsymbol{0} \\ \boldsymbol{0} & N_{\boldsymbol{H}}^a N_{\boldsymbol{H}}^b \boldsymbol{\mathcal{I}} & \boldsymbol{0} & \boldsymbol{0} \\ \boldsymbol{0} & \boldsymbol{0} & N_J^a N_J^b & \boldsymbol{0} \\ \boldsymbol{0} & \boldsymbol{0} & \boldsymbol{0} & N_{\boldsymbol{A}}^a N_{\boldsymbol{A}}^b \boldsymbol{I} \end{array} \right] d\Omega_0, \tag{80}$$

where $\boldsymbol{\mathcal{I}}$ represents the fourth order identity tensor $\mathcal{I}_{iIjJ} = \delta_{ij}\delta_{IJ}$ and $\boldsymbol{I}$, the second order identity tensor. Linearisation of the residual $\boldsymbol{R}_{\boldsymbol{y}}$ with respect to $\boldsymbol{\mathcal{Y}}$ leads to the stiffness $\boldsymbol{K}_{\boldsymbol{y}\boldsymbol{y}}$, defined as

$$\boldsymbol{K}_{\boldsymbol{y}\boldsymbol{y}}^{ab} = -\int_{\Omega_0} \left[\begin{array}{cccc} N_{\boldsymbol{F}}^a N_{\boldsymbol{F}}^b W_{\boldsymbol{FF}} & N_{\boldsymbol{F}}^a N_{\boldsymbol{H}}^b W_{\boldsymbol{FH}} & N_{\boldsymbol{F}}^a N_J^b W_{\boldsymbol{F}J} & \boldsymbol{0} \\ N_{\boldsymbol{H}}^a N_{\boldsymbol{F}}^b W_{\boldsymbol{HF}} & N_{\boldsymbol{H}}^a N_{\boldsymbol{H}}^b W_{\boldsymbol{HH}} & N_{\boldsymbol{H}}^a N_J^b W_{\boldsymbol{H}J} & \boldsymbol{0} \\ N_J^a N_{\boldsymbol{F}}^b W_{J\boldsymbol{F}} & N_J^a N_{\boldsymbol{H}}^b W_{J\boldsymbol{H}} & N_J^a N_J^b W_{JJ} & \boldsymbol{0} \\ \boldsymbol{0} & \boldsymbol{k_{AH}} & \boldsymbol{k_{A}}_J & N_{\boldsymbol{A}}^a N_{\boldsymbol{A}}^b \boldsymbol{Q} \end{array} \right] d\Omega_0, \tag{81}$$

where $W_{\boldsymbol{BC}} = \frac{\partial^2 W}{\partial \boldsymbol{B} \partial \boldsymbol{C}}$ with $\boldsymbol{B}$ and $\boldsymbol{C}$ any of the fields of the set $\{\boldsymbol{F}, \boldsymbol{H}, J\}$. Moreover, $\boldsymbol{k_{AH}}$ and $\boldsymbol{k_{A}}_J$ in above equation are obtained as

$$[\boldsymbol{k_{AH}}]_{IjJ} = d_{\text{iso}} J^{-2} N_{\boldsymbol{A}}^a N_{\boldsymbol{H}}^b \left(H_{jI} A_J + \delta_{IJ} [\boldsymbol{H} \boldsymbol{A}]_j \right); \qquad \boldsymbol{k_{A}}_J = -2d_{\text{iso}} J^{-3} N_{\boldsymbol{A}}^a N_J^b \left(\boldsymbol{H}^T \boldsymbol{H} \boldsymbol{A} \right). \tag{82}$$

Finally, the non-vanishing $(\boldsymbol{K_{A\phi}} = \boldsymbol{0})$ contributions of the stiffness $\boldsymbol{K}_{\boldsymbol{y}\phi}$ are obtained as

$$\boldsymbol{K}_{\boldsymbol{F}\phi}^{ab} = \int_{\Omega_0} N_{\boldsymbol{F}}^a N_{\phi}^b W_{\boldsymbol{FF^A}} : \boldsymbol{U} d\Omega_0; \quad \boldsymbol{K}_{\boldsymbol{H}\phi}^{ab} = \int_{\Omega_0} N_{\boldsymbol{H}}^a N_{\phi}^b W_{\boldsymbol{HF^A}} : \boldsymbol{U} d\Omega_0; \quad \boldsymbol{K}_{J\phi}^{ab} = \int_{\Omega_0} N_J^a N_{\phi}^b W_{J\boldsymbol{F^A}} : \boldsymbol{U} d\Omega_0, \tag{83}$$

where the second order tensor $\boldsymbol{U}$ is expressed as

$$\boldsymbol{U} = \frac{D\boldsymbol{F}^A}{D\gamma_{\boldsymbol{f}_0}} \frac{D\gamma_{\boldsymbol{f}_0}}{D\phi}, \tag{84}$$

where the derivation of $\frac{D\gamma_{\boldsymbol{f}_0}}{D\phi}$ can be found in Remark 5.

Remark 5. Time integration of equation (52) via the implicit first order in time Backward Euler scheme enables to $\gamma_{\boldsymbol{f}_0}$ at current time step t_{n+1} as

$$\gamma_{\boldsymbol{f}_0}(t_{n+1}) = \gamma_{\boldsymbol{f}_0}(t_n) + \Delta t h_{\gamma_{\boldsymbol{f}_0}}(\phi(t_{n+1}), \boldsymbol{q}(\phi(t_{n+1}))), \tag{85}$$

where Δt represents the magnitude of the time step used. The total derivative of both the source term f_ϕ in (46) and $\gamma_{\boldsymbol{f}_0}$ in (52) in (85) leads to

$$\frac{Df_\phi}{D\phi} = \frac{\partial f_\phi}{\partial \phi} + \frac{\partial f_\phi}{\partial \boldsymbol{q}} \cdot \frac{\partial \boldsymbol{q}}{\partial \phi}; \qquad \frac{D\gamma_{\boldsymbol{f}_0}}{D\phi} = \frac{\partial h_{\gamma_{\boldsymbol{f}_0}}}{\partial \phi} + \frac{\partial h_{\gamma_{\boldsymbol{f}_0}}}{\partial \boldsymbol{q}} \cdot \frac{\partial \boldsymbol{q}}{\partial \phi}. \tag{86}$$

The only field that remains to be determined in (86) is $\frac{\partial \boldsymbol{q}}{\partial \phi}$. Time integration of (45) via the implicit first order in time Backward Euler scheme enables to obtain $\boldsymbol{q}$ at t_{n+1} as

$$\boldsymbol{q}(t_{n+1}) = \boldsymbol{q}(t_n) + \Delta t \boldsymbol{g}(\phi(t_{n+1}), \boldsymbol{q}(t_{n+1})). \tag{87}$$

Differentiation with respect to ϕ in (87) enables to obtain $\frac{\partial \boldsymbol{q}}{\partial \phi}$ as

$$\frac{\partial \boldsymbol{q}}{\partial \phi} = \Delta t \left(\frac{\partial \boldsymbol{g}}{\partial \phi} + \frac{\partial \boldsymbol{g}}{\partial \boldsymbol{q}} \frac{\partial \boldsymbol{q}}{\partial \phi} \right) \rightarrow \frac{\partial \boldsymbol{q}}{\partial \phi} = \Delta t \left(\boldsymbol{I}_{n_{\boldsymbol{q}} \times n_{\boldsymbol{q}}} - \frac{\partial \boldsymbol{g}}{\partial \boldsymbol{q}} \right)^{-1} \frac{\partial \boldsymbol{g}}{\partial \phi}. \tag{88}$$

6.2.1. Static condensation

In order to use the static condensation procedure for a given element e, the system of equations can be expressed as

$$\begin{bmatrix} \boldsymbol{K}_{\boldsymbol{xx}}^e & \boldsymbol{0} & \boldsymbol{K}_{\boldsymbol{xp}}^e & \boldsymbol{0} & \boldsymbol{K}_{\boldsymbol{x}\Sigma_{\boldsymbol{y}}}^e \\ \boldsymbol{0} & \boldsymbol{K}_{\phi\phi}^e & \boldsymbol{0} & \boldsymbol{0} & \boldsymbol{K}_{\phi\Sigma_{\boldsymbol{y}}}^e \\ [\boldsymbol{K}_{\boldsymbol{xp}}^e]^T & \boldsymbol{0} & \boldsymbol{0} & \boldsymbol{0} & \boldsymbol{0} \\ \boldsymbol{0} & \boldsymbol{K}_{\boldsymbol{y}\phi}^e & \boldsymbol{0} & \boldsymbol{K}_{\boldsymbol{yy}}^e & \boldsymbol{K}_{\boldsymbol{y}\Sigma_{\boldsymbol{y}}}^e \\ [\boldsymbol{K}_{\boldsymbol{x}\Sigma_{\boldsymbol{y}}}^e]^T & \boldsymbol{K}_{\Sigma_{\boldsymbol{y}}\phi}^e & \boldsymbol{0} & [\boldsymbol{K}_{\boldsymbol{y}\Sigma_{\boldsymbol{y}}}^e]^T & \boldsymbol{0} \end{bmatrix} \begin{bmatrix} \Delta\boldsymbol{x}^e \\ \Delta\phi^e \\ \Delta p^e \\ \Delta\boldsymbol{\mathcal{Y}}^e \\ \Delta\boldsymbol{\Sigma}_{\boldsymbol{y}}^e \end{bmatrix} = - \begin{bmatrix} \boldsymbol{R}_{\boldsymbol{x}}^e \\ \boldsymbol{R}_{\phi}^e \\ \boldsymbol{R}_p^e \\ \boldsymbol{R}_{\boldsymbol{y}}^e \\ \boldsymbol{R}_{\Sigma_{\boldsymbol{y}}}^e \end{bmatrix}. \tag{89}$$

Replacing the values of $\Delta\boldsymbol{\mathcal{Y}}^e$ and $\Delta\boldsymbol{\Sigma}_{\boldsymbol{y}}^e$ from the fourth and fifth rows in above equation (89), enables to rewrite the element system of equations as

$$\begin{bmatrix} \bar{\boldsymbol{K}}_{\boldsymbol{xx}}^e & \bar{\boldsymbol{K}}_{\boldsymbol{x}\phi}^e & \boldsymbol{K}_{\boldsymbol{xp}}^e \\ \bar{\boldsymbol{K}}_{\phi\boldsymbol{x}}^e & \bar{\boldsymbol{K}}_{\phi\phi}^e & \boldsymbol{0} \\ [\boldsymbol{K}_{\boldsymbol{xp}}^e]^T & \boldsymbol{0} & \boldsymbol{0} \end{bmatrix} \begin{bmatrix} \Delta\boldsymbol{x}^e \\ \Delta\phi^e \\ \Delta p^e \end{bmatrix} = - \begin{bmatrix} \bar{\boldsymbol{R}}_{\boldsymbol{x}}^e \\ \bar{\boldsymbol{R}}_{\phi}^e \\ \boldsymbol{R}_p^e \end{bmatrix}. \tag{90}$$

where the modified matrices $\bar{\boldsymbol{K}}_{\boldsymbol{xx}}^e$, $\bar{\boldsymbol{K}}_{\boldsymbol{x}\phi}^e$, $\bar{\boldsymbol{K}}_{\phi\boldsymbol{x}}^e$, $\bar{\boldsymbol{K}}_{\phi\phi}^e$, $\bar{\boldsymbol{R}}_{\boldsymbol{x}}^e$ and $\bar{\boldsymbol{R}}_{\phi}^e$ are defined as

$$\begin{aligned} \bar{\boldsymbol{K}}_{\boldsymbol{xx}}^e &= \boldsymbol{K}_{\boldsymbol{x}\Sigma_{\boldsymbol{y}}}^e [\boldsymbol{K}_{\boldsymbol{y}\Sigma_{\boldsymbol{y}}}^e]^{-1} \boldsymbol{K}_{\boldsymbol{yy}}^e [\boldsymbol{K}_{\boldsymbol{y}\Sigma_{\boldsymbol{y}}}^e]^{-T} [\boldsymbol{K}_{\boldsymbol{x}\Sigma_{\boldsymbol{y}}}^e]^T && + \boldsymbol{K}_{\boldsymbol{xx}}^e \\ \bar{\boldsymbol{K}}_{\boldsymbol{x}\phi}^e &= \boldsymbol{K}_{\boldsymbol{x}\Sigma_{\boldsymbol{y}}}^e [\boldsymbol{K}_{\boldsymbol{y}\Sigma_{\boldsymbol{y}}}^e]^{-1} \left(\boldsymbol{K}_{\boldsymbol{yy}}^e [\boldsymbol{K}_{\boldsymbol{y}\Sigma_{\boldsymbol{y}}}^e]^{-T} \boldsymbol{K}_{\Sigma_{\boldsymbol{y}}\phi}^e - \boldsymbol{K}_{\boldsymbol{y}\phi}^e \right) \\ \bar{\boldsymbol{K}}_{\phi\boldsymbol{x}}^e &= \boldsymbol{K}_{\phi\Sigma_{\boldsymbol{y}}}^e [\boldsymbol{K}_{\boldsymbol{y}\Sigma_{\boldsymbol{y}}}^e]^{-1} \boldsymbol{K}_{\boldsymbol{yy}}^e [\boldsymbol{K}_{\boldsymbol{y}\Sigma_{\boldsymbol{y}}}^e]^{-T} [\boldsymbol{K}_{\boldsymbol{x}\Sigma_{\boldsymbol{y}}}^e]^T \\ \bar{\boldsymbol{K}}_{\phi\phi}^e &= \boldsymbol{K}_{\phi\Sigma_{\boldsymbol{y}}}^e [\boldsymbol{K}_{\boldsymbol{y}\Sigma_{\boldsymbol{y}}}^e]^{-1} \left(\boldsymbol{K}_{\boldsymbol{yy}}^e [\boldsymbol{K}_{\boldsymbol{y}\Sigma_{\boldsymbol{y}}}^e]^{-T} \boldsymbol{K}_{\Sigma_{\boldsymbol{y}}\phi}^e - \boldsymbol{K}_{\boldsymbol{y}\phi}^e \right) && + \boldsymbol{K}_{\phi\phi}^e \\ \bar{\boldsymbol{R}}_{\boldsymbol{x}}^e &= \boldsymbol{K}_{\boldsymbol{x}\Sigma_{\boldsymbol{y}}}^e [\boldsymbol{K}_{\boldsymbol{y}\Sigma_{\boldsymbol{y}}}^e]^{-1} \left(\boldsymbol{K}_{\boldsymbol{yy}}^e [\boldsymbol{K}_{\boldsymbol{y}\Sigma_{\boldsymbol{y}}}^e]^{-T} \boldsymbol{R}_{\boldsymbol{y}}^e - \boldsymbol{R}_{\Sigma_{\boldsymbol{y}}}^e \right) && + \boldsymbol{R}_{\boldsymbol{x}}^e \\ \bar{\boldsymbol{R}}_{\phi}^e &= \boldsymbol{K}_{\phi\Sigma_{\boldsymbol{y}}}^e [\boldsymbol{K}_{\boldsymbol{y}\Sigma_{\boldsymbol{y}}}^e]^{-1} \left(\boldsymbol{K}_{\boldsymbol{yy}}^e [\boldsymbol{K}_{\boldsymbol{y}\Sigma_{\boldsymbol{y}}}^e]^{-T} \boldsymbol{R}_{\boldsymbol{y}}^e - \boldsymbol{R}_{\Sigma_{\boldsymbol{y}}}^e \right) && + \boldsymbol{R}_{\phi}^e, \end{aligned} \tag{91}$$

where $n_{\boldsymbol{\mathcal{Y}}}$ denotes the total number of nodes within an element for the set $\boldsymbol{\mathcal{Y}}$.

7. Numerical examples

A series of examples are included in this section in order to verify the robustness and applicability of the mixed formulations **MFA**-T_a and **MFA**-γ presented in Sections 5.2.1 and 5.2.2, respectively. One important aspect which is common to both formulations needs to be highlighted. Specifically, the reader must notice that the strain energy in (18) does not depend on the cofactor $\boldsymbol{H}$. Therefore, in this particular case, the weak form $\mathcal{W}_{\boldsymbol{H}}$ in (62) and its associated residual vector $\boldsymbol{R}_{\boldsymbol{H}}^a$ (72) are unnecessary, and so is the field $\boldsymbol{\Sigma_H}$. Therefore, in the forthcoming numerical examples, the unknown fields for both **MFA**-T_a and **MFA**-γ formulations when considering the model in (18) will include $\{\boldsymbol{x}, \phi, p\}$, $\{\boldsymbol{F}, \boldsymbol{H}, J, \boldsymbol{A}\}$ and $\{\boldsymbol{\Sigma_F}, \Sigma_J, \boldsymbol{\Sigma_A}\}$. On the contrary, for those examples where the strain energy depends on the cofactor (see Section 7.3.3), the field $\boldsymbol{\Sigma_H}$ is included as part of the set of unknowns.

7.1. Numerical example 1: patch test

The objective of this example is:

- **O1.I** Assesment of the correctness of the computational implementation of the mixed formulations **MFA**-T_a and **MFA**-γ introduced in Sections 5.2.1 and 5.2.2 when using both Finite Elements ELEM1 and ELEM2 in Table 4.

In this example, we consider a portion of the myocardium defined by a cubic shaped domain of unit length. This domain is discretised using two $(3 \times 3 \times 3) \times 6$ tetrahedral discretisations characterised by: (**a**) structured mesh (refer to Figure 5(a)) and (**b**) unstructured mesh (refer to Figure 5(b)) where an arbitrary displacement of the interior nodes of the structured mesh is applied.

(a)   (b)
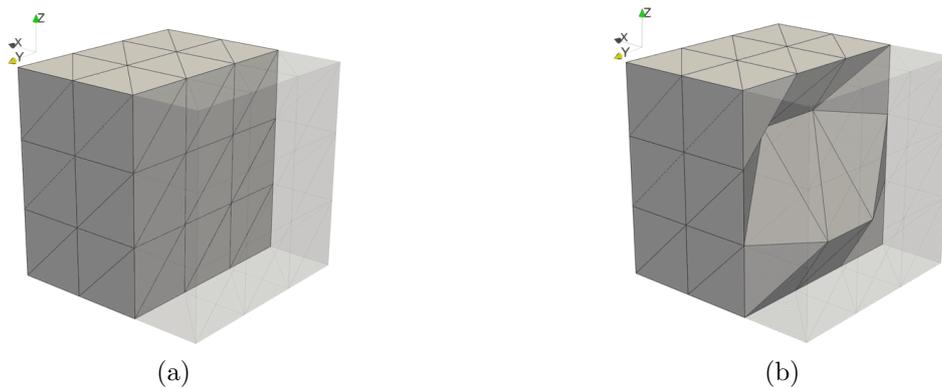
Figure 5: Numerical example 1. $(3 \times 3 \times 3) \times 6$ tetrahedral discretisation with (**a**) structured and (**b**) unstructured mesh.

The constitutive model describing the passive response of the myocardium in this example is that in (18), and all the material parameters chosen can be found in Figure 6. In this example, the fibres $\{\boldsymbol{n}_0, \boldsymbol{s}_0, \boldsymbol{f}_0\}$ are chosen parallel to the axes $\{OX, OY, OZ\}$, respectively.

Parameters for the Holzapfel-Odgen constitutive law			
a = 0.059 kPa	a_f = 0 kPa	a_s = 0 kPa	a_{fs} = 0 kPa
b = 8.023	b_f = 0	b_s = 0	b_{fs} = 0

Figure 6: Numerical example 1. Material parameters chosen for the constitutive model in equation [24].

With regards to boundary conditions for the transmembrane potential ϕ, this is prescribed as $\phi = 0$ mV and $\phi = 30$ mV on the faces perpendicular to the OZ axis whilst homogeneous Neumann boundary conditions are applied elsewhere. Furthermore, homogeneous normal Dirichlet boundary conditions for the displacements are applied on the base perpendicular to the OZ axis whilst homogeneous Neumann boundary conditions are applied elsewhere.

In order to focus strictly on above objective **O1.I**, the physics of the problem has been simplified. Specifically, the time derivative of the electric potential, i.e. $\dot{\phi}$ and the source term f_ϕ in (4) have been neglected. Furthermore, *ad-hoc* activation laws for both active stress and active strain approaches have been defined as

$$T_a = \alpha\phi; \qquad \gamma_{\boldsymbol{f}_0} = \beta\phi; \qquad \gamma_{\boldsymbol{s}_0} = 0; \qquad \gamma_{\boldsymbol{n}_0} = 0, \tag{92}$$

with $\alpha = -0.5$ and $\beta = 0.05$.

As it can be seen from Figures 7, a linear distribution for both the deformation gradient tensor $\boldsymbol{F}$ and the transmembrane potential ϕ are obtained along the OZ axis, as expected. This distribution is identical for both structured and unstructured meshes and for both formulations **MFA**-T_a, **MFA**-γ, when using the Finite Elements ELEM1 and ELEM2 in Table 4. Therefore, both Finite Elements pass the patch test in both mixed formulations. For completeness, the quadratic convergence of the Newton-Raphson algorithm is shown in Figure 8.
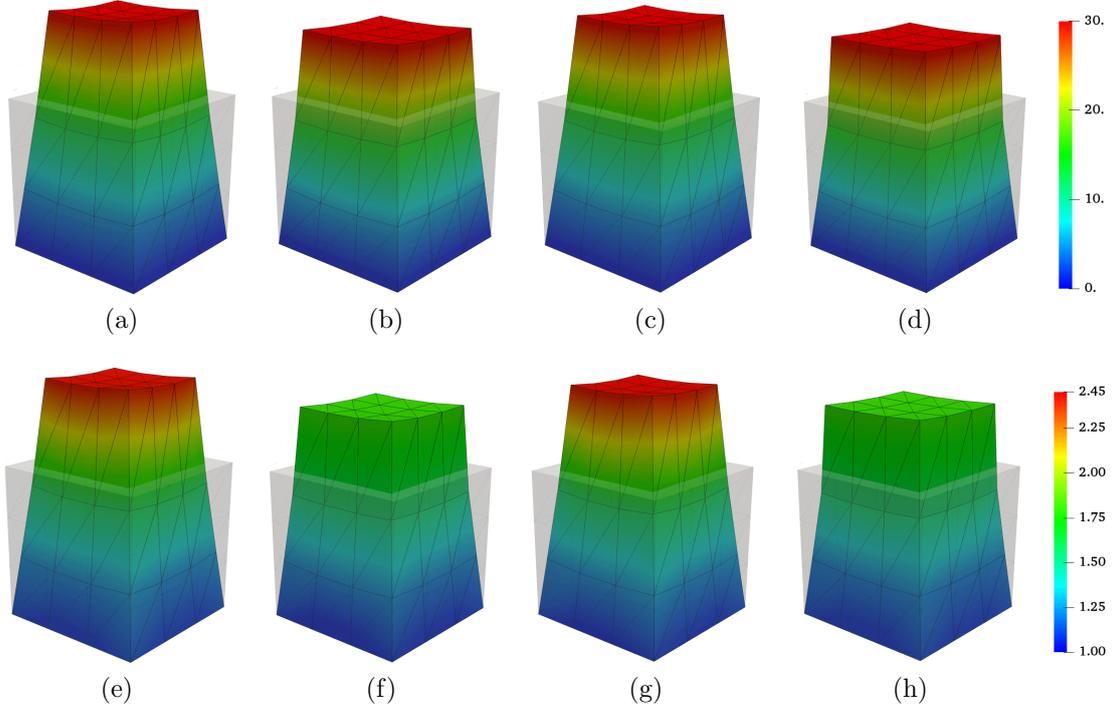
Figure 7: Numerical example 1. Contour plot of ϕ on unstructured mesh for: **(a)** ELEM1-**MFA**-T_a; **(b)** ELEM1-**MFA**-γ; **(c)** ELEM2-**MFA**-T_a; **(d)** ELEM2-**MFA**-γ. Contour plot of F_{zZ} on unstructured mesh for: **(e)** ELEM1-**MFA**-T_a; **(f)** ELEM1-**MFA**-γ; **(g)** ELEM2-**MFA**-T_a; **(h)** ELEM2-**MFA**-γ.
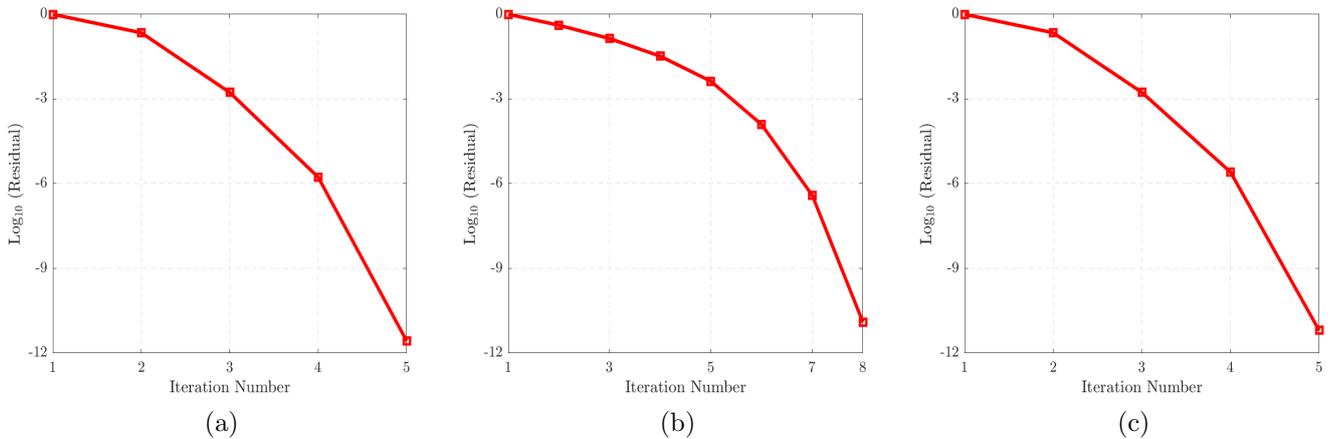
Figure 8: Numerical example 1. Quadratic convergence of the Newton-Raphson algorithm for: **(a)** ELEM1-**MFA**-γ; **(b)** ELEM2-**MFA**-γ; **(c)** **MFA**-T_a. All the results correspond to the unstructured mesh in Figure 5_b.

7.2. Numerical example 2: convergence of new mixed formulations

The objective of this example is:

- **O2.I** Demonstrate the *p*-order of accuracy of the mixed formulations **MFA**-γ presented in Section 5.2.2 when using both Finite Elements ELEM1 and ELEM2.

The same cubic domain of unit length as in the previous example is considered. The constitutive model describing the passive response in this example is that in equation (18), with material parameters chosen as in Figure 6. Furthermore, the directions of the fibres $\{\boldsymbol{f}_0, \boldsymbol{s}_0, \boldsymbol{n}_0\}$ are chosen parallel to the axes $\{OX, OY, OZ\}$, respectively.

In order to study objective **O2.I**, the analysis of an *ad hoc* manufactured problem is carried out following a similar procedure as that described in reference [60]. For that, the following exact fields associated with the deformed configuration $\boldsymbol{x}$ and the transmembrane potential ϕ are chosen

$$\boldsymbol{x}^{\text{exact}} = \boldsymbol{X} + \begin{bmatrix} AX_1^3 \\ BX_2^3 \\ CX_3^3 \end{bmatrix}; \qquad \phi^{\text{exact}} = DX_1^4, \tag{93}$$

with $\{A, B, C, D\} = \{0.01, 0.01, 0.01, 100\}$. The exact deformation gradient tensor $\boldsymbol{F}^{\text{exact}}$ associated with $\boldsymbol{x}^{\text{exact}}$ and the material gradient of ϕ^{exact} can be computed as

$$\boldsymbol{F}^{\text{exact}} = \begin{bmatrix} 1 + 3AX_1^2 & 0 & 0 \\ 0 & 1 + 3BX_2^2 & 0 \\ 0 & 0 & 1 + 3CX_3^2 \end{bmatrix}; \qquad \boldsymbol{A}^{\text{exact}} = \begin{bmatrix} 4DX_1^3 \\ 0 \\ 0 \end{bmatrix}, \tag{94}$$

This enables to obtain the exact fields $\{\boldsymbol{H}^{\text{exact}}, J^{\text{exact}}, \boldsymbol{D}^{\text{exact}}\}$ using equations (1) and (44) as

$$\boldsymbol{H}^{\text{exact}} = \frac{1}{2}\boldsymbol{F}^{\text{exact}} \boldsymbol{\times} \boldsymbol{F}^{\text{exact}}; \qquad J^{\text{exact}} = \frac{1}{3}\boldsymbol{H}^{\text{exact}} : \boldsymbol{F}^{\text{exact}}; \qquad \boldsymbol{D}^{\text{exact}} = d_{\text{iso}} \frac{\left(\boldsymbol{H}^{\text{exact}}\right)^T \boldsymbol{H}^{\text{exact}}}{\left(J^{\text{exact}}\right)^2}. \tag{95}$$

The following *ad-hoc* activation law for the active strain approach is considered

$$\gamma_{\boldsymbol{f}_0}^{\text{exact}} = \frac{\beta \left(\phi^{\text{exact}}\right)^2}{\left(\phi^{\text{exact}}\right)^2 + 1}; \qquad \gamma_{\boldsymbol{s}_0}^{\text{exact}} = \gamma_{\boldsymbol{n}_0}^{\text{exact}} = \frac{1}{\sqrt{\gamma_{\boldsymbol{f}_0}^{\text{exact}} - 1}}, \tag{96}$$

with $\beta = -0.1$. This enables us to compute the active component of the deformation tensor $\boldsymbol{F}^{A,\text{exact}}$ from (29) and its elastic counterpart $\boldsymbol{F}^{E,\text{exact}}$ from (28). With this, the first exact first Piola-Kichhoff stress tensor $\boldsymbol{P}^{\text{exact}}$ can be obtained as in (36). In addition, using $d_{\text{iso}} = 10^{-4}$ and $d_{\text{ani}} = 0$ it is possible to compute $\boldsymbol{Q}^{\text{exact}}$ from (43)-(44). The computation of both $\{\boldsymbol{P}^{\text{exact}}, \boldsymbol{Q}^{\text{exact}}\}$, allows to obtain the associated volumetric force $\boldsymbol{b}_0$ in (3) and the source term f_ϕ in (4) as

$$\boldsymbol{b}_0 = \text{DIV}\boldsymbol{P}^{\text{exact}}; \qquad f_\phi = -\text{DIV}\boldsymbol{Q}^{\text{exact}}, \tag{97}$$

where the time dependent term $\dot{\phi}$ (refer to (4)) vanishes from the definition of ϕ^{exact} in (93). Dirichlet boundary conditions compatible with the exact fields $\{\boldsymbol{x}^{\text{exact}}, \phi^{\text{exact}}\}$ in (93) are applied on the boundary of the domain. Finally, as it can be seen from the definition of $\boldsymbol{F}^{\text{exact}}$ in (94), the exact displacement field is not incompressible. Therefore, the pressure field p will not be included as an unknown field for this specific example.

It can be seen from Figure 9 that the convergence of the fields $\{\boldsymbol{x}, \boldsymbol{F}, \boldsymbol{H}, \boldsymbol{\Sigma_F}, \boldsymbol{\Sigma_H}\}$ is decreased by 1 due to the constant interpolation of the fields $\{J, \Sigma_J\}$. This has already been shown in Reference [60]. The remaining fields converge at the expected rate. On the contrary, for the Finite Element ELEM2, all the fields converge at the expected rate. Nonetheless, it has been shown (in the context of nonlinear elasticity, where no electrical coupling is present) [60, 77] that the equivalent to ELEM1 outperforms the classical P_2 (tetrahedral) element in bending dominated problems. Moreover, ELEM1 is computationally more effective than ELEM2 as the inclusion of bubble functions in the latter requires an increased order of quadrature with respect to ELEM1. Therefore, ELEM1 will be used for the remaining examples of this paper.
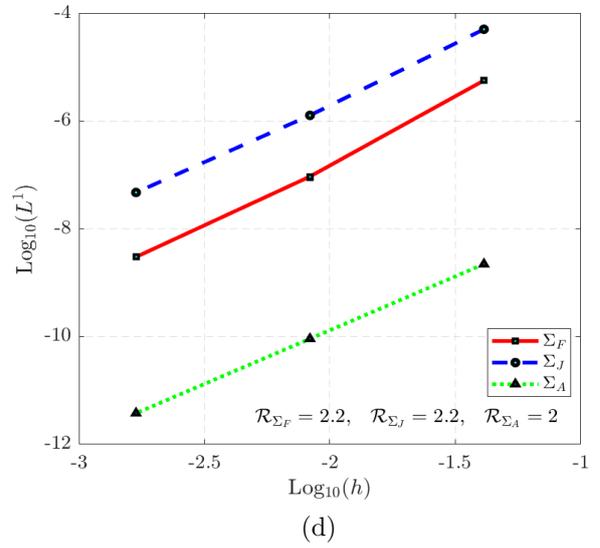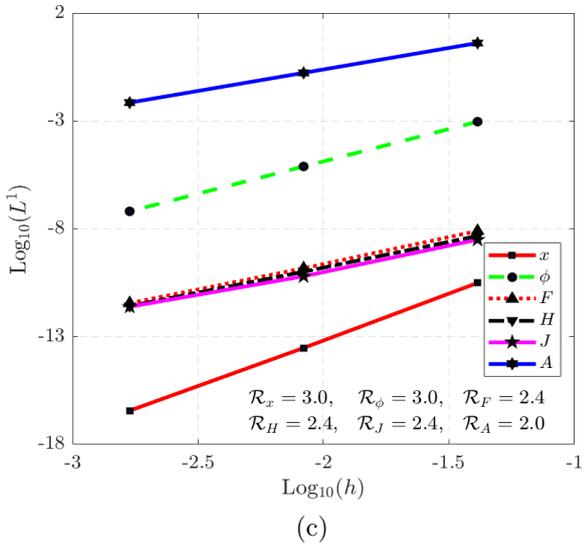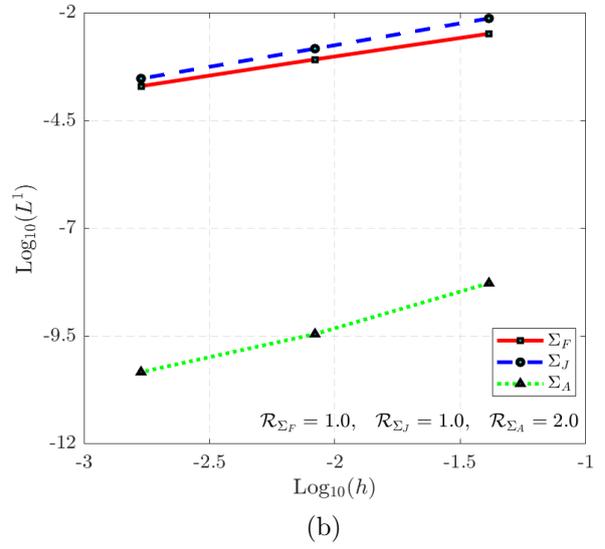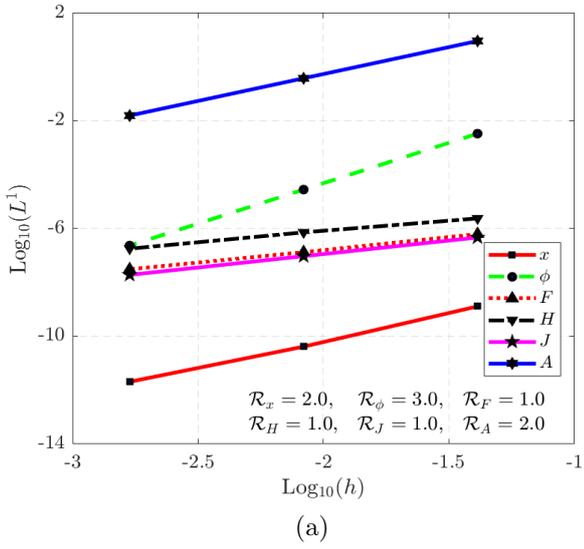
Figure 9: Numerical example 2. p-order of accuracy for: $\{\boldsymbol{x}, \phi, \boldsymbol{F}, \boldsymbol{H}, J, \boldsymbol{A}\}$ for: **(a)** ELEM1-**MFA**-γ and **(b)** ELEM2-**MFA**-γ. p-order of accuracy for: $\{\boldsymbol{\Sigma_F}, \Sigma_J, \boldsymbol{\Sigma_A}\}$ for: **(c)** ELEM1-**MFA**-γ and **(d)** ELEM2-**MFA**-γ.

7.3. Numerical example 3: benchmark problems

The objective of this example is:

- **O3.I** Compare the accuracy of the new formulations presented in Sections 5.2.1 and 5.2.2 against available computer codes in the context of cardiac mechanics in a series of tailor-made benchmark examples reported in [78].

With the aim of aiding in the verification of current and future cardiac mechanics solvers, the authors in [78] proposed three benchmark problems for cardiac mechanics. In these, the constitutive model chosen for the passive response of the myocardium was that proposed by Guccione [22], defined as

$$\Psi\left(\boldsymbol{E}^{\star}\right) = \frac{K}{2}\left(e^{Q(\boldsymbol{E}^{\star})} - 1\right), \tag{98}$$

The exponent $Q\left(\boldsymbol{E}^{\star}\right)$ in (98) is defined in terms of the local Green-Lagrange strain tensor[7] as

$$Q\left(\boldsymbol{E}^{\star}\right) = c_f E^{\star 2}_{11} + c_t\left(E^{\star 2}_{22} + E^{\star 2}_{33} + E^{\star 2}_{23} + E^{\star 2}_{32}\right) + c_{fs}\left(E^{\star 2}_{12} + E^{\star 2}_{21} + E^{\star 2}_{13} + E^{\star 2}_{31}\right), \tag{99}$$

where $\{K, c_f, c_t, c_{fs}\}$ represent material parameters. Alternatively, we have derived in Appendix B an invariant representation of $\boldsymbol{Q}\left(\boldsymbol{E}^{\star}\right)$ and an additional representation in terms of the (global) strain measures $\{\boldsymbol{F_x}, \boldsymbol{H_x}, J_x\}$ as

$$Q\left(\boldsymbol{E}^{\star}\right) = \widetilde{Q}\left(\boldsymbol{F_x}, \boldsymbol{H_x}, J_x\right) = A\,\widetilde{Q}_{\text{aniso},1}\left(\boldsymbol{F_x}\right) + B\,\widetilde{Q}_{\text{aniso},2}\left(\boldsymbol{F_x}, \boldsymbol{H_x}\right) + C\,\widetilde{Q}_{\text{iso}}\left(\boldsymbol{F_x}, \boldsymbol{H_x}, J_x\right), \tag{100}$$

with $\{A, B, C\}$ and $\{\widetilde{Q}_{\text{aniso},1}, \widetilde{Q}_{\text{aniso},2}, \widetilde{Q}_{\text{iso}}\}$ presented in Appendix B. Notice that above representation in (100) is more amenable for Finite Element implementation as it does not depend on the local axis of choice. Specifically, this representation permits the use of both mixed formulations presented in this paper, namely **MFA**-T_a and **MFA**-γ in Sections 5.2.1 and 5.2.2 in conjunction with Guccione's model, as these formulations are tailor-made for constitutive models expressed in terms of the strain measures $\{\boldsymbol{F_x}, \boldsymbol{H_x}, J_x\}$.

7.3.1. Numerical example 3.1: cantilever beam

The first benchmark problem considers the beam with geometry and boundary conditions in Figure 10. The beam is subjected to a follower load of $q = 4\,\text{Pa}$. The material parameters of Guccione's model in (98) are defined by $\{K, c_f, c_t, c_{fs}\} = \{2\,\text{kPa}, 8, 2, 4\}$ where the local axis $\{\boldsymbol{f}_0, \boldsymbol{s}_0, \boldsymbol{n}_0\}$ are chosen to be coincident with the global axis.
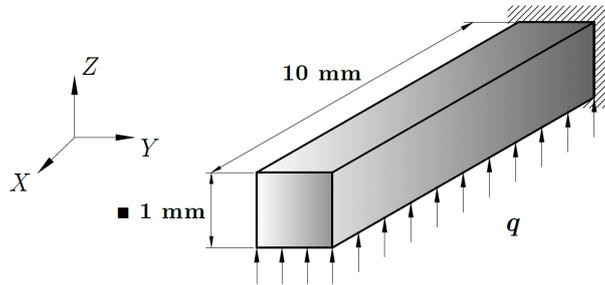
Figure 10: Numerical example 3.1. Geometry and boundary conditions.

The four meshes in Figure 11 will be used. Each mesh will be solved using the mixed formulation **MFA**-T_a in Section 4.1.2 in conjunction with the Finite Element ELEM1 in Table 4. Notice

---

[7]Let $\boldsymbol{R}$ be the rotation matrix from a local system of coordinates parallel to $\{\boldsymbol{f}_0, \boldsymbol{s}_0, \boldsymbol{n}_0\}$ to the global system of coordinates. $\boldsymbol{E}^{\star}$ can be related to its global counterpart $\boldsymbol{E} = \frac{1}{2}\left(\boldsymbol{F}_x^T \boldsymbol{F_x} - \boldsymbol{I}\right)$ as $\boldsymbol{E}^{\star} = \boldsymbol{R}^T \boldsymbol{E} \boldsymbol{R}$.

that in this problem, electro-activation effects are neglected. Therefore, **MFA**-T_a and **MFA**-γ in Section 4.1.3 are identical in this specific scenario.

The results obtained with the ELEM1-**MFA**-T_a formulation will be studied for two variables of interest: **(a)** the maximum Z-displacement for the four meshes in Figure 11 will be compared against the results from authors in [78]; **(b)** the engineering strain measure along the three Cartesian directions for the finest mesh in Figure 11 will be compared with other approaches. The engineering strain measures with respect to the axis $\{OX, OY, OZ\}$ are defined at the material points $\{\bar{\boldsymbol{X}}_{X_i}, \bar{\boldsymbol{X}}_{Y_i}, \bar{\boldsymbol{X}}_{Z_i}\}$ as

$$\varepsilon_X\left(\bar{\boldsymbol{X}}_{X_i}\right) = \frac{\|\hat{\boldsymbol{x}}_i - \bar{\boldsymbol{x}}_{X_i}\|}{\left\|\hat{\boldsymbol{X}}_i - \bar{\boldsymbol{X}}_{X_i}\right\|} - 1; \quad \varepsilon_Y\left(\bar{\boldsymbol{X}}_{Y_i}\right) = \frac{\|\hat{\boldsymbol{x}}_i - \bar{\boldsymbol{x}}_{Y_i}\|}{\left\|\hat{\boldsymbol{X}}_i - \bar{\boldsymbol{X}}_{Y_i}\right\|} - 1; \quad \varepsilon_Z\left(\bar{\boldsymbol{X}}_{Z_i}\right) = \frac{\|\hat{\boldsymbol{x}}_i - \bar{\boldsymbol{x}}_{Z_i}\|}{\left\|\hat{\boldsymbol{X}}_i - \bar{\boldsymbol{X}}_{Z_i}\right\|} - 1,$$
(101)

where the points $\{\hat{\boldsymbol{X}}_i, \bar{\boldsymbol{X}}_{X_i}, \bar{\boldsymbol{X}}_{Y_i}, \bar{\boldsymbol{X}}_{Z_i}\}$ in the reference configuration are defined as

$$\begin{aligned}
\hat{\boldsymbol{X}}_i &= (i, 0.5, 0.5); & \bar{\boldsymbol{X}}_{X_i} &= (i+1, 0.5, 0.5); & i &= \{0, 1, ...9\}; \\
\bar{\boldsymbol{X}}_{Y_i} &= (i, 0.9, 0.5); & \bar{\boldsymbol{X}}_{Z_i} &= (i, 0.5, 0.9); & i &= \{0, 1, ...9\},
\end{aligned}$$
(102)

and with $\{\hat{\boldsymbol{x}}_i, \bar{\boldsymbol{x}}_{X_i}, \bar{\boldsymbol{x}}_{Y_i}, \bar{\boldsymbol{x}}_{Z_i}\}$ their respective counterparts in the deformed configuration.
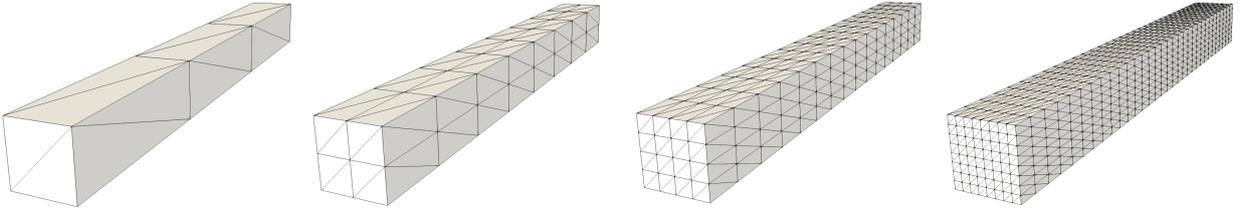
Figure 11: Numerical example 3.1. Increasingly finer Finite Element discretisations for cantilever beam example. From left to right: $(1 \times 1 \times 3) \times 6$, $(2 \times 2 \times 8) \times 6$, $(4 \times 4 \times 16) \times 6$ and $(8 \times 8 \times 32) \times 6$ tetrahedral elements.

It can be seen from Figure 12 that the maximum Z-coordinate obtained for the four discretisations is very similar. In fact, for the coarsest mesh, the results are considerably better than those obtained by the code Simula-FEniCS. In addition, Figure 13 shows a good agreement of the results obtained by the ELEM1-**MFA**-γ formulation with respect to those reported in [78] for the finest mesh in Figure 11.

For the sake of completeness, the contour plot for the first Piola Kirchhoff stress tensor P_{zX} and the Lagrange multiplier p enforcing the incompressibility constraint is shown in Figure 14. A reasonable agreement for these variables is obtained for the four discretisations considered in this paper.

7.3.2. Numerical example 3.2: inflation of a ventricle

The second benchmark problem considers the idealised ventricle represented by an intersected set of ellipsoids with semiaxes $\{10, 10, 20\}$ mm and $\{7, 7, 17\}$ mm centred in the origin and truncated by the plane $Z = 5$ mm (see Figure 15_a). The material parameters of Guccione's model (98) are $\{K, c_f, c_s, c_{fs}\} = \{10 \, \text{kPa}, 1, 1, 1\}$. Homogeneous Dirichlet boundary conditions are applied on the plane $Z = 5$ mm for all directions and a pressure (follower load) of $10 \, \text{kPa}$ is applied on the inner face (endocardium), leading to the inflation of the ventricle (see Figure 15_c).

The engineering strain is defined now with respect to the ellipsoidal coordinates $\{\varphi, \theta, R\}$ of the ventricle (refer to Figure 15). The engineering strains with respect to the axis $\{O\varphi, O\theta, OR\}$
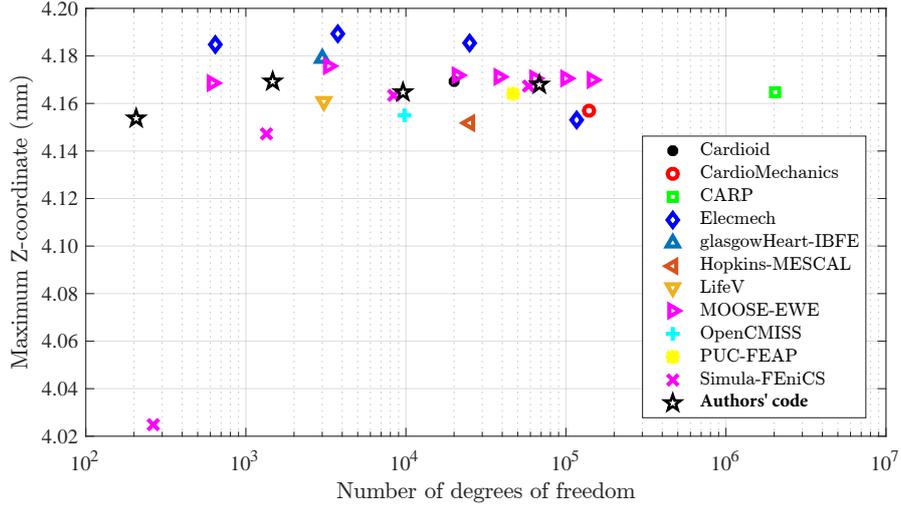
Figure 12: Numerical example 3.1. Maximum Z-coordinate in the deformed configuration for the four discretisations in Figure 11. Results obtained with ELEM1-**MFA**-T_a formulation and by authors in Reference [78].
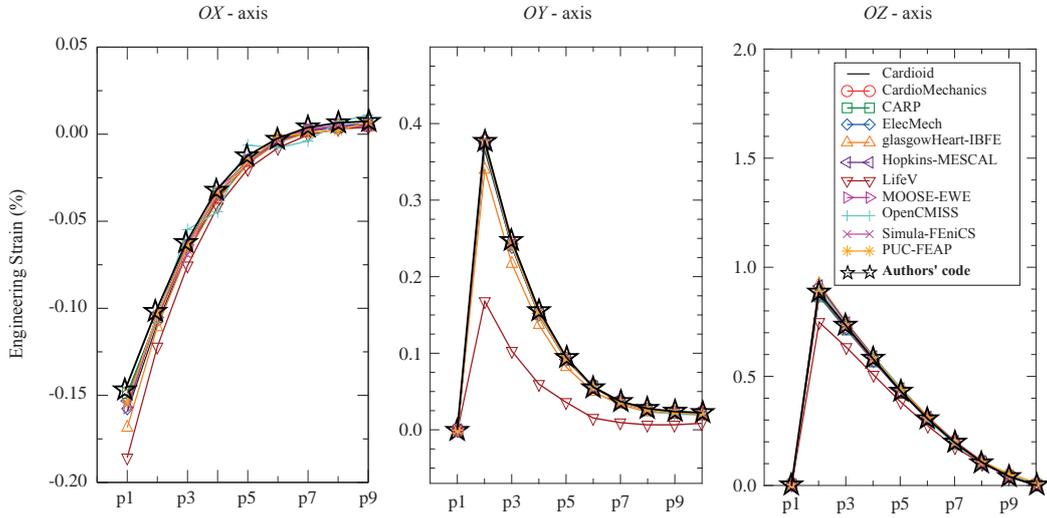
Figure 13: Numerical example 3.1. Engineering strain ε_X (left), ε_Y (centre) and ε_Z (right) for finest mesh in Figure 11. $\{p_1, ..., p_9\}$ correspond to: $\{\bar{\boldsymbol{X}}_{X_1}, ..., \bar{\boldsymbol{X}}_{X_9}\}$ in left figure (refer to (102)); $\{\bar{\boldsymbol{X}}_{Y_1}, ..., \bar{\boldsymbol{Y}}_{X_9}\}$ in centre figure; $\{\bar{\boldsymbol{X}}_{Z_1}, ..., \bar{\boldsymbol{X}}_{Z_9}\}$ in right figure. Results obtained with ELEM1-**MFA**-T_a formulation and by authors in [78].
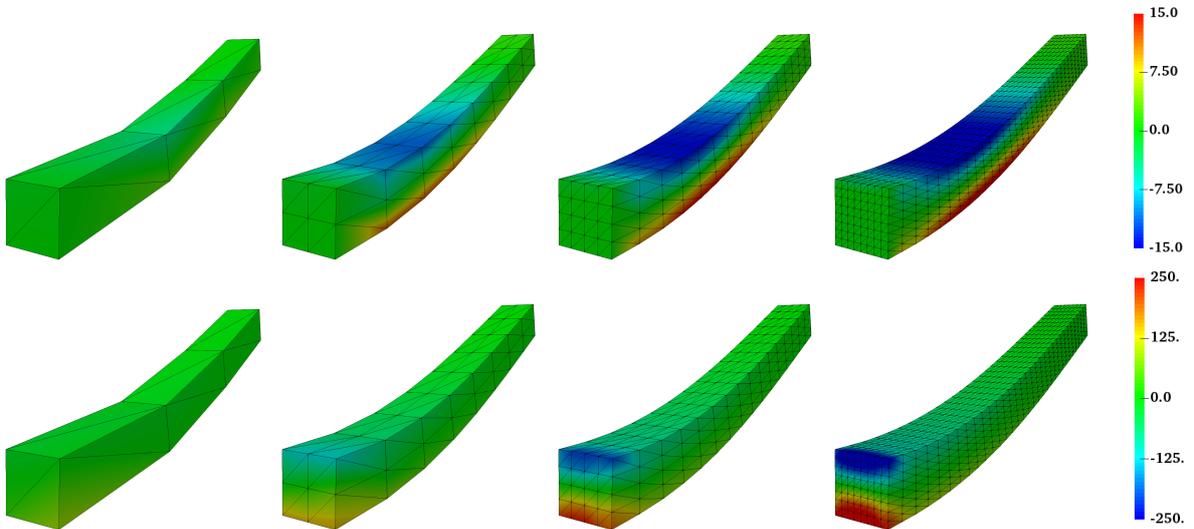
Figure 14: Numerical example 3.1. Contour plot distribution of P_{zX} and the Lagrange multiplier for incompressibility p for the four discretisations considered and for the ELEM1-**MFA**-T_a formulation.

26
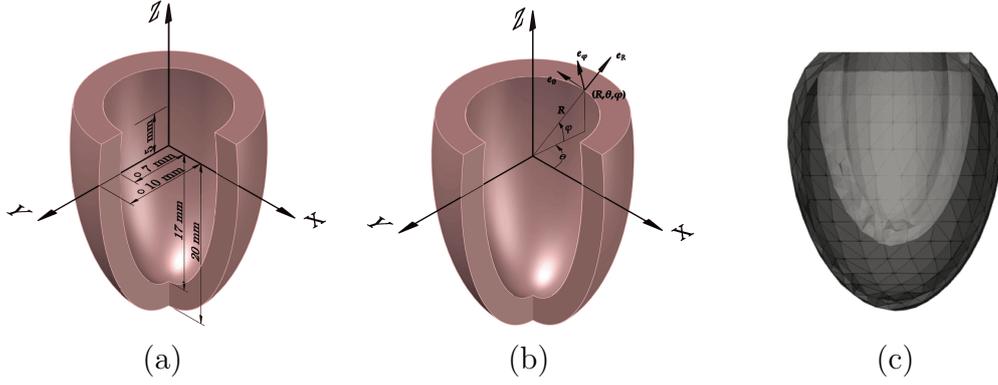
Figure 15: Numerical example 3.2. **(a)** Geometry of the idealised ventricle. **(b)** Ellipsoidal coordinates of the idealised ventricle. **(c)** Initial configuration (grey) and final configuration (black) after inflation of the ventricle.

at material points $\{\bar{\boldsymbol{X}}_{\varphi_i}, \bar{\boldsymbol{X}}_{\theta_i}, \bar{\boldsymbol{X}}_{R_i}\}$ are defined in a similar fashion to equation (101) as

$$\varepsilon_\varphi\left(\bar{\boldsymbol{X}}_{\varphi_i}\right) = \frac{\|\hat{\boldsymbol{x}}_i - \bar{\boldsymbol{x}}_{\varphi_i}\|}{\left\|\hat{\boldsymbol{X}}_i - \bar{\boldsymbol{X}}_{\varphi_i}\right\|} - 1; \quad \varepsilon_\theta\left(\bar{\boldsymbol{X}}_{\theta_i}\right) = \frac{\|\hat{\boldsymbol{x}}_i - \bar{\boldsymbol{x}}_{\theta_i}\|}{\left\|\hat{\boldsymbol{X}}_i - \bar{\boldsymbol{X}}_{\theta_i}\right\|} - 1; \quad \varepsilon_R\left(\bar{\boldsymbol{X}}_{R_i}\right) = \frac{\|\hat{\boldsymbol{x}}_i - \bar{\boldsymbol{x}}_{R_i}\|}{\left\|\hat{\boldsymbol{X}}_i - \bar{\boldsymbol{X}}_{R_i}\right\|} - 1,$$

(103)

where the points $\{\hat{\boldsymbol{X}}_i, \bar{\boldsymbol{X}}_{\varphi_i}, \bar{\boldsymbol{X}}_{\theta_i}, \bar{\boldsymbol{X}}_{R_i}\}$ can be found in Reference [78]. Table 1 shows a good agreement of the results obtained by the ELEM1-**MFA**-T_a formulation with respect to those reported in [78] for the three engineering strains $\{\varepsilon_\varphi, \varepsilon_\theta, \varepsilon_R\}$ for all the points described in Reference [78] located at the endocardium, midmyocardium and epicardium. Finally, Figure 16 displays the contour plot of $\{F_{xY}, H_{zY}, P_{zX}, p, \Sigma_{F_{zY}}, \Sigma_J\}$ by means of the ELEM1-**MFA**-T_a formulation.
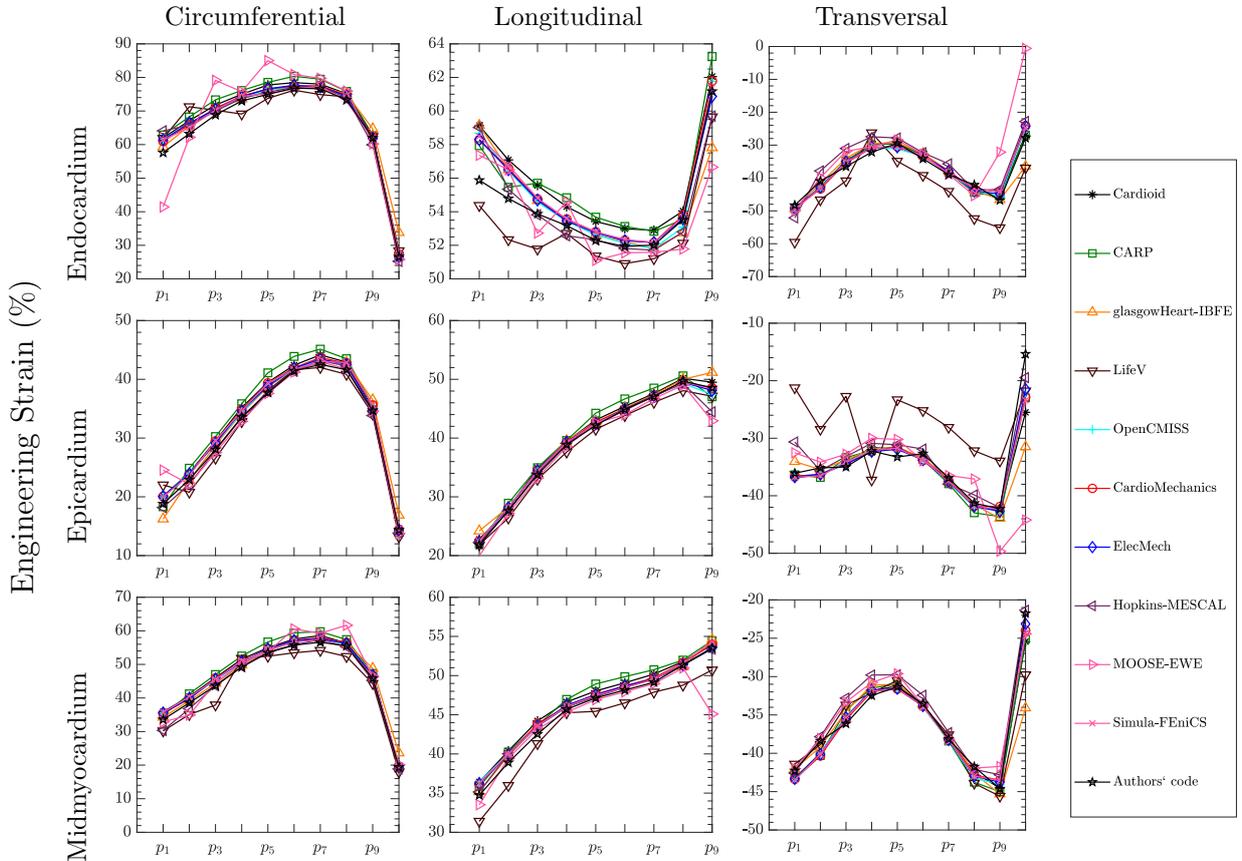
Table 1: Numerical example 3.2. Engineering strain ε_θ (left), ε_ϕ (centre) and ε_R (right). $\{p_1, ..., p_9\}$ corresponds to: $\{\bar{\boldsymbol{X}}_{\theta_1}, ..., \bar{\boldsymbol{X}}_{\theta_9}\}$ in left figure (refer to [78]); $\{\bar{\boldsymbol{X}}_{\varphi_1}, ..., \bar{\boldsymbol{Y}}_{\varphi_9}\}$ in centre figure; $\{\bar{\boldsymbol{X}}_{R_1}, ..., \bar{\boldsymbol{X}}_{R_9}\}$ in right figure. Results obtained with ELEM1-**MFA**-T_a formulation and by authors in [78].

27
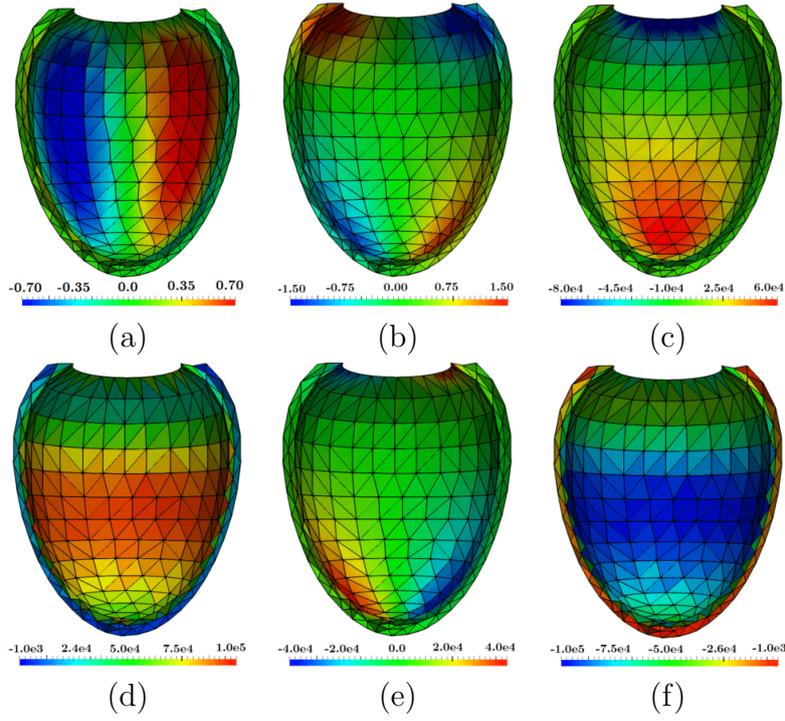
Figure 16: Numerical example 3.2. Contour plot distribution of: **(a)** F_{xY}, **(b)** H_{zY}, **(c)** P_{zX}, **(d)** p, **(e)** $\Sigma_{F_{zY}}$ and **(f)** Σ_J. Results obtained with ELEM1-**MFA**-T_a formulation.

7.3.3. Numerical example 3.3: inflation and active contraction of a ventricle

The geometry of the third example can be seen in Figure 17_a. The Dirichlet boundary conditions are identical to those in Section 7.3.2. In this case, there is a combined effect of a follower load of value 15 kPa and a contraction along a set of fibres $\boldsymbol{f}_0$ whose parametrisation can be found in [78]. This contraction is imposed by considering a value of 60 kPa for the cardiomyocite stress T_a in the active stress approach. The proposed mathematical description of the fibres $\boldsymbol{f}_0$ is singular in the apex of the ventricle, leading to stress concentration in this region.
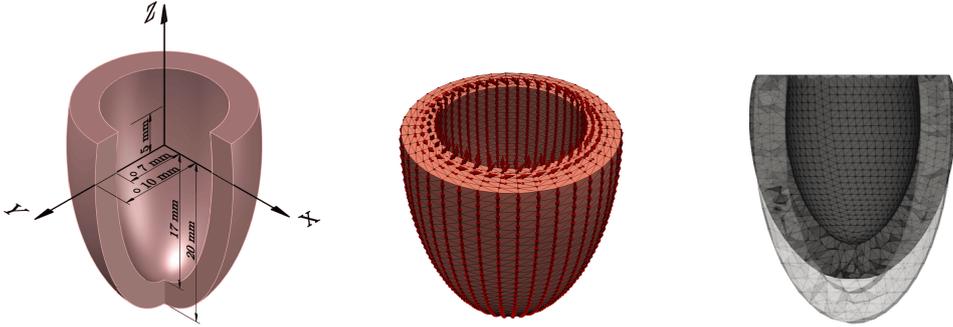
Figure 17: Numerical example 3.3. **(a)** Geometry of the idealised ventricle. **(b)** Orientation of $\boldsymbol{f}_0$ in Guccione's model (B.1). **(c)** Undeformed (transparent) and deformed (grey) configurations after activation of the ventricle.

The material parameters of Guccione's constitutive law (98) are chosen as $\{K, c_f, c_s, c_{fs}\} = \{10\,\text{kPa}, 8, 2, 4\}$. Table 2 shows a good agreement of the results obtained by the ELEM1-**MFA**-T_a formulation with respect to those reported in [78] for the three engineering strains $\{\varepsilon_\varphi, \varepsilon_\theta, \varepsilon_R\}$ for all the points described in Reference [78] located at the endocardium, midmyocardium and epicardium. Finally, Figure 18 displays the contour plot of $\{F_{zY}, H_{zY}, P_{zX}, p, \Sigma_{F_{zY}}, \Sigma_J\}$ by means of the ELEM1-**MFA**-T_a formulation.
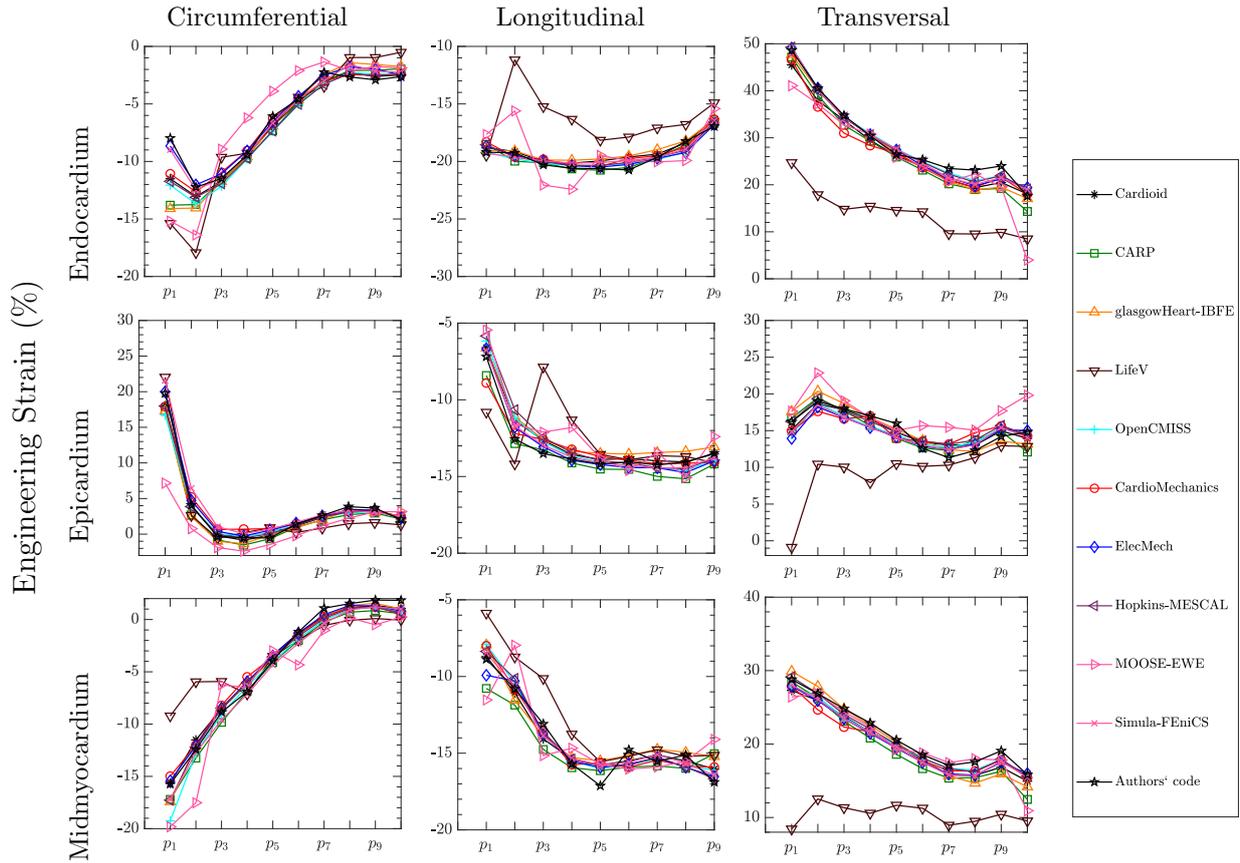
Table 2: Numerical example 3.3. Engineering strain ε_θ (left), ε_ϕ (centre) and ε_R (right). $\{p_1, ..., p_9\}$ corresponds to: $\{\bar{X}_{\theta_1}, ..., \bar{X}_{\theta_9}\}$ in left figure (refer to [78]); $\{\bar{X}_{\varphi_1}, ..., \bar{Y}_{\varphi_9}\}$ in centre figure; $\{\bar{X}_{R_1}, ..., \bar{X}_{R_9}\}$ in right figure. Results obtained with ELEM1-**MFA**-T_a formulation and by authors in [78].
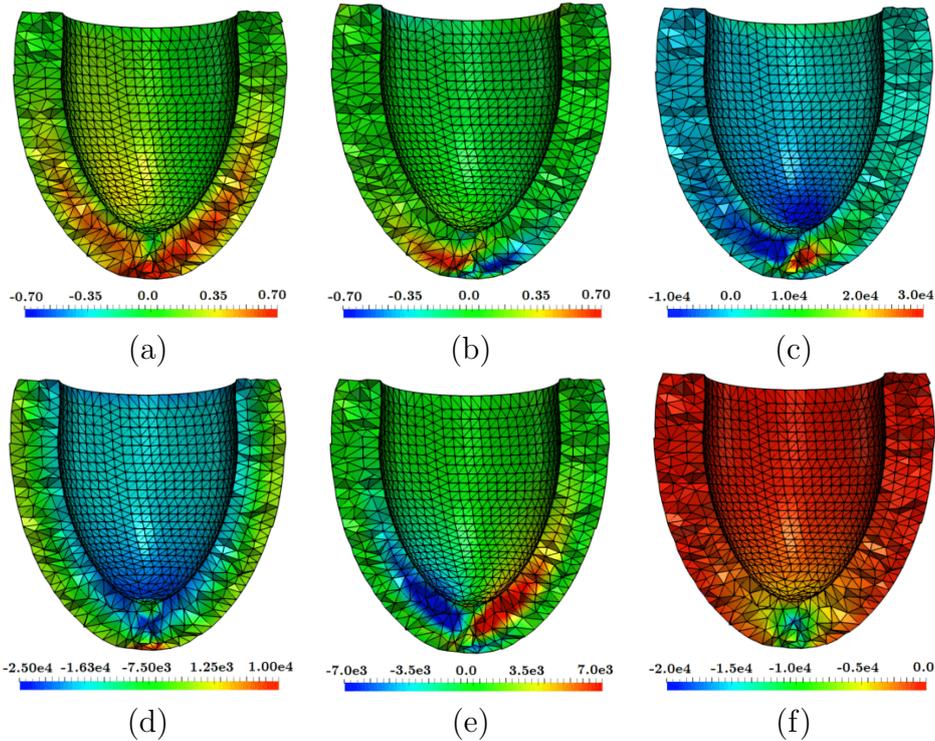
Figure 18: Numerical example 3.3. Contour plot distribution of: **(a)** F_{xY}, **(b)** H_{zY}, **(c)** P_{zX}, **(d)** p, **(e)** $\Sigma_{F_{zY}}$ and **(f)** Σ_J. Results obtained with the ELEM1-**MFA**-T_a formulation.

7.4. Numerical example 4: coupled electro-mechanical simulation of a pair of idealised ventricles

The objectives of this example are:

- **O4.I** Demonstrate the applicability of formulations **MFA**-T_a in Section 5.2.1 and **MFA**-γ in Section 5.2.2 for the simulation of the cardiac cycle under different: **(a)** coupling type approaches (active stress/active strain); **(b)** activation laws (see Section 4.3) and **(c)** ionic models (see Section 4.2).

- **O4.II** Demonstrate the shortcomings of conventional Finite Element approaches for the modelling of cardiac mechanics.

- **O4.III** Study the susceptibility for loss of ellipticity of the constitutive model proposed by Holzapfel-Ogden in [24] (refer to (18)) for both active strain and active stress approaches during the cardiac cycle.

The main features of this example are:

Geometry: we consider in this example an idealised geometry of two ventricles defined by four ellipsoids. The two outermost ellipsoids are centred in the origin, i.e $\{X, Y, Z\} = \{0, 0, 0\}$ and the length of their semi-axes is $\{50, 50, 70\}$ mm and $\{45, 45, 65\}$ mm. The two innermost ellipsoids are centred at $\{X, Y, Z\} = \{0, -10, 0\}$ and the length of their semi-axes is $\{40, 40, 63\}$ mm and $\{35, 35, 60\}$ mm. The four ellipsoids are truncated by the plane $Z = 0$.
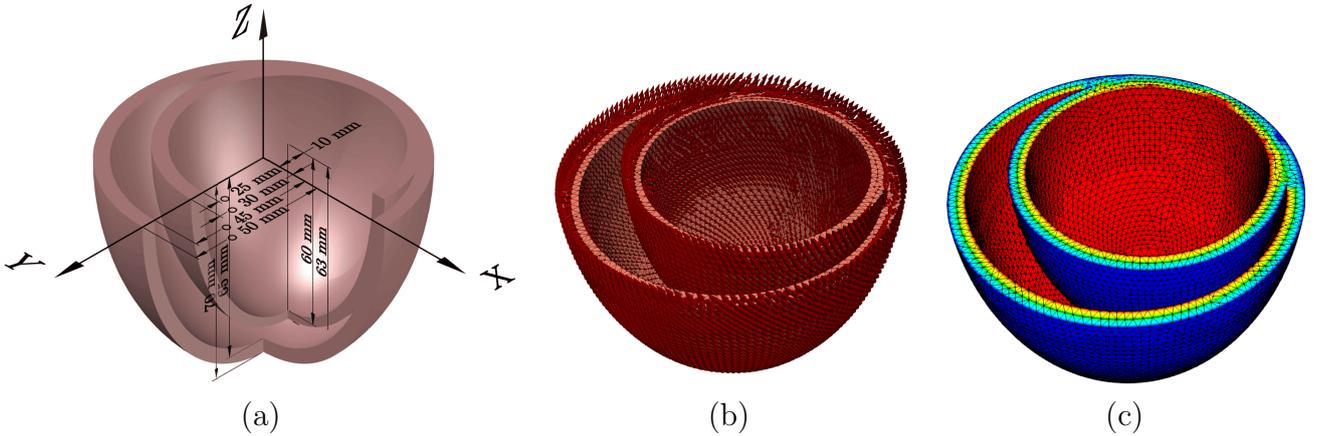
Figure 19: Numerical example 4. **(a)** Geometry of the two ventricles. **(b)** Representation of the fibre $\boldsymbol{f}_0$. **(c)** Contour plot of η for the interpolation of $\boldsymbol{f}_0$. Blue and red regions correspond to $\eta = 1$ and $\eta = 0$, respectively.

Fibres direction: we consider the surfaces described by the four ellipsoids of the ventricle. For each point of these surfaces, the unitary vector $\boldsymbol{f}_0$ will be considered to be tangential to them. Specifically, at each point of them, $\boldsymbol{f}_0$ forms an angle of $+60$ or -60 degrees with respect to its local circumferential axis. The angle is $+60$ in the first (outermost ellipsoid) and third ellipsoids, whereas the angle is -60 in the remaining ellipsoids (refer to Figure 19_b). A Poisson problem is solved in order to obtain the orientation of $\boldsymbol{f}_0$ in the interior of the ventricles [13] (at Gauss point level). This is done by introducing the intermediate field η, satisfying $\boldsymbol{\nabla}_0 \cdot (\boldsymbol{\nabla}_0 \eta) = 0$ in Ω_0, where $\eta = 1$ in the ellipsoidal surfaces associated with a $+60$ orientation of $\boldsymbol{f}_0$ and $\eta = 0$ in the remaining ellipsoidal surfaces (refer to Figure 19_c). In addition, this intermediate field helps to compute the normal unit vector $\boldsymbol{s}_0$ as $\boldsymbol{\nabla}_0 \eta / \|\boldsymbol{\nabla}_0 \eta\|$. With all this information, the direction $\boldsymbol{f}_0$ is then calculated by means of Rodrigues' rotation formula as explained in Reference [10]. Finally, the remaining direction $\boldsymbol{n}_0$ is computed as $\boldsymbol{n}_0 = \boldsymbol{f}_0 \times \boldsymbol{s}_0$.

Boundary conditions: homogeneous Dirichlet boundary conditions are applied on the coloured regions in Figure 20_a. Homogeneous Neumann boundary conditions are applied elsewhere.

Initial conditions: the cardiac action potential is triggered by means of an arbitrary stimulation intensity I_{stim} applied on the coloured region in Figure 20_b.

$$\text{(a)} \qquad\qquad\qquad\qquad \text{(b)}$$
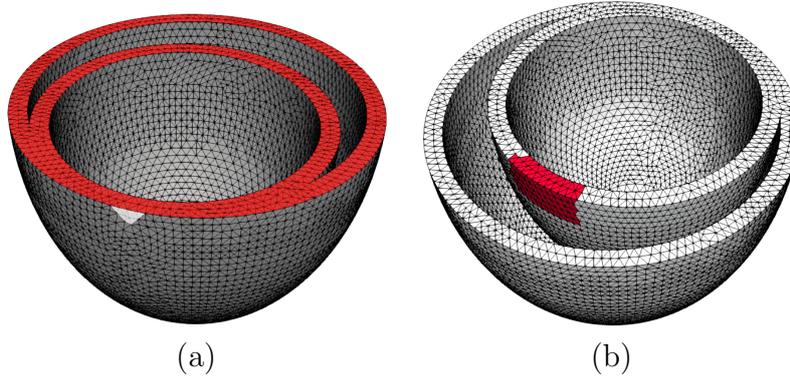
Figure 20: Numerical example 4. **(a)** Regions for the application of homogeneous Dirichlet boundary conditions for displacements. In red: restriction displacement in OZ direction; in white: restriction in all directions. **(b)** Region where the initial electrical stimulation occurs.

Time integration: an adaptive time step strategy is used for the time integration of equation (4). A small time step Δt is required in order to correctly capture the rapid initial depolarisation and can then be gradually increased without compromising the accuracy of the simulation. The time step Δt at a given time t is automatically chosen by measuring the rate of change in absolute value of the internal variables in the ionic models (see Sections 4.2). The minimum and maximum values for Δt are 0.3 ms and 50 ms, respectively. Furthermore, the time integration of equation (4), the evolution equations for the activation laws for T_a (49) and $\gamma_{\boldsymbol{f}_0}$ (52) and the ODE for the internal variables $\boldsymbol{q}$ in (45) is carried out by means of the (implicit) Backward-Euler scheme.

Material parameters: Table 22 contains the values for the relevant material parameters for: **(a)** Holzapfel-Ogden model [24] in (18); **(b)** activation model proposed by Nash and Panfilov [51]; **(c)** activation model proposed by Wong *et al.* [52]. **(d)** activation model proposed by Rossi *et al.* [10]; **(e)** ionic model proposed by Bueno-Orovio *et al.* [1]; **(f)** ionic model proposed by Ten Tusscher *et al.* [49]; **(g)** parameters controlling diffusion in (63).

7.4.1. Comprehensive simulation using the new mixed formulations in Sections 5.2.1 and 5.2.1

In order to address objective **O4.I**, four different simulations will be carried out in this example. For the four simulations, the *passive response* is that proposed by Holzapfel-Ogden [24] in (18). The material parameters for this model can be found in Figure 22_a. The values of the parameters controlling diffusion in equation (63) are in Figure 22_g. The remaining details of the simulations can be found below and also in Figure 21.

Simulation-I: the *coupling type* considered is active stress. The *mixed formulation* ELEM1-**MFA**-T_a is used. The *activation law* is that of Nash & Panfilov [63] (see Figure 22_b). The *ionic model* chosen is the Bueno-Orovio model [1] (see Figure 22_e).

Simulation-II: the *coupling type* considered is active stress. The *mixed formulation* ELEM1-**MFA**-T_a is used in this case. The *activation law* is that of Wong & Kuhl [52] (see Figure 22_c). The *ionic model* chosen is the Ten Tusscher model [2] (see Figure 22_f).

Simulation-III: the *coupling type* considered is active strain. The *mixed formulation* ELEM1-**MFA**-γ is used in this case. The *activation law* is that of Rossi *et al.* [10] (see Figure 22_d). The *ionic model* chosen is the Bueno-Orovio model [1] (see Figure 22_e).

Simulation-IV: the *coupling type* considered is active strain. The *mixed formulation* ELEM1-**MFA**-γ is used in this case. The *activation law* is that of Rossi *et al.* [10] (see Figure 22_d). The *ionic model* chosen is the Ten Tusscher model [2] (see Figure 22_f).

31

Summary of details for the four simulation					
Simulation name	**Coupling type**	**Activation Law**	**Ionic Model**	**Passive response**	**Mixed Formulation**
Simulation-I	Active Stress	Nash & Panfilov	Bueno-Orovio	Holzapfel-Ogden	ELEM1-**MFA**-T_a
Simulation-II	Active Stress	Wong & Kuhl	Ten Tusscher	Holzapfel-Ogden	ELEM1-**MFA**-T_a
Simulation-III	Active Strain	Rossi *et al.*	Bueno-Orovio	Holzapfel-Ogden	ELEM1-**MFA**-γ
Simulation-IV	Active Strain	Rossi *et al.*	Ten Tusscher	Holzapfel-Ogden	ELEM1-**MFA**-γ

Figure 21: Numerical example 4.1. Description of the four simulations considered.

The number of degrees of freedom for the various simulations is: $\{525705, 175235, 112088\}$ for $\{\boldsymbol{x}, \phi, p\}$ and $\{4035168, 4035168, 112088, 1345056\}$ for $\{\boldsymbol{F}, \boldsymbol{H}, J, \boldsymbol{A}\}$ and $\{\boldsymbol{\Sigma_F}, \boldsymbol{\Sigma_H}, \Sigma_J, \boldsymbol{\Sigma_A}\}$, where the static condensation procedure in Section 6.2.1 is used in order to condense out the fields $\{\boldsymbol{F}, \boldsymbol{H}, J, \boldsymbol{A}\}$ and $\{\boldsymbol{\Sigma_F}, \boldsymbol{\Sigma_H}, \Sigma_J, \boldsymbol{\Sigma_A}\}$.

Tables 3-4, 5-6, 7-8 and 9-10 display the results obtained for: Simulation-I, Simulation-II, Simulation-III and Simulation-IV (refer to Figure 21), respectively. The contour plot distribution of relevant variables of interest are plotted for different snapshots of the cardiac cycle. From these pictures it is worth emphasising the similarities in the mechanical contraction obtained from Simulation-I and Simulation-II (Tables 3-4, 5-6). Moreover, the mechanical contraction from Simulation-III and Simulation-IV are very similar (Tables 7-8, 9-10). These similarities are due to the use of the same coupling type in Simulation-I and Simulation-II (active stress in both) and in Simulation-III and Simulation-IV (active strain in both). Even though the ionic model used in Simulation-I and Simulation-II were different (Bueno-Orovio and Ten Tusscher, respectively), there is a very good agreement between the results of both simulations. The same can be said regarding Simulation-III and Simulation-IV. This similarity is due to fact that both ionic models (Bueno-Orovio and Ten Tusscher) have been calibrated to reproduce the cardiac cycle. Hence, provided that the activation type and the activation law are the same, the electrically induced contraction should be reasonably similar.

However, the activation laws for T_a (49) (active stress) or $\gamma_{\boldsymbol{f}_0}$ (52) (active strain) have not been calibrated to obtain a similar electrically induced mechanical response to the best of the authors' knowledge. In our study, we have limited to use the material parameters reported in the available literature for the three activation laws in Figures 22_b-22_d considered. This explains the dissimilarities between Simulation-I (or Simulation-II) and Simulation-III (or Simulation-IV).

7.5. Numerical example 4.2: comparison against P_1-P_1 element

This example addresses objective **O4.II**. We model in this example the cardiac cycle considering an active stress approach, the Nash & Panfilov [63] activation law for T_a and the Bueno-Orovio [1] ionic model. For the passive response we use Holzapfel-Ogden model (18). The relevant material parameters can be found in Figure 22.

We then compare the ELEM1-**MFA**-T_a formulation against a conventional formulation where the unknown fields are the geometry $\boldsymbol{x}$ and the transmembrane potential ϕ. Truly incompressibility is not enforced in this formulation. Instead, nearly incompressibility is enforced by means of high value for κ in the volumetric functional $U(J_{\boldsymbol{x}})$ in (18). In this formulation, $\{\boldsymbol{x} - \phi\}$ are interpolated using linear tetrahedral Finite Elements. We denote this formulation as P_1-P_1.

The number of degrees of freedom for the ELEM1-**MFA**-T_a is: $\{525705, 175235, 112088\}$ for $\{\boldsymbol{x}, \phi, p\}$ and $\{4035168, 4035168, 112088, 1345056\}$ for $\{\boldsymbol{F}, \boldsymbol{H}, J, \boldsymbol{A}\}$ and $\{\boldsymbol{\Sigma_F}, \boldsymbol{\Sigma_H}, \Sigma_J, \boldsymbol{\Sigma_A}\}$, where the static condensation procedure in Section 6.2.1 is used in order to condense out the fields $\{\boldsymbol{F}, \boldsymbol{H}, J, \boldsymbol{A}\}$ and $\{\boldsymbol{\Sigma_F}, \boldsymbol{\Sigma_H}, \Sigma_J, \boldsymbol{\Sigma_A}\}$. For the P_1-P_1 formulation we use a discretisation with a number of degrees of freedom of $\{775668, 258556\}$ for $\{\boldsymbol{x}, \phi\}$. Our objective is to compare both formulations for a similar number of degrees of freedom for $\{\boldsymbol{x}, \phi\}$ for both ELEM1-**MFA**-T_a and P_1-P_1 formulations.

Parameters for the Holzapfel-Ogden constitutive law			
$a = 0.496$ kPa	$a_f = 15.196$ kPa	$a_s = 3.283$ kPa	$a_{fs} = 0.662$ kPa
$b = 7.209$	$b_f = 20.417$	$b_s = 11.176$	$b_{fs} = 9.466$

Parameters for the activation model proposed by Nash and Panfilov					
$k_{T_a} = 12.5$ kPa/μM	-	-	-	-

Parameters for the activation model proposed by Wong *et al.*					
$\eta = 12.5$ kPa/μM	$c_{Ca}^{crit} = 0.8$ μM	$c_{Ca,0} = 0.08$ μM	$\varepsilon_0 = 0.1$ ms^{-1}	$\varepsilon_\infty = 1$ ms^{-1}	$\xi = 4$ μM^{-1}

Parameters for the activation law proposed by Rossi *et al.*		
$d_1 = 2570.395355352195$	$e_2 = 302.216784558222$	$d_0 = -4333.618335582119$
$e_1 = -2051.827278991976$	$d_3 = 104.943770305116$	$\hat{\mu}_A = 5000$ ms μM^{-2}
$d_2 = 1329.536116891330$	$e_3 = 218.375174229422$	$l_0 = 1.95$ mm $\quad \alpha = -4$ μM^{-2}

Parameters for the Bueno-Orovio ionic model						
$u_o = 0.0$	$\theta_v = 0.3$	$\tau_{o1} = 400$	$\tau_{v1}^- = 60$	$w_\infty^* = 0.94$	$\tau_{s1} = 2.7342$	$k_w^- = 65$
$u_u = 1.55$	$\theta_w = 0.13$	$\tau_{o2} = 6$	$\tau_{v2}^- = 1150$	$\tau_{w1}^- = 60$	$\tau_{s2} = 16$	$k_s = 2.0994$
$u_s = 0.9087$	$\theta_o = 0.006$	$\tau_{so1} = 30.0181$	$\tau_w^+ = 200$	$\tau_{w2}^- = 15$	$\tau_{si} = 1.8875$	$k_{so} = 2.0458$
$u_w^- = 0.03$	$\theta_v^- = 0.006$	$\tau_{so2} = 0.9957$	$\tau_v^+ = 1.4506$	$\tau_{fi} = 0.11$	$\tau_w^\infty = 0.07$	$I_{stim} = 0.9$

Parameters for the Ten Tusscher ionic model			
$\alpha = 2.5$	$G_{Na} = 14.838$ nS/pF	$K_{Buf_{sr}} = 0.3$ mM	$V_C = 0.016404$ cm^3
$\gamma = 0.35$	$G_{K1} = 5.405$ nS/pF	$K_{up} = 0.00025$ mM	$V_{SR} = 0.001094$ cm^3
$T = 310$ K	$G_{to} = 0.245$ nS/pF	$K_{mNai} = 87.5$ mM	$V_{leak} = 0.00008$ ms^{-1}
$k_{sat} = 0.1$	$G_{Kr} = 0.0096$ nS/pF	$K_{pCa} = 0.0005$ mM	$a_{rel} = 0.016464$ mM/ms
$p_{KNa} = 0.03$	$G_{Ks} = 0.245$ nS/pF	$K_{mK} = 1$ mM	$b_{rel} = 0.25$ mM
$Ca_O = 2$ mM	$G_{pk} = 0.0146$ nS/pF	$K_{mNa} = 40$ mM	$c_{rel} = 0.008232$ mM/ms
$K_O = 5.4$ mM	$G_{pCa} = 0.825$ nS/pF	$K_{mCa} = 1.38$ mM	$V_{max,up} = 0.000425$ mM/ms
$Na_O = 140$ mM	$G_{bCa} = 0.000592$ nS/pF	$K_{Buf_c} = 0.001$ mM	$R = 8.3143$ mJ K/mM
$Buf_c = 0.15$ mM	$G_{bNa} = 0.00029$ nS/pF	$P_{NaK} = 1.362$ pA/pF	$F = 96.4867$ C/mM
$Buf_{sr} = 10$ mM	$G_{CaL} = 0.175$ mm^3/μF/s	$k_{NaCa} = 1000$ pA/pF	$C_m = 0.000185$ μF/cm^2

Additional parameters	
$d_{iso} = 8 \cdot 10^{-4}$ m^2/s	$d_{ani} = 12 \cdot 10^{-4}$ m^2/s

Figure 22: Numerical example 4. Parameters for: **(a)** Holzapfel-Ogden model [24] for passive response of the myocardium. Values provided in Göktepe *et al.* [40]; **(b)** Activation model proposed by Nash and Panfilov [51] (*activation type*: active stress; *ionic model*: Bueno-Orovio). **(c)** Activation model proposed by Wong *et al.* [52] (*activation type*: active stress; *ionic model*: Ten Tusscher). **(d)** Activation model proposed by Rossi *et al.* [10] (*activation type*: active strain; *ionic model*: both Bueno-Orovio and Ten Tusscher). **(e)** Ionic model proposed by Bueno-Orovio *et al.* [1]; **(f)** Ionic model proposed by Ten Tusscher *et al.* [49]. **(g)** Electrical conductivities in (63).
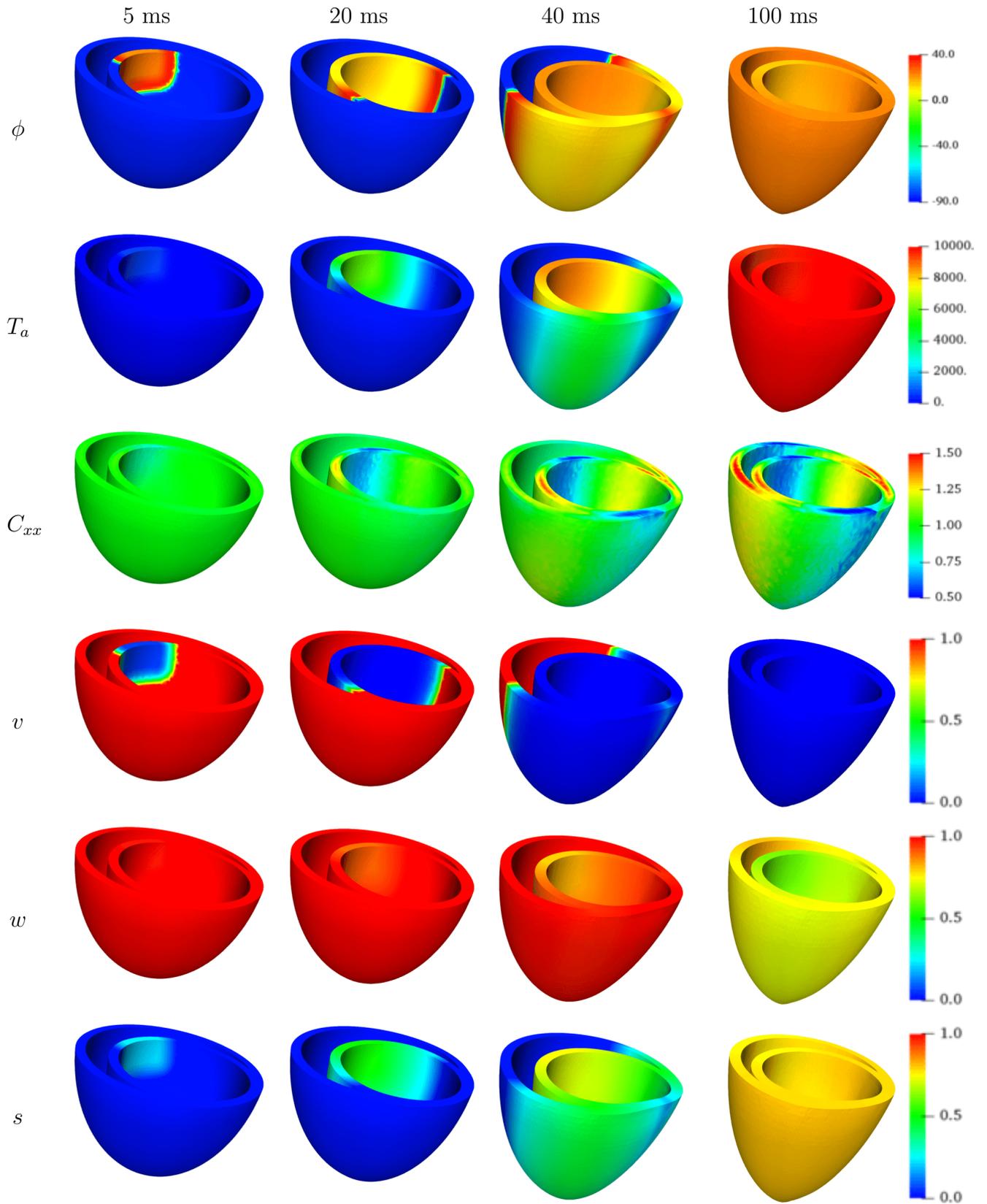
Table 3: Numerical example 4.1. **Simulation-I** (*activation type*: active stress; *ionic model*: Bueno-Ovorio; *activation law*: Nash & Panfilov; *mixed formulation*: ELEM1-**MFA**-T_a). Snapshots for time $t = \{5, 20, 40, 100\}$ (ms) of the cardiac cycle. Contour plot of ϕ (mV), cardiomyocite stress T_a (Pa), right Cauchy-Green tensor component C_{XX} and three internal variables, namely $\{v, w, s\}$.

34
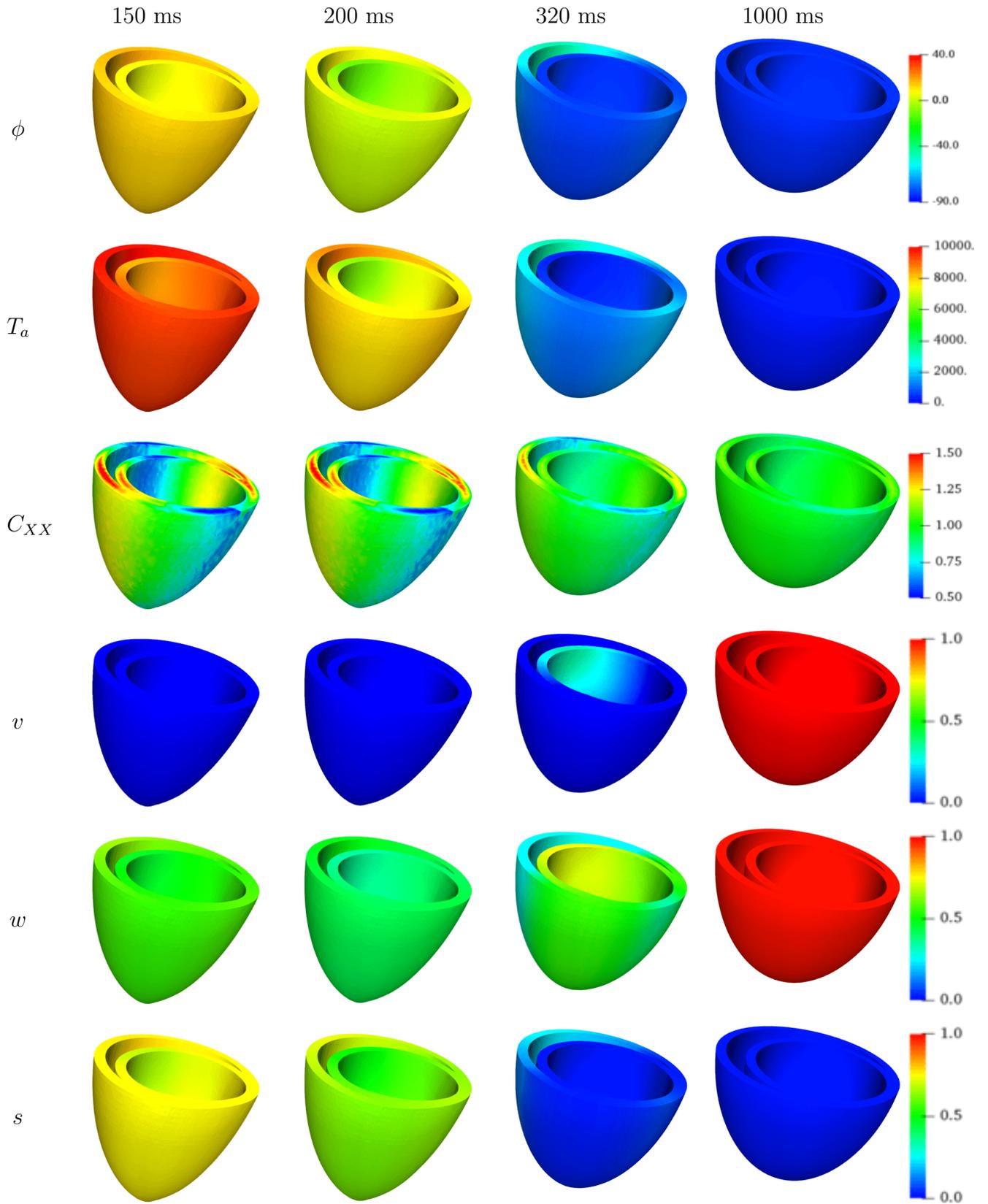
Table 4: Numerical example 4.1. **Simulation-I** (*activation type*: active stress; *ionic model*: Bueno-Ovorio; *activation law*: Nash & Panfilov; *mixed formulation*: ELEM1-**MFA**-T_a). Snapshots for time $t = \{150, 200, 320, 1000\}$ (ms) of the cardiac cycle. Contour plot of ϕ (mV), cardiomyocite stress T_a (Pa), right Cauchy-Green tensor component C_{XX} and three internal variables, namely $\{v, w, s\}$.

Table 5: Numerical example 4.1. Results for **Simulation-II** (*activation type*: active stress; *ionic model*: Ten Tusscher; *activation law*: Wong & Kuhl; *mixed formulation*: ELEM1-**MFA**-T_a). Snapshots for time $t = \{5, 20, 40, 100\}$ (ms) of the cardiac cycle. Contour plot of ϕ (mV), cardiomyocite stress T_a (Pa), right Cauchy-Green tensor component C_{XX} and three ionic concentrations, namely, $\{Ca^{++}, Na^+, K^+\}$ (units of mM).
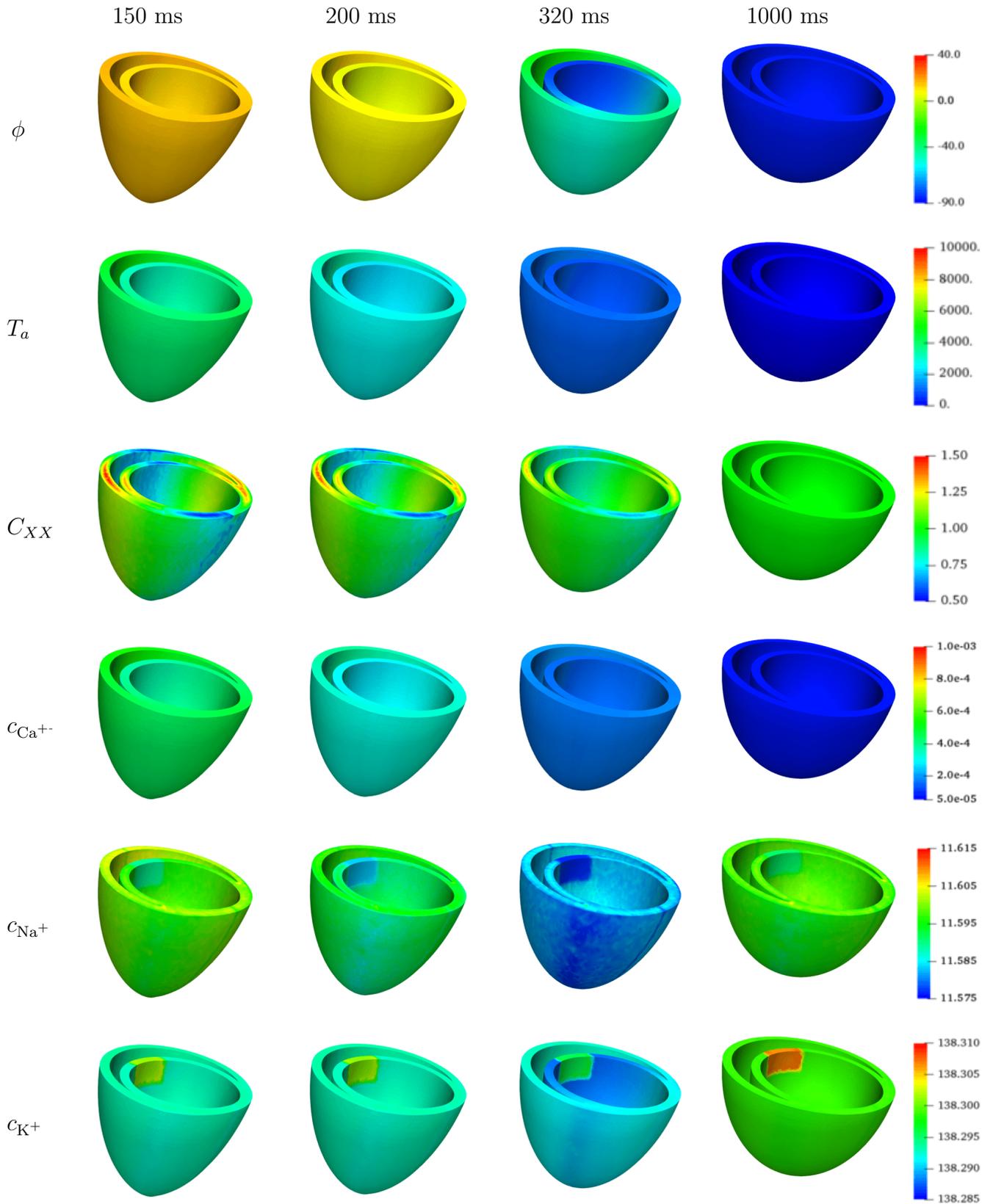
Table 6: Numerical example 4.1. Results for **Simulation-II** (*activation type*: active stress; *ionic model*: Ten Tusscher; *activation law*: Wong & Kuhl; *mixed formulation*: ELEM1-**MFA**-T_a). Snapshots for time $t = \{150, 200, 320, 1000\}$ (ms) of the cardiac cycle. Contour plot of ϕ (mV), cardiomyocite stress T_a (Pa), right Cauchy-Green tensor component C_{XX} and three ionic concentrations, namely, $\{Ca^{++}, Na^+, K^+\}$ (units of mM).
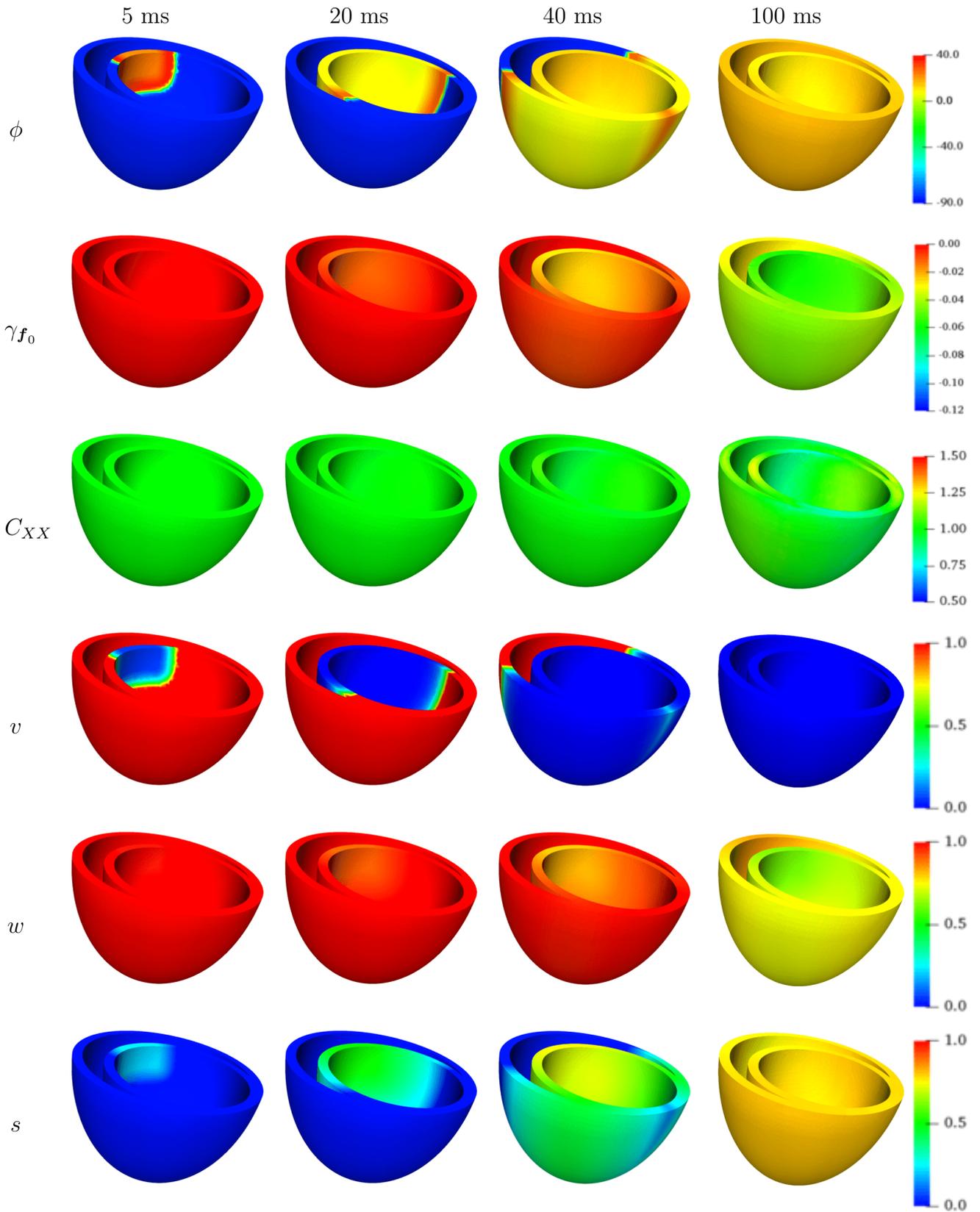
Table 7: Numerical example 4.1. **Simulation-III** (*activation type*: active strain; *ionic model*: Bueno-Ovorio; *activation law*: Rossi *et al.*; *mixed formulation*: ELEM1-**MFA**-γ). Snapshots for time $t = \{5, 20, 40, 100\}$ (ms) of the cardiac cycle. Contour plot of ϕ (mV), electrical stretch $\gamma_{\boldsymbol{f}_0}$, right Cauchy-Green tensor component C_{XX} and three internal variables, namely $\{v, w, s\}$.
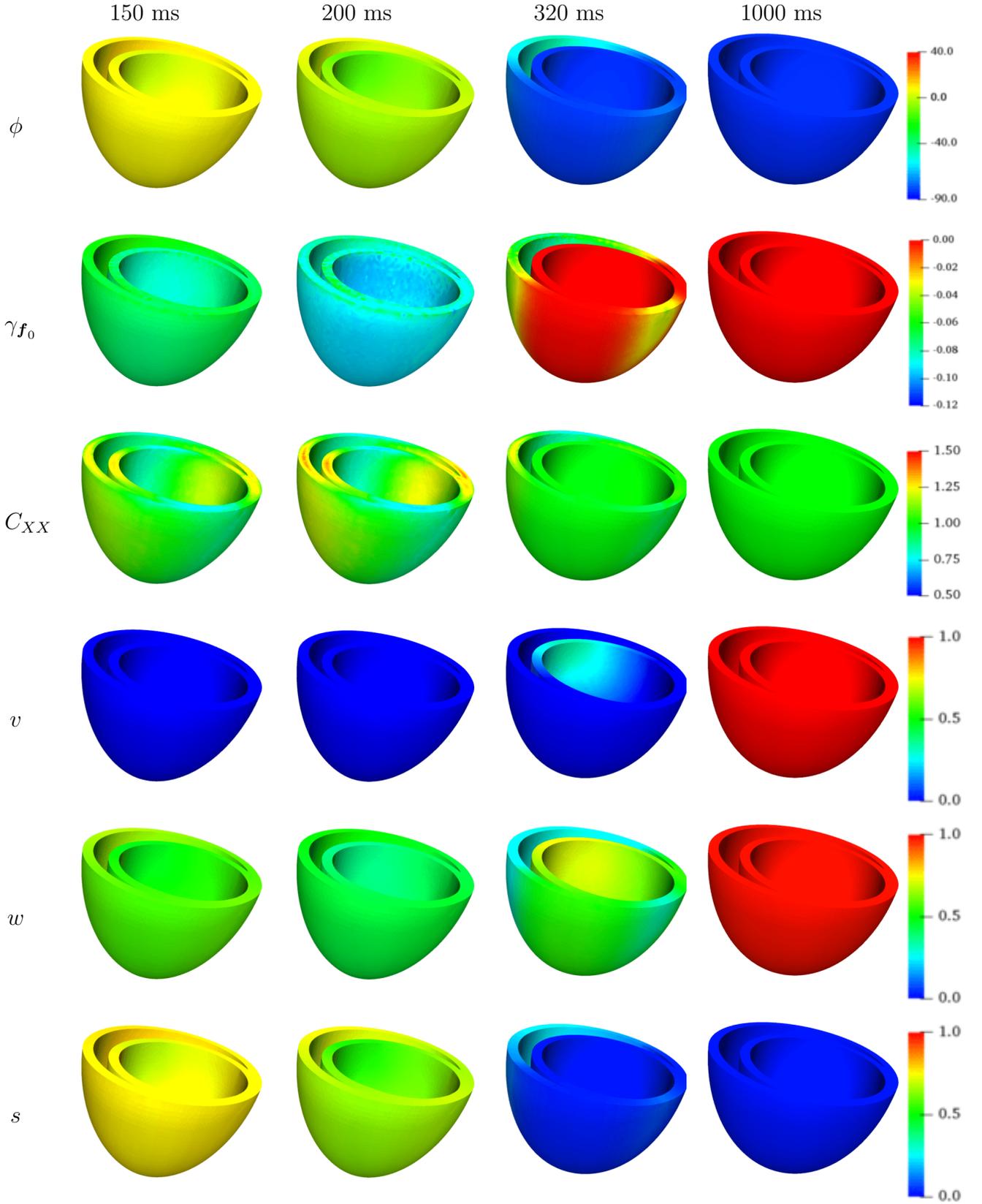
Table 8: Numerical example 4.1. **Simulation-III** (*activation type*: active strain; *ionic model*: Bueno-Ovorio; *activation law*: Rossi *et al.*; *mixed formulation*: ELEM1-**MFA**-γ). Snapshots for time $t = \{150, 200, 320, 1000\}$ (ms) of the cardiac cycle. Contour plot of ϕ (mV), electrical stretch $\gamma_{\boldsymbol{f}_0}$ (Pa), right Cauchy-Green tensor component C_{XX} and three internal variables, namely $\{v, w, s\}$.
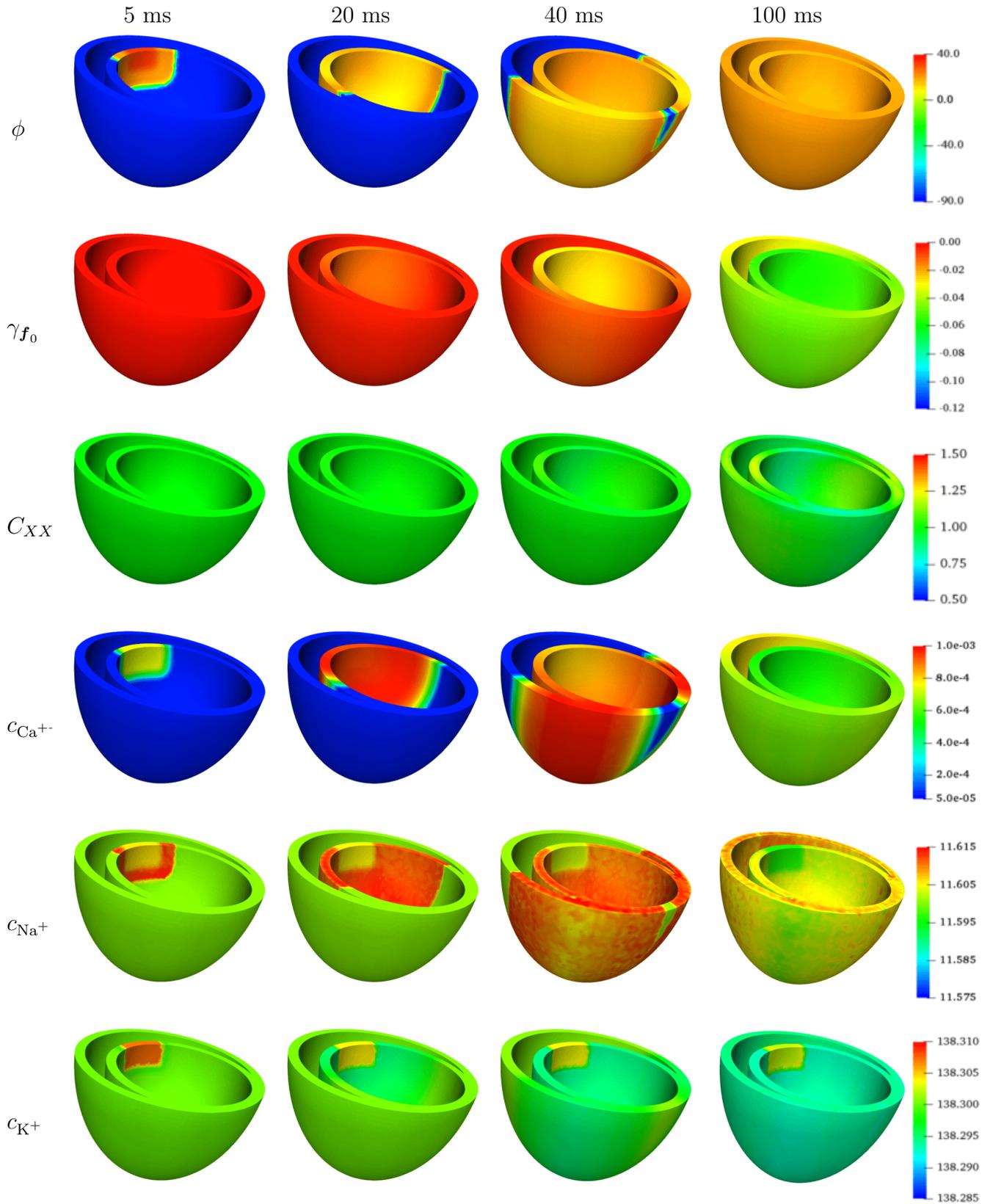
Table 9: Numerical example 4.1. Results for **Simulation-IV** (*activation type*: active strain; *ionic model*: Ten Tusscher; *activation law*: Rossi *et al.*; *mixed formulation*: ELEM1-**MFA**-γ). Snapshots for time $t = \{5, 20, 40, 100\}$ (ms) of the cardiac cycle. Contour plot of ϕ (mV), electrical stretch $\gamma_{\boldsymbol{f}_0}$, right Cauchy-Green tensor component C_{XX} and three ionic concentrations, namely, $\{Ca^{++}, Na^{+}, K^{+}\}$ (units of mM).
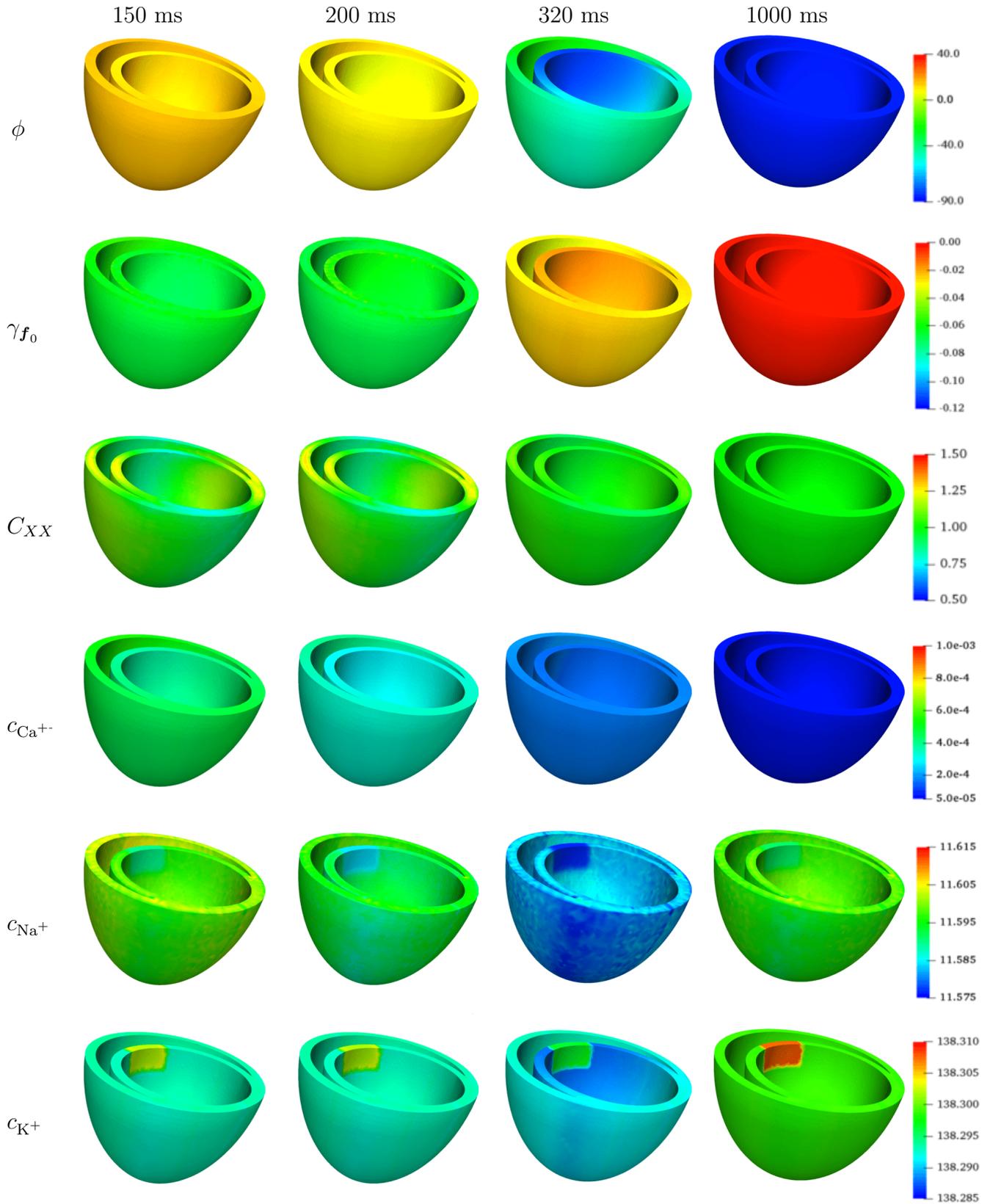
Table 10: Numerical example 4.1. Results for **Simulation-IV** (*activation type*: active strain; *ionic model*: Ten Tusscher; *activation law*: Rossi *et al.*; *mixed formulation:* ELEM1-**MFA**-γ). Snapshots for time $t = \{150, 200, 320, 1000\}$ (ms) of the cardiac cycle. Contour plot of ϕ (mV), electrical stretch $\gamma_{\boldsymbol{f}_0}$, right Cauchy-Green tensor component C_{XX} and three ionic concentrations, namely, $\{\mathrm{Ca}^{++}, \mathrm{Na}^+, \mathrm{K}^+\}$ (units of mM).

Table 11 shows the severe locking obtained with the P_1-P_1 formulation. A considerably smaller electrically induced contraction of the ventricles is obtained with this formulation in comparison to the ELEM1-**MFA**-T_a formulation. These results enable to conclude that the electrically induced deformation obtained by means of the P_1-P_1 is not reliable and hence, this formulation should not be used in this context.
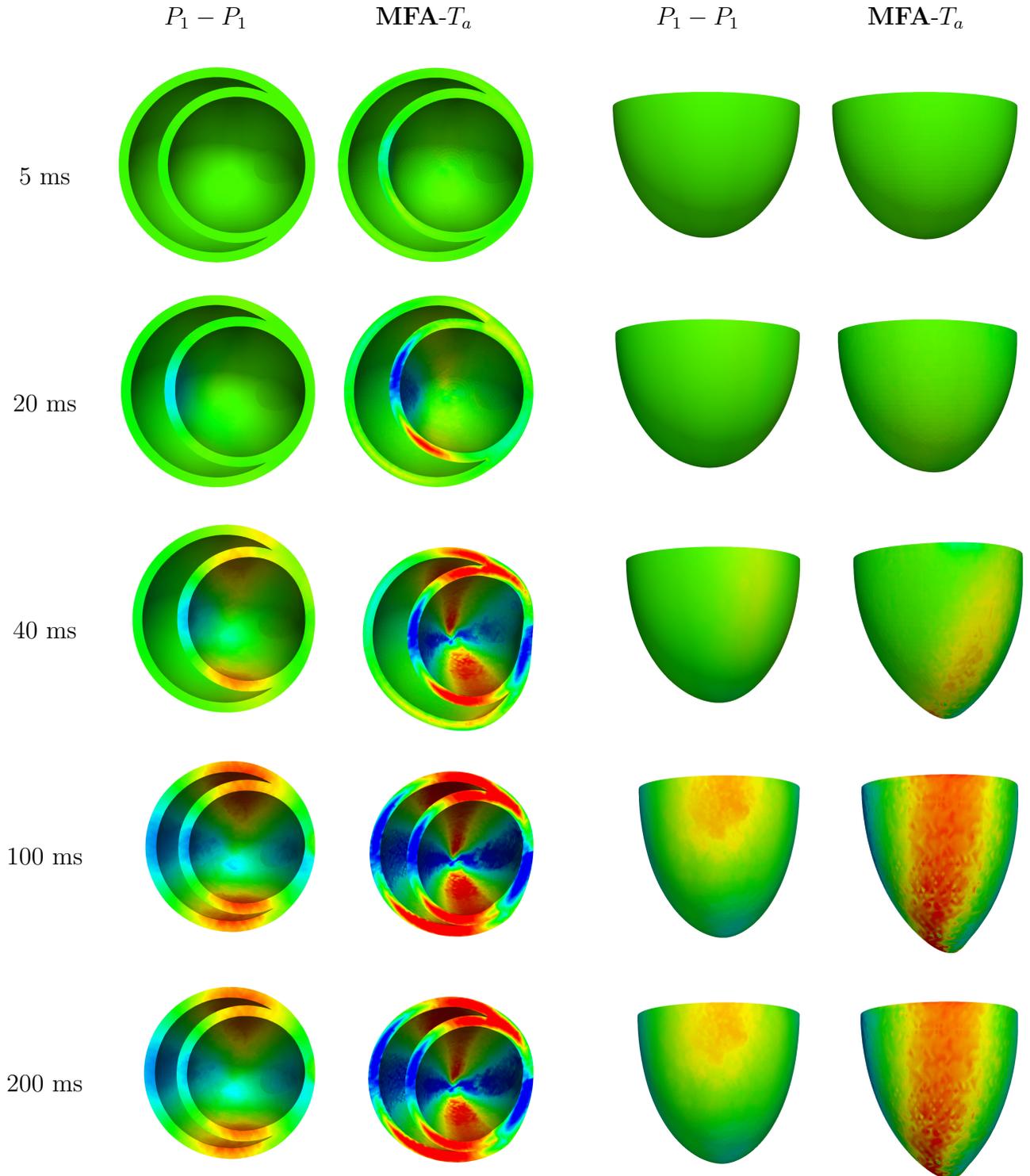
Table 11: Numerical example 4.2. *Activation type*: active stress; *ionic model*: Bueno-Orovio; *activation law*: Nash & Panfilov. Snapshots for time $t = \{20, 40, 100, 200\}$ (ms) of the cardiac cycle. Contour plot of right Cauchy-Green tensor component C_{XX}. Results for ELEM1-**MFA**-T_a and P_1-P_1 formulations.

7.6. Numerical example 4.3: analysis of possible loss of ellipticity of passive response

This example addresses objective **O4.III**. The susceptibility of Holzapfel-Ogden model (18) for the passive response of the myocardium is analysed when considering both active strain and active stress approaches. In addition, the influence of the consideration of the Macauly brackets in equation (18) upon the possible loss of ellipticity of this model is also studied. Mathematically, the consideration of these brackets implies that the energetic contributions in W^{ani} associated with the fibres $\{\boldsymbol{f}_0, \boldsymbol{s}_0\}$ are only active when the invariants $I_{4,\boldsymbol{f}_0}$ and $I_{4,\boldsymbol{s}_0}$ are positive. Physically, this means that the fibres contribute to the overall passive response when they are tractioned. On the contrary, not considering the Macaulay brackets implies assuming that these fibres contribute to the overall response even when they are compressed (i.e. when $I_{4,\boldsymbol{f}_0}$ and $I_{4,\boldsymbol{s}_0}$ are negative).

In order to analyse the possible loss of ellipticity, we study the positive definiteness of the acoustic tensor tensor $\boldsymbol{\mathcal{Q}_{VV}}$ in equation (16) for any direction $\boldsymbol{V}$. For any direction $\boldsymbol{V}$, spherically parametrised in terms of the angles $0 \leq \alpha \leq \pi$ and $0 \leq \beta \leq 2\pi$, i.e. $\boldsymbol{V} = \begin{bmatrix} \sin\alpha\cos\beta & \sin\alpha\sin\beta & \cos\alpha \end{bmatrix}$, the ellipticity indicator q is defined as $q = \min(q_1, q_2, q_3)$, with $\{q_1, q_2, q_3\}$ the leading minors of $\boldsymbol{\mathcal{Q}_{VV}}$. Negative values of q are associated with loss of ellipticity. Figures 12 and 13 show the distribution of q for different snapshots of the cardiac cycle for Simulation-I (active stress) and Simulation-III (active strain) when considering or when disregarding the Macaulay brackets at a given Gauss point of the idealised set of ventricles in 19. It can be observed that no loss of ellipticity was obtained at the given Gauss point when the Macaulay brackets are activated. However, when these are disabled, loss of ellipticity can be observed for both active stress and active strain approaches. Notice that negative values of q have been truncated to zero in both figures.

Figures 14 and 15 show the contour plot of the ellipticity indicator q over the entire domain when the Macaulay brackets in Holzapfel-Ogden model (18) are not considered for: **(a)** different snapshots of the cardiac circle and for **(b)** active stress and active strain approaches. In these figures, loss of ellipticity is associated with orange regions. Furthermore, both figures include the contour plot of an alternative instability indicator associated with loss of polyconvexity. Specifically, red areas in these figures are associated with the loss of positve definiteness of the Hessian operator $\mathbb{H}_W$ (12). Although polyconvexity and ellipticity are not equivalent concepts, an extremely good agreement between loss of ellipticity and loss of polyconvexity is obtained for the constitutive model considered. When considering the Macaulay brackets, loss of ellipticity was rarely detected.

This study is in good agreement with the derivations in Appendix A. Specifically, it demonstrates numerically that the strain energy in (18) is very prone to exhibit loss of ellipticity and hence, polyconvexity when the Macauly brackets are not considered in both active stress and active strain approaches.
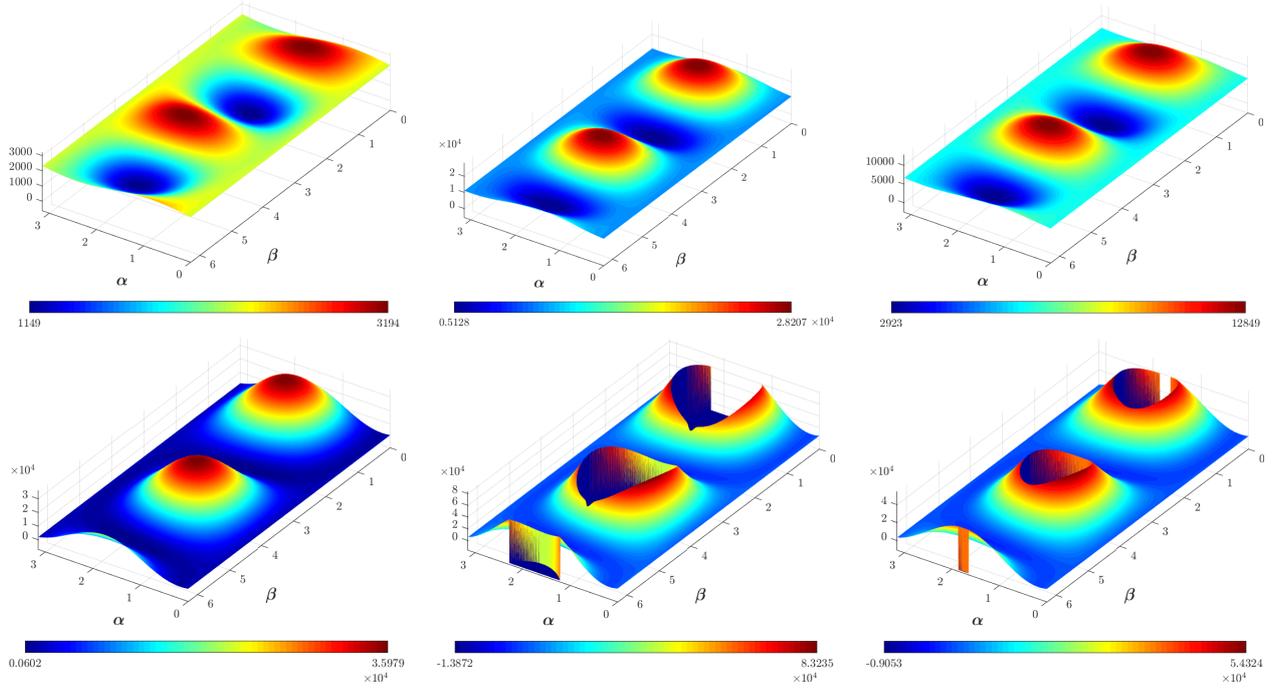
Table 12: Numerical example 4.3. Simulation details: *activation type*: active stress; *ionic model*: Bueno-Orovio; *activation law*: Nash & Panfilov; *mixed formulation*: ELEM1-**MFA**-T_a. Snapshots for time $t = \{2, 20, 40\}$ (ms) of the cardiac cycle. Ellipticity indicator q at a fixed Gauss point for angles α and β when considering Holzapfel-Ogden law in the case of: (upper row) with Macaulay brackets and (lower row) without Macaulay brackets. Loss of ellipticity in the later case.

Table 13: Numerical example 4.3. Simulation details: *activation type*: active strain; *ionic model*: Bueno-Orovio; *activation law*: Rossi *et al.*; *mixed formulation*: ELEM1-**MFA**-T_a. Snapshots for time $t = \{2, 20, 40\}$ (ms) of the cardiac cycle. Ellipticity indicator q at a fixed Gauss point for angles α and β when considering Holzapfel-Ogden law in the case of: (upper row) with Macaulay brackets and (lower row) without Macaulay brackets. Loss of ellipticity in the later case.

	Ellipticity	Polyconvexity		Ellipticity	Polyconvexity
20 ms			150 ms		
40 ms			250 ms		
80 ms			290 ms		
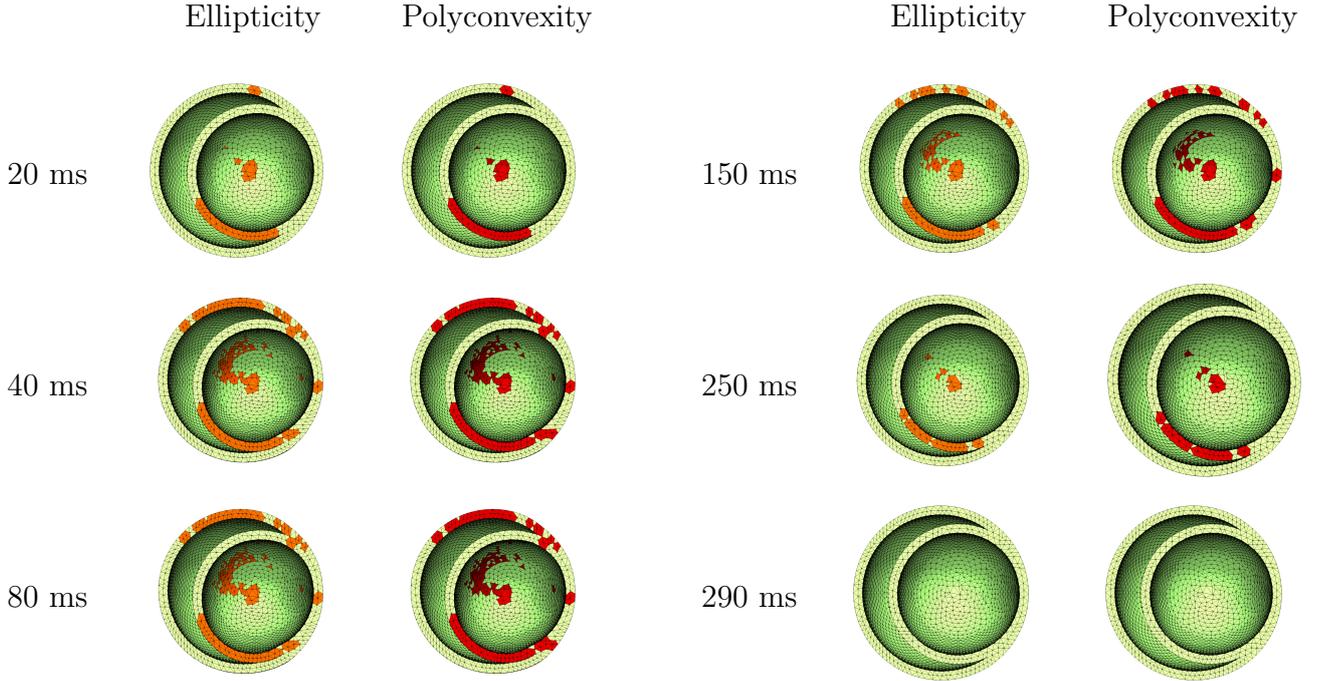
Table 14: Numerical example 4.3. Simulation details: *activation type*: active stress; *ionic model*: Bueno-Orovio; *activation law*: Nash & Panfilov; *mixed formulation*: ELEM1-**MFA**-T_a. Snapshots for time $t = \{20, 40, 80, 150, 250, 290\}$ (ms) of the cardiac cycle. Loss of ellipticity (orange regions) and loss of polyconvexity (red regions) when the Macaulay brackets are not considered in Holzapfel-Ogden model (18).

	Ellipticity	Polyconvexity		Ellipticity	Polyconvexity
20 ms			110 ms		
40 ms			250 ms		
80 ms			290 ms		
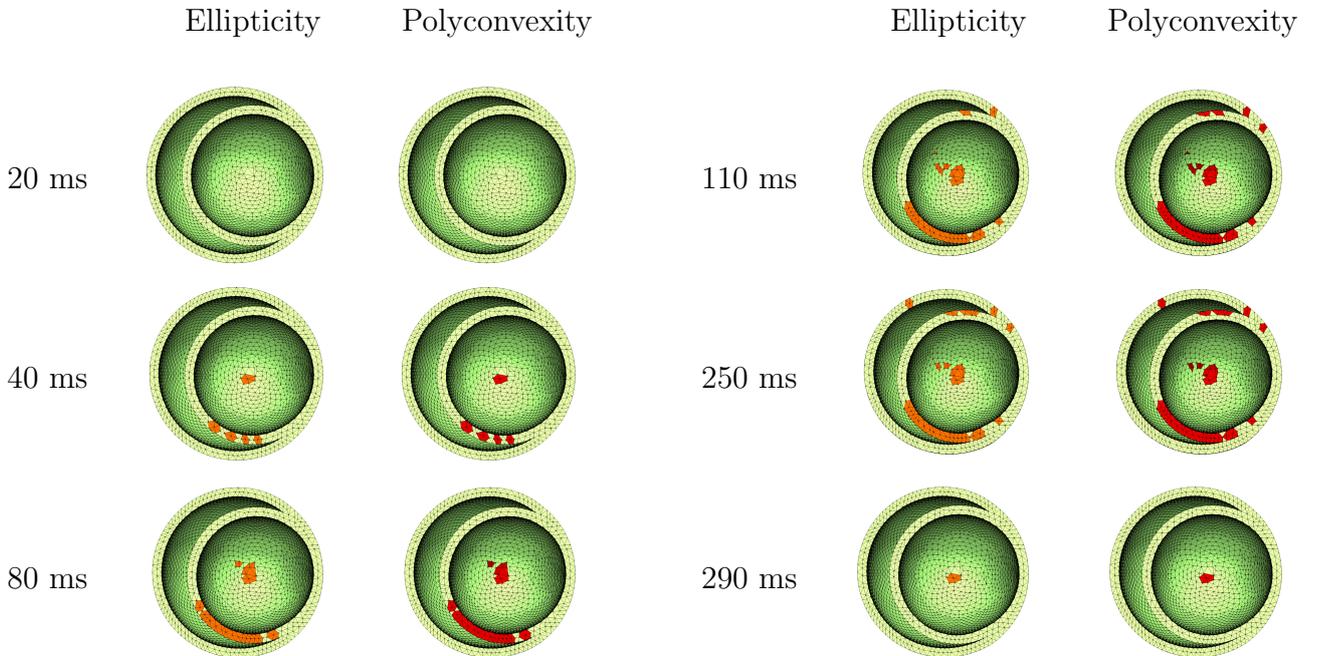
Table 15: Numerical example 4.3. Simulation details: *activation type*: active strain; *ionic model*: Bueno-Orovio; *activation law*: Rossi *et al.*; *mixed formulation*: ELEM1-**MFA**-T_a. Snapshots for time $t = \{10, 20, 40, 80, 150, 250, 290, 320\}$ (ms) of the cardiac cycle. Loss of ellipticity (orange regions) and loss of polyconvexity (red regions) when the Macaulay brackets are not considered in Holzapfel-Ogden model (18).

8. Concluding remarks

This paper presents a novel computational framework for the numerical simulation of the electromechanical response of the myocardium during the cardiac cycle. Two new mixed formulations, *tailor-made* for active stress and active strain coupling approaches, have been developed and used in conjunction with two different ionic models, namely Bueno-Orovio [1] and Ten Tusccher [2, 49]. Taking as a reference the mixed formulations introduced by Bonet *et al.* [3] in the context of nonlinear elasticity, the proposed formulations include as unknown fields the geometry and the transmembrane potential (and possibly a Lagrange multiplier enforcing weakly the incompressibility constraint) as well as the deformation gradient tensor, its cofactor and its determinant, the gradient of the transmembrane potential and their respective work conjugates. The Finite Element implementation of these formulations is shown in this paper. Crucially, the superiority of these formulations with respect to classical low order Finite Element implementations is shown in this paper. A comprehensive and rigorous study of different ionic models (i.e Bueno-Orovio and Ten Tusscher) and electromechanical activation couplings (i.e active strain and active stress) has been carried out. An analytical and numerical analysis of the possible loss of ellipticity and polyconvexity of one of the most widely used constitutive models in the context of cardiac mechanics is carried out in this paper, putting forward possible polyconvexifications of the existing model. (4) In addition, an invariant representation of Guccione's constitutive model is proposed. Finally, a series of numerical examples are included in order to demonstrate the applicability and robustness of the proposed formulations.

The computational framework developed in this manuscript will be used in a follow up publication with the aim of carrying out a thorough investigation of different solution techniques for the coupled electromechanical problem. Specifically, the accuracy and computational efficiency of staggered schemes will be analysed and compared to those of the monolithical approach advocated for in this paper. The conclusions of this forthcoming study could be very beneficial for the analysis of more complex and computationally demanding simulations such as those involving the simulation of cardiac arrhythmias.

Appendix A. Ellipticity (rank-one convexity) of Holzapfel-Ogden model for passive response of myocardium

In this Section we study the possible loss of ellipticity of the constitutive model in equation (18). For this, we introduce an additive decomposition of the ellipticity indicator $\mathcal{I}_W$ in (15) as

$$\mathcal{I}_{\mathcal{W}} = \mathcal{I}_{\hat{W}} + \mathcal{I}_U + \mathcal{I}_{W_{\boldsymbol{f}_0}^{\mathrm{ani}}} + \mathcal{I}_{W_{\boldsymbol{s}_0}^{\mathrm{ani}}} + \mathcal{I}_{W_{\boldsymbol{f}_0 \boldsymbol{s}_0}^{\mathrm{ani}}} \tag{A.1}$$

with each term defined as

$$
\begin{aligned}
\mathcal{I}_{\hat{W}} &= D^2 \hat{W} [\boldsymbol{u} \otimes \boldsymbol{V}; \boldsymbol{u} \otimes \boldsymbol{V}]; \\
\mathcal{I}_U &= D^2 U [\boldsymbol{u} \otimes \boldsymbol{V}; \boldsymbol{u} \otimes \boldsymbol{V}]; \\
\mathcal{I}_{W_{\boldsymbol{f}_0}^{\mathrm{ani}}} &= D^2 \left(\frac{a_f}{2b_f} \left(e^{b_f \langle I_{4,\boldsymbol{f}_0} - 1 \rangle^2} - 1 \right) \right) [\boldsymbol{u} \otimes \boldsymbol{V}; \boldsymbol{u} \otimes \boldsymbol{V}]; \\
\mathcal{I}_{W_{\boldsymbol{s}_0}^{\mathrm{ani}}} &= D^2 \left(\frac{a_s}{2b_s} \left(e^{b_s \langle I_{4,\boldsymbol{s}_0} - 1 \rangle^2} - 1 \right) \right) [\boldsymbol{u} \otimes \boldsymbol{V}; \boldsymbol{u} \otimes \boldsymbol{V}]; \\
\mathcal{I}_{W_{\boldsymbol{f}_0 \boldsymbol{s}_0}^{\mathrm{ani}}} &= D^2 \left(\frac{a_{fs}}{2b_{fs}} \left(e^{b_{fs} I_{8,\boldsymbol{f}_0,\boldsymbol{s}_0}^2} - 1 \right) \right) [\boldsymbol{u} \otimes \boldsymbol{V}; \boldsymbol{u} \otimes \boldsymbol{V}].
\end{aligned}
\tag{A.2}
$$

The ellipticity indicator for the isochoric isotropic term can be expressed as

$$
\begin{aligned}
\mathcal{I}_{\hat{W}} &= abe^{b\left(II_{\hat{F}_{\boldsymbol{x}}} - 3\right)} J_{\boldsymbol{x}}^{-10/3} \alpha^2 + ae^{b\left(II_{\hat{F}_{\boldsymbol{x}}} - 3\right)} J_{\boldsymbol{x}}^{-8/3} II_{\boldsymbol{A}} + \frac{a}{5} e^{b\left(II_{\hat{F}_{\boldsymbol{x}}} - 3\right)} J_{\boldsymbol{x}}^{-2/3} (\boldsymbol{u} \cdot \boldsymbol{u})(\boldsymbol{V} \cdot \boldsymbol{V}) \\
&\geq \frac{a}{5} e^{b\left(II_{\hat{F}_{\boldsymbol{x}}} - 3\right)} J_{\boldsymbol{x}}^{-2/3} (\boldsymbol{u} \cdot \boldsymbol{u})(\boldsymbol{V} \cdot \boldsymbol{V}) \geq 0.
\end{aligned}
\tag{A.3}
$$

with

$$
\alpha = \sqrt{2} J_{\boldsymbol{x}} (\boldsymbol{u} \cdot \boldsymbol{F}_{\boldsymbol{x}} \boldsymbol{V}) - \frac{\sqrt{2}}{3} (\boldsymbol{u} \cdot \boldsymbol{H}_{\boldsymbol{x}} \boldsymbol{V}) II_{\boldsymbol{F}_{\boldsymbol{x}}}; \qquad \boldsymbol{A} = \frac{2}{\sqrt{5}} J_{\boldsymbol{x}} (\boldsymbol{u} \otimes \boldsymbol{V}) - \frac{\sqrt{5}}{3} (\boldsymbol{u} \cdot \boldsymbol{H}_{\boldsymbol{x}} \boldsymbol{V}) \boldsymbol{F}_{\boldsymbol{x}}
\tag{A.4}
$$

For the volumetric contribution $U(J_{\boldsymbol{x}})$, $\mathcal{I}_U$ is obtained as

$$\mathcal{I}(U) = \kappa (\boldsymbol{u} \cdot \boldsymbol{H}_{\boldsymbol{x}} \boldsymbol{V})^2 \geq 0. \tag{A.5}$$

The anisotropic contribution $\mathcal{I}_{W_{\boldsymbol{f}_0}^{\mathrm{ani}}}$ can be obtained as

$$
\begin{aligned}
\mathcal{I}_{W_{\boldsymbol{f}_0}^{\mathrm{ani}}} &= 4 \left(2b_f \langle I_{4,\boldsymbol{f}_0} - 1 \rangle^2 + 1 \right) a_f e^{b_f \langle I_{4,\boldsymbol{f}_0} - 1 \rangle^2} (\boldsymbol{u} \cdot \boldsymbol{F}_{\boldsymbol{x}} \boldsymbol{f}_0)^2 (\boldsymbol{V} \cdot \boldsymbol{f}_0)^2 \\
&\quad + 2a_f e^{b_f \langle I_{4,\boldsymbol{f}_0} - 1 \rangle^2} \langle I_{4,\boldsymbol{f}_0} - 1 \rangle (\boldsymbol{u} \cdot \boldsymbol{u})(\boldsymbol{V} \cdot \boldsymbol{f}_0)^2 \geq 0.
\end{aligned}
\tag{A.6}
$$

Similarly, the anisotropic contribution $\mathcal{I}_{W_{\boldsymbol{s}_0}^{\mathrm{ani}}}$ can be obtained as

$$
\begin{aligned}
\mathcal{I}_{W_{\boldsymbol{s}_0}^{\mathrm{ani}}} &= 4 \left(2b_s \langle I_{4,\boldsymbol{s}_0} - 1 \rangle^2 + 1 \right) a_s e^{b_s \langle I_{4,\boldsymbol{s}_0} - 1 \rangle^2} (\boldsymbol{u} \cdot \boldsymbol{F}_{\boldsymbol{x}} \boldsymbol{s}_0)^2 (\boldsymbol{V} \cdot \boldsymbol{s}_0)^2 \\
&\quad + 2a_s e^{b_s \langle I_{4,\boldsymbol{s}_0} - 1 \rangle^2} \langle I_{4,\boldsymbol{s}_0} - 1 \rangle (\boldsymbol{u} \cdot \boldsymbol{u})(\boldsymbol{V} \cdot \boldsymbol{s}_0)^2 \geq 0.
\end{aligned}
\tag{A.7}
$$

Finally, the anisotropic contribution $\mathcal{I}_{W_{\boldsymbol{f}_0 \boldsymbol{s}_0}^{\mathrm{ani}}}$ can be obtained as

$$
\begin{aligned}
\mathcal{I}_{W_{\boldsymbol{f}_0 \boldsymbol{s}_0}^{\mathrm{ani}}} &= \left(2b_{fs} I_{8,\boldsymbol{f}_0 \boldsymbol{s}_0}^2 + 1 \right) a_{fs} e^{b_{fs} I_{4,\boldsymbol{f}_0 \boldsymbol{s}_0}^2} ((\boldsymbol{u} \cdot \boldsymbol{F}_{\boldsymbol{x}} \boldsymbol{f}_0)(\boldsymbol{V} \cdot \boldsymbol{s}_0) + (\boldsymbol{u} \cdot \boldsymbol{F}_{\boldsymbol{x}} \boldsymbol{s}_0)(\boldsymbol{V} \cdot \boldsymbol{f}_0))^2 \\
&\quad + 2a_{fs} e^{b_{fs} I_{8,\boldsymbol{f}_0 \boldsymbol{s}_0}^2} I_{8,\boldsymbol{f}_0 \boldsymbol{s}_0} (\boldsymbol{u} \cdot \boldsymbol{u})(\boldsymbol{V} \cdot \boldsymbol{f}_0)(\boldsymbol{V} \cdot \boldsymbol{s}_0) \\
&\geq -2a_{fs} e^{b_{fs} I_{8,\boldsymbol{f}_0 \boldsymbol{s}_0}^2} I_{8,\boldsymbol{f}_0 \boldsymbol{s}_0} (\boldsymbol{u} \cdot \boldsymbol{u}) |(\boldsymbol{V} \cdot \boldsymbol{f}_0)(\boldsymbol{V} \cdot \boldsymbol{s}_0)|.
\end{aligned}
\tag{A.8}
$$

As a result, given the unconditional positiveness of $\mathcal{I}_{\hat{W}}$, $\mathcal{I}_U$, $\mathcal{I}_{W_{\boldsymbol{f}_0}^{\text{ani}}}$ and $\mathcal{I}_{W_{\boldsymbol{s}_0}^{\text{ani}}}$, the total ellipticity indicator $\mathcal{I}_W$ can be written as

$$\mathcal{I}_W \geq -2a_{fs}e^{b_{fs}I_{8,\boldsymbol{f}_0\boldsymbol{s}_0}^2}I_{8,\boldsymbol{f}_0\boldsymbol{s}_0}\left(\boldsymbol{u}\cdot\boldsymbol{u}\right)|\left(\boldsymbol{V}\cdot\boldsymbol{f}_0\right)\left(\boldsymbol{V}\cdot\boldsymbol{s}_0\right)|. \tag{A.9}$$

Alternatively, if the Macauly brackets are not considered, the anisotropic contributions $\mathcal{I}_{W_{\boldsymbol{f}_0}^{\text{ani}}}$ and $\mathcal{I}_{W_{\boldsymbol{s}_0}^{\text{ani}}}$ are

$$\begin{aligned}
\mathcal{I}_{W_{\boldsymbol{f}_0}^{\text{ani}}} &= 4\left(2b_f\left(I_{4,\boldsymbol{f}_0}-1\right)^2+1\right)a_f e^{b_f\left(I_{4,\boldsymbol{f}_0}-1\right)^2}\left(\boldsymbol{u}\cdot\boldsymbol{F_x f}_0\right)^2\left(\boldsymbol{V}\cdot\boldsymbol{f}_0\right)^2 \\
&\quad + 2a_f e^{b_f\left(I_{4,\boldsymbol{f}_0}-1\right)^2}\left(I_{4,\boldsymbol{f}_0}-1\right)\left(\boldsymbol{u}\cdot\boldsymbol{u}\right)\left(\boldsymbol{V}\cdot\boldsymbol{f}_0\right)^2 \\
&\geq -2a_f e^{b_f\left(I_{4,\boldsymbol{f}_0}-1\right)^2}|\left(I_{4,\boldsymbol{f}_0}-1\right)|\left(\boldsymbol{u}\cdot\boldsymbol{u}\right)\left(\boldsymbol{V}\cdot\boldsymbol{f}_0\right)^2 \\
\mathcal{I}_{W_{\boldsymbol{s}_0}^{\text{ani}}} &= 4\left(2b_s\left(I_{4,\boldsymbol{s}_0}-1\right)^2+1\right)a_s e^{b_s\left(I_{4,\boldsymbol{s}_0}-1\right)^2}\left(\boldsymbol{u}\cdot\boldsymbol{F_x s}_0\right)^2\left(\boldsymbol{V}\cdot\boldsymbol{s}_0\right)^2 \\
&\quad + 2a_s e^{b_f\left(I_{4,\boldsymbol{s}_0}-1\right)^2}\left(I_{4,\boldsymbol{s}_0}-1\right)\left(\boldsymbol{u}\cdot\boldsymbol{u}\right)\left(\boldsymbol{V}\cdot\boldsymbol{s}_0\right)^2 \\
&\geq -2a_s e^{b_s\left(I_{4,\boldsymbol{s}_0}-1\right)^2}|\left(I_{4,\boldsymbol{s}_0}-1\right)|\left(\boldsymbol{u}\cdot\boldsymbol{u}\right)\left(\boldsymbol{V}\cdot\boldsymbol{s}_0\right)^2.
\end{aligned} \tag{A.10}$$

The total contribution $\mathcal{I}_W$ when not considering the Macauly brackets is

$$\begin{aligned}
\mathcal{I}_W &= -2a_{fs}e^{b_{fs}I_{8,\boldsymbol{f}_0\boldsymbol{s}_0}^2}I_{8,\boldsymbol{f}_0\boldsymbol{s}_0}\left(\boldsymbol{u}\cdot\boldsymbol{u}\right)|\left(\boldsymbol{V}\cdot\boldsymbol{f}_0\right)\left(\boldsymbol{V}\cdot\boldsymbol{s}_0\right)|. \\
&\quad -2a_f e^{b_s\left(I_{4,\boldsymbol{f}_0}-1\right)^2}|\left(I_{4,\boldsymbol{f}_0}-1\right)|\left(\boldsymbol{u}\cdot\boldsymbol{u}\right)\left(\boldsymbol{V}\cdot\boldsymbol{f}_0\right)^2 \\
&\quad -2a_s e^{b_s\left(I_{4,\boldsymbol{s}_0}-1\right)^2}|\left(I_{4,\boldsymbol{s}_0}-1\right)|\left(\boldsymbol{u}\cdot\boldsymbol{u}\right)\left(\boldsymbol{V}\cdot\boldsymbol{s}_0\right)^2.
\end{aligned} \tag{A.11}$$

The larger number of terms in (B.21) as opposed to (B.18) leads therefore in general to a model which is more prone for loss of ellipticity, specially when fibres $\boldsymbol{f}_0$ and $\boldsymbol{s}_0$ are contracted, namely $I_{4,\boldsymbol{f}_0} < 0$ and $I_{4,\boldsymbol{s}_0} < 0$.

Appendix B. Invariant-based representation for Guccione's law

Guccione *et al.* modelled the heart tissue as a three-dimensional transverse isotropic material in [79] using a Fung-type exponential energy law [80] as

$$\Psi\left(\boldsymbol{E}^{\star}\right) = \frac{K}{2}\left(e^{Q\left(\boldsymbol{E}^{\star}\right)} - 1\right), \tag{B.1}$$

where $\boldsymbol{E}^{*}$ represents the local Green-Lagrange strain tensor, expressed with respect to the local basis $\{\boldsymbol{f}_0, \boldsymbol{s}_0, \boldsymbol{n}_0\}$. Let $\boldsymbol{R}$ be the rotation matrix from the local basis to the global system of coordinates. $\boldsymbol{E}^{\star}$ can be related to its global counterpart $\boldsymbol{E} = \frac{1}{2}\left(\boldsymbol{F}_{\boldsymbol{x}}^{T}\boldsymbol{F}_{\boldsymbol{x}} - \boldsymbol{I}\right)$ as $\boldsymbol{E}^{\star} = \boldsymbol{R}^{T}\boldsymbol{E}\boldsymbol{R}$. The exponent $Q\left(\boldsymbol{E}^{\star}\right)$ in (B.1) is defined in terms of the local Green-Lagrange strain tensor as

$$Q\left(\boldsymbol{E}^{\star}\right) = c_f E_{11}^{\star 2} + c_t\left(E_{22}^{\star 2} + E_{33}^{\star 2} + E_{23}^{\star 2} + E_{32}^{\star 2}\right) + c_{fs}\left(E_{12}^{\star 2} + E_{21}^{\star 2} + E_{13}^{\star 2} + E_{31}^{\star 2}\right), \tag{B.2}$$

where $\{K, c_f, c_t, c_{fs}\}$ represent material parameters. Let $\{\boldsymbol{e}_1, \boldsymbol{e}_2, \boldsymbol{e}_3\}$ be

$$\begin{bmatrix} 1 & 0 & 0 \end{bmatrix}^{T}; \qquad \begin{bmatrix} 0 & 1 & 0 \end{bmatrix}^{T}; \qquad \begin{bmatrix} 0 & 0 & 1 \end{bmatrix}^{T}. \tag{B.3}$$

Then $Q\left(\boldsymbol{E}^{\star}\right)$ can be expressed in terms of $\{\left(\boldsymbol{e}_1 \cdot \boldsymbol{E}^{\star}\boldsymbol{e}_1\right)^2, \boldsymbol{E}^{\star}\boldsymbol{e}_1 \cdot \boldsymbol{E}^{\star}\boldsymbol{e}_1, \boldsymbol{E}^{\star} : \boldsymbol{E}^{\star}\}$, as

$$Q\left(\boldsymbol{E}^{*}\right) = 4A\left(\boldsymbol{e}_1 \cdot \boldsymbol{E}^{*}\boldsymbol{e}_1\right)^2 + 4B\left(\boldsymbol{E}^{*}\boldsymbol{e}_1 \cdot \boldsymbol{E}^{*}\boldsymbol{e}_1\right) + 4C\left(\boldsymbol{E}^{*} : \boldsymbol{E}^{*}\right), \tag{B.4}$$

with

$$A = \frac{c_f - 2c_{fs} + c_t}{2}; \qquad B = \frac{c_{fs} - c_t}{4}; \qquad C = \frac{c_f}{4}. \tag{B.5}$$

Notice that the three invariants $\{\left(\boldsymbol{e}_1 \cdot \boldsymbol{E}^{\star}\boldsymbol{e}_1\right)^2, \boldsymbol{E}^{\star}\boldsymbol{e}_1 \cdot \boldsymbol{E}^{\star}\boldsymbol{e}_1, \boldsymbol{E}^{\star} : \boldsymbol{E}^{\star}\}$ can be equivalently expressed with respect to the global system of coordinates as

$$\boldsymbol{e}_1 \cdot \boldsymbol{E}^{\star}\boldsymbol{e}_1 = \boldsymbol{f}_0 \cdot \boldsymbol{E}\boldsymbol{f}_0; \qquad \boldsymbol{E}^{*} : \boldsymbol{E}^{*} = \boldsymbol{E} : \boldsymbol{E}; \qquad \boldsymbol{E}^{*}\boldsymbol{e}_1 \cdot \boldsymbol{E}^{*}\boldsymbol{e}_1 = \boldsymbol{E}\boldsymbol{f}_0 \cdot \boldsymbol{E}\boldsymbol{f}_0, \tag{B.6}$$

and hence, an equivalent expression for Q can be obtained in terms of the global Green-Lagrange strain tensor $\boldsymbol{E}$ as

$$Q\left(\boldsymbol{E}\right) = 4A\left(\boldsymbol{f}_0 \cdot \boldsymbol{E}\boldsymbol{f}_0\right)^2 + 4B\left(\boldsymbol{E}\boldsymbol{f}_0 \cdot \boldsymbol{E}\boldsymbol{f}_0\right) + 4C\left(\boldsymbol{E} : \boldsymbol{E}\right), \tag{B.7}$$

This (objective) invariant representation of Guccione's model is now very well suited for numerical simulation via Finite Element implementation. Alternatively, it is possible to express the invariants $\{\left(\boldsymbol{f}_0 \cdot \boldsymbol{E}\boldsymbol{f}_0\right)^2, \boldsymbol{E}\boldsymbol{f}_0 \cdot \boldsymbol{E}\boldsymbol{f}_0, \boldsymbol{E} : \boldsymbol{E}\}$ in terms of the kinematic strain measures $\{\boldsymbol{F}_{\boldsymbol{x}}, \boldsymbol{H}_{\boldsymbol{x}}, J_{\boldsymbol{x}}\}$ as

$$\boldsymbol{f}_0 \cdot \boldsymbol{E}\boldsymbol{f}_0 = \frac{I_{4,\boldsymbol{f}_0} - 1}{2};$$
$$\boldsymbol{E}\boldsymbol{f}_0 \cdot \boldsymbol{E}\boldsymbol{f}_0 = \frac{II_{\boldsymbol{F}_{\boldsymbol{x}}} I_{4,\boldsymbol{f}_0} - II_{\boldsymbol{H}_{\boldsymbol{x}}} + I_{4,\boldsymbol{H}_{\boldsymbol{x}},\boldsymbol{f}_0} - 2I_{4,\boldsymbol{f}_0} + 1}{4}; \qquad I_{4,\boldsymbol{H}_{\boldsymbol{x}},\boldsymbol{f}_0} = \boldsymbol{H}_{\boldsymbol{x}}\boldsymbol{f}_0 \cdot \boldsymbol{H}_{\boldsymbol{x}}\boldsymbol{f}_0; \tag{B.8}$$
$$\boldsymbol{E} : \boldsymbol{E} = \frac{II_{\boldsymbol{F}_{\boldsymbol{x}}}^2 - 2II_{\boldsymbol{H}_{\boldsymbol{x}}} - 2II_{\boldsymbol{F}_{\boldsymbol{x}}} + 3}{4}.$$

Making use of (B.8), $Q\left(\boldsymbol{E}^{\star}\right)$ can be equivalently expressed as $Q\left(\boldsymbol{E}\right) = \widetilde{Q}\left(\boldsymbol{F}_{\boldsymbol{x}}, \boldsymbol{H}_{\boldsymbol{x}}, J_{\boldsymbol{x}}\right)$, with

$$\widetilde{Q}\left(\boldsymbol{F}_{\boldsymbol{x}}, \boldsymbol{H}_{\boldsymbol{x}}, J_{\boldsymbol{x}}\right) = A\,Q_{\mathrm{aniso},1}\left(\boldsymbol{F}_{\boldsymbol{x}}\right) + B\,Q_{\mathrm{aniso},2}\left(\boldsymbol{F}_{\boldsymbol{x}}, \boldsymbol{H}_{\boldsymbol{x}}\right) + C\,Q_{\mathrm{iso}}\left(\boldsymbol{F}_{\boldsymbol{x}}, \boldsymbol{H}_{\boldsymbol{x}}, J_{\boldsymbol{x}}\right), \tag{B.9}$$

where

$$Q_{\mathrm{aniso},1}\left(\boldsymbol{F}_{\boldsymbol{x}}\right) = \left(I_{4,\boldsymbol{f}_0} - 1\right)^2;$$
$$Q_{\mathrm{aniso},2}\left(\boldsymbol{F}_{\boldsymbol{x}}, \boldsymbol{H}_{\boldsymbol{x}}\right) = II_{\boldsymbol{F}_{\boldsymbol{x}}} I_{4,\boldsymbol{f}_0} - II_{\boldsymbol{H}_{\boldsymbol{x}}} + I_{4,\boldsymbol{H}_{\boldsymbol{x}},\boldsymbol{f}_0} - 2I_{4,\boldsymbol{f}_0} + 1; \tag{B.10}$$
$$Q_{\mathrm{iso}}\left(\boldsymbol{F}_{\boldsymbol{x}}, \boldsymbol{H}_{\boldsymbol{x}}, J_{\boldsymbol{x}}\right) = II_{\boldsymbol{F}_{\boldsymbol{x}}}^2 - 2II_{\boldsymbol{H}_{\boldsymbol{x}}} - 2II_{\boldsymbol{F}_{\boldsymbol{x}}} + 3.$$

In this Section we study the possible loss of ellipticity of the constitutive model in equation (18). For this, we introduce an additive decomposition of the ellipticity indicator $\mathcal{I}_W$ in (15) as

$$\mathcal{I}_\mathcal{W} = \mathcal{I}_{\hat{W}} + \mathcal{I}_U + \mathcal{I}_{W_{\boldsymbol{f}_0}^{\mathrm{ani}}} + \mathcal{I}_{W_{\boldsymbol{s}_0}^{\mathrm{ani}}} + \mathcal{I}_{W_{\boldsymbol{f}_0\boldsymbol{s}_0}^{\mathrm{ani}}} \tag{B.11}$$

with each term defined as

$$\begin{aligned}
\mathcal{I}_{\hat{W}} &= D^2\hat{W}[\boldsymbol{u}\otimes\boldsymbol{V};\boldsymbol{u}\otimes\boldsymbol{V}]; \\
\mathcal{I}_U &= D^2 U[\boldsymbol{u}\otimes\boldsymbol{V};\boldsymbol{u}\otimes\boldsymbol{V}]; \\
\mathcal{I}_{W_{\boldsymbol{f}_0}^{\mathrm{ani}}} &= D^2\left(\frac{a_f}{2b_f}\left(e^{b_f\langle I_{4,\boldsymbol{f}_0}-1\rangle^2}-1\right)\right)[\boldsymbol{u}\otimes\boldsymbol{V};\boldsymbol{u}\otimes\boldsymbol{V}]; \\
\mathcal{I}_{W_{\boldsymbol{s}_0}^{\mathrm{ani}}} &= D^2\left(\frac{a_s}{2b_s}\left(e^{b_s\langle I_{4,\boldsymbol{s}_0}-1\rangle^2}-1\right)\right)[\boldsymbol{u}\otimes\boldsymbol{V};\boldsymbol{u}\otimes\boldsymbol{V}]; \\
\mathcal{I}_{W_{\boldsymbol{f}_0\boldsymbol{s}_0}^{\mathrm{ani}}} &= D^2\left(\frac{a_{fs}}{2b_{fs}}\left(e^{b_{fs}I_{8,\boldsymbol{f}_0,\boldsymbol{s}_0}^2}-1\right)\right)[\boldsymbol{u}\otimes\boldsymbol{V};\boldsymbol{u}\otimes\boldsymbol{V}].
\end{aligned} \tag{B.12}$$

The ellipticity indicator for the isochoric isotropic term can be expressed as

$$\begin{aligned}
\mathcal{I}_{\hat{W}} &= abe^{b\left(II_{\hat{\boldsymbol{F}}_{\boldsymbol{x}}}-3\right)}J_{\boldsymbol{x}}^{-10/3}\alpha^2 + ae^{b\left(II_{\hat{\boldsymbol{F}}_{\boldsymbol{x}}}-3\right)}J_{\boldsymbol{x}}^{-8/3}II_{\boldsymbol{A}} + \frac{a}{5}e^{b\left(II_{\hat{\boldsymbol{F}}_{\boldsymbol{x}}}-3\right)}J_{\boldsymbol{x}}^{-2/3}(\boldsymbol{u}\cdot\boldsymbol{u})(\boldsymbol{V}\cdot\boldsymbol{V}) \\
&\geq \frac{a}{5}e^{b\left(II_{\hat{\boldsymbol{F}}_{\boldsymbol{x}}}-3\right)}J_{\boldsymbol{x}}^{-2/3}(\boldsymbol{u}\cdot\boldsymbol{u})(\boldsymbol{V}\cdot\boldsymbol{V})\geq 0.
\end{aligned} \tag{B.13}$$

with

$$\alpha = \sqrt{2}J_{\boldsymbol{x}}(\boldsymbol{u}\cdot\boldsymbol{F}_{\boldsymbol{x}}\boldsymbol{V}) - \frac{\sqrt{2}}{3}(\boldsymbol{u}\cdot\boldsymbol{H}_{\boldsymbol{x}}\boldsymbol{V})II_{\boldsymbol{F}_{\boldsymbol{x}}}; \qquad \boldsymbol{A} = \frac{2}{\sqrt{5}}J_{\boldsymbol{x}}(\boldsymbol{u}\otimes\boldsymbol{V}) - \frac{\sqrt{5}}{3}(\boldsymbol{u}\cdot\boldsymbol{H}_{\boldsymbol{x}}\boldsymbol{V})\boldsymbol{F}_{\boldsymbol{x}} \tag{B.14}$$

For the volumetric contribution $U(J_{\boldsymbol{x}})$, $\mathcal{I}_U$ is obtained as

$$\mathcal{I}(U) = \kappa(\boldsymbol{u}\cdot\boldsymbol{H}_{\boldsymbol{x}}\boldsymbol{V})^2 \geq 0. \tag{B.15}$$

The anisotropic contribution $\mathcal{I}_{W_{\boldsymbol{f}_0}^{\mathrm{ani}}}$ can be obtained as

$$\begin{aligned}
\mathcal{I}_{W_{\boldsymbol{f}_0}^{\mathrm{ani}}} &= 4\left(2b_f\langle I_{4,\boldsymbol{f}_0}-1\rangle^2 + 1\right)a_f e^{b_f\langle I_{4,\boldsymbol{f}_0}-1\rangle^2}(\boldsymbol{u}\cdot\boldsymbol{F}_{\boldsymbol{x}}\boldsymbol{f}_0)^2(\boldsymbol{V}\cdot\boldsymbol{f}_0)^2 \\
&\quad + 2a_f e^{b_f\langle I_{4,\boldsymbol{f}_0}-1\rangle^2}\langle I_{4,\boldsymbol{f}_0}-1\rangle(\boldsymbol{u}\cdot\boldsymbol{u})(\boldsymbol{V}\cdot\boldsymbol{f}_0)^2 \geq 0.
\end{aligned} \tag{B.16}$$

Similarly, the anisotropic contribution $\mathcal{I}_{W_{\boldsymbol{s}_0}^{\mathrm{ani}}}$ can be obtained as

$$\begin{aligned}
\mathcal{I}_{W_{\boldsymbol{s}_0}^{\mathrm{ani}}} &= 4\left(2b_s\langle I_{4,\boldsymbol{s}_0}-1\rangle^2 + 1\right)a_s e^{b_s\langle I_{4,\boldsymbol{s}_0}-1\rangle^2}(\boldsymbol{u}\cdot\boldsymbol{F}_{\boldsymbol{x}}\boldsymbol{s}_0)^2(\boldsymbol{V}\cdot\boldsymbol{s}_0)^2 \\
&\quad + 2a_s e^{b_s\langle I_{4,\boldsymbol{s}_0}-1\rangle^2}\langle I_{4,\boldsymbol{s}_0}-1\rangle(\boldsymbol{u}\cdot\boldsymbol{u})(\boldsymbol{V}\cdot\boldsymbol{s}_0)^2 \geq 0.
\end{aligned} \tag{B.17}$$

Finally, the anisotropic contribution $\mathcal{I}_{W_{\boldsymbol{f}_0\boldsymbol{s}_0}^{\mathrm{ani}}}$ can be obtained as

$$\begin{aligned}
\mathcal{I}_{W_{\boldsymbol{f}_0\boldsymbol{s}_0}^{\mathrm{ani}}} &= \left(2b_{fs}I_{8,\boldsymbol{f}_0\boldsymbol{s}_0}^2 + 1\right)a_{fs}e^{b_{fs}I_{4,\boldsymbol{f}_0\boldsymbol{s}_0}^2}((\boldsymbol{u}\cdot\boldsymbol{F}_{\boldsymbol{x}}\boldsymbol{f}_0)(\boldsymbol{V}\cdot\boldsymbol{s}_0) + (\boldsymbol{u}\cdot\boldsymbol{F}_{\boldsymbol{x}}\boldsymbol{s}_0)(\boldsymbol{V}\cdot\boldsymbol{f}_0))^2 \\
&\quad + 2a_{fs}e^{b_{fs}I_{8,\boldsymbol{f}_0\boldsymbol{s}_0}^2}I_{8,\boldsymbol{f}_0\boldsymbol{s}_0}(\boldsymbol{u}\cdot\boldsymbol{u})(\boldsymbol{V}\cdot\boldsymbol{f}_0)(\boldsymbol{V}\cdot\boldsymbol{s}_0) \\
&\geq -2a_{fs}e^{b_{fs}I_{8,\boldsymbol{f}_0\boldsymbol{s}_0}^2}I_{8,\boldsymbol{f}_0\boldsymbol{s}_0}(\boldsymbol{u}\cdot\boldsymbol{u})|(\boldsymbol{V}\cdot\boldsymbol{f}_0)(\boldsymbol{V}\cdot\boldsymbol{s}_0)|.
\end{aligned} \tag{B.18}$$

As a result, given the unconditional positiveness of $\mathcal{I}_{\hat{W}}$, $\mathcal{I}_U$, $\mathcal{I}_{W_{\boldsymbol{f}_0}^{\mathrm{ani}}}$ and $\mathcal{I}_{W_{\boldsymbol{s}_0}^{\mathrm{ani}}}$, the total ellipticity indicator $\mathcal{I}_W$ can be written as

$$\mathcal{I}_W \geq -2a_{fs}e^{b_{fs}I_{8,\boldsymbol{f}_0\boldsymbol{s}_0}^2}I_{8,\boldsymbol{f}_0\boldsymbol{s}_0}(\boldsymbol{u}\cdot\boldsymbol{u})|(\boldsymbol{V}\cdot\boldsymbol{f}_0)(\boldsymbol{V}\cdot\boldsymbol{s}_0)|. \tag{B.19}$$

Alternatively, if the Macauly brackets are not considered, the anisotropic contributions $\mathcal{I}_{W_{\boldsymbol{f}_0}^{\text{ani}}}$ and $\mathcal{I}_{W_{\boldsymbol{s}_0}^{\text{ani}}}$ are

$$
\begin{aligned}
\mathcal{I}_{W_{\boldsymbol{f}_0}^{\text{ani}}} &= 4\left(2b_f\left(I_{4,\boldsymbol{f}_0}-1\right)^2+1\right)a_f e^{b_f\left(I_{4,\boldsymbol{f}_0}-1\right)^2}\left(\boldsymbol{u}\cdot\boldsymbol{F_x}\boldsymbol{f}_0\right)^2\left(\boldsymbol{V}\cdot\boldsymbol{f}_0\right)^2 \\
&\quad + 2a_f e^{b_f\left(I_{4,\boldsymbol{f}_0}-1\right)^2}\left(I_{4,\boldsymbol{f}_0}-1\right)\left(\boldsymbol{u}\cdot\boldsymbol{u}\right)\left(\boldsymbol{V}\cdot\boldsymbol{f}_0\right)^2 \\
&\geq -2a_f e^{b_f\left(I_{4,\boldsymbol{f}_0}-1\right)^2}\left|\left(I_{4,\boldsymbol{f}_0}-1\right)\right|\left(\boldsymbol{u}\cdot\boldsymbol{u}\right)\left(\boldsymbol{V}\cdot\boldsymbol{f}_0\right)^2 \\
\mathcal{I}_{W_{\boldsymbol{s}_0}^{\text{ani}}} &= 4\left(2b_s\left(I_{4,\boldsymbol{s}_0}-1\right)^2+1\right)a_s e^{b_s\left(I_{4,\boldsymbol{s}_0}-1\right)^2}\left(\boldsymbol{u}\cdot\boldsymbol{F_x}\boldsymbol{s}_0\right)^2\left(\boldsymbol{V}\cdot\boldsymbol{s}_0\right)^2 \\
&\quad + 2a_s e^{b_f\left(I_{4,\boldsymbol{s}_0}-1\right)^2}\left(I_{4,\boldsymbol{s}_0}-1\right)\left(\boldsymbol{u}\cdot\boldsymbol{u}\right)\left(\boldsymbol{V}\cdot\boldsymbol{s}_0\right)^2 \\
&\geq -2a_s e^{b_s\left(I_{4,\boldsymbol{s}_0}-1\right)^2}\left|\left(I_{4,\boldsymbol{s}_0}-1\right)\right|\left(\boldsymbol{u}\cdot\boldsymbol{u}\right)\left(\boldsymbol{V}\cdot\boldsymbol{s}_0\right)^2.
\end{aligned}
\tag{B.20}
$$

The total contribution $\mathcal{I}_W$ when not considering the Macauly brackets is

$$
\begin{aligned}
\mathcal{I}_W &= -2a_{fs}e^{b_{fs}I_{8,\boldsymbol{f}_0\boldsymbol{s}_0}^2}I_{8,\boldsymbol{f}_0\boldsymbol{s}_0}\left(\boldsymbol{u}\cdot\boldsymbol{u}\right)\left|\left(\boldsymbol{V}\cdot\boldsymbol{f}_0\right)\left(\boldsymbol{V}\cdot\boldsymbol{s}_0\right)\right|. \\
&\quad - 2a_f e^{b_s\left(I_{4,\boldsymbol{f}_0}-1\right)^2}\left|\left(I_{4,\boldsymbol{f}_0}-1\right)\right|\left(\boldsymbol{u}\cdot\boldsymbol{u}\right)\left(\boldsymbol{V}\cdot\boldsymbol{f}_0\right)^2 \\
&\quad - 2a_s e^{b_s\left(I_{4,\boldsymbol{s}_0}-1\right)^2}\left|\left(I_{4,\boldsymbol{s}_0}-1\right)\right|\left(\boldsymbol{u}\cdot\boldsymbol{u}\right)\left(\boldsymbol{V}\cdot\boldsymbol{s}_0\right)^2.
\end{aligned}
\tag{B.21}
$$

The larger number of terms in (B.21) as opposed to (B.18) leads therefore in general to a model which is more prone for loss of ellipticity, specially when fibres $\boldsymbol{f}_0$ and $\boldsymbol{s}_0$ are contracted, namely $I_{4,\boldsymbol{f}_0} < 0$ and $I_{4,\boldsymbol{s}_0} < 0$.

References

[1] A. Bueno-Orovio, E. M. Cherry, F. H. Fenton, Minimal model for human ventricular action potentials in tissue, Journal of Theoretical Biology 253 (2008) 544–560.

[2] K. ten Tusscher, D. Noble, P. Noble, A. Panfilov, A model for human ventricular tissue, American Journal of Physiology-Heart and Circulatory Physiology 286 (2004) H1573–H1589.

[3] J. Bonet, A. J. Gil, R. Ortigosa, A computational framework for polyconvex large strain elasticity, Computer Methods in Applied Mechanics and Engineering 283 (2015) 1061–1094.

[4] World Health Organization, Hearts: Technical package for cardiovascular disease management in primary health care (2016).

[5] E. Wilkins, L. Wilson, K. Wickramasinghe, P. Bhatnagar, J. Leal, R. Luengo-Fernandez, R. Burns, M. Rayner, N. Townsend, European cardiovascular disease statistics (2017).

[6] D. Mozaffarian, E. J. Benjamin, A. S. Go, D. K. Arnett, M. J. Blaha, M. Cushman, S. R. Das, S. de Ferranti, J. P. Després, H. J. Fullerton, et al., Heart disease and stroke statistics, Circulation 133 (2016) e38–e360.

[7] G. J. Tortora, B. H. Derrickson, Principles of anatomy and physiology, John Wiley & Sons, 2008.

[8] E. Hsu, A. Muzikant, S. Matulevicius, R. Penland, C. Henriquez, Magnetic resonance myocardial fiber-orientation mapping with direct histological correlation, American Journal of Physiology-Heart and Circulatory Physiology 274 (1998) H1627–H1634.

[9] A. Nagler, C. Bertoglio, M. Gee, W. Wall, Personalization of cardiac fiber orientations from image data using the unscented kalman filter, in: International Conference on Functional Imaging and Modeling of the Heart, Springer, pp. 132–140.

[10] S. Rossi, T. Lassila, R. Ruiz-Baier, A. Sequeira, A. Quarteroni, Thermodynamically consistent orthotropic activation model capturing ventricular systolic wall thickening in cardiac electromechanics, European Journal of Mechanics-A/Solids 48 (2014) 129–142.

[11] H. Lombaert, J. M. Peyrat, P. Croisille, S. Rapacchi, L. Fanton, F. Cheriet, P. Clarysse, I. Magnin, H. Delingette, N. Ayache, Human atlas of the cardiac fiber architecture: study on a healthy population, IEEE Transactions on Medical Imaging 31 (2012) 1436–1447.

[12] S. Göktepe, E. Kuhl, Electromechanics of the heart: a unified approach to the strongly coupled excitation–contraction problem, Computational Mechanics 45 (2010) 227–243.

[13] J. Wong, E. Kuhl, Generating fibre orientation maps in human heart models using Poisson interpolation, Computer Methods in Biomechanics and Biomedical Engineering 17 (2014) 1217–1226.

[14] J. Vossoughi, R. N. Vaishnav, D. J. Patel, Compressibility of the myocardial tissue, Advances in Bioengineering (1980) 45–48.

[15] F. Yin, C. Chan, R. M. Judd, Compressibility of perfused passive myocardium, American Journal of Physiology-Heart and Circulatory Physiology 271 (1996) H1864–H1870.

[16] T. A. Quinn, P. Kohl, Combining wet and dry research: experience with model development for cardiac mechano-electric structure-function studies, Cardiovascular Research 97 (2013) 601–611.

[17] O. Gültekin, G. Sommer, G. A. Holzapfel, An orthotropic viscoelastic model for the passive myocardium: continuum basis and numerical treatment, Computer Methods in Biomechanics and Biomedical Engineering 19 (2016) 1647–1664.

[18] H. Demiray, On the constitutive equations of biological materials, Journal of Applied Mechanics 42 (1975) 242–243.

[19] J. Humphrey, R. Strumpf, F. Yin, Determination of a constitutive relation for passive myocardium: I. A new functional form, Journal of Biomechanical Engineering 112 (1990) 333–339.

[20] B. Smaill, P. Hunter, Structure and function of the diastolic heart: material properties of passive myocardium, in: Theory of Heart, Springer, 1991, pp. 1–29.

[21] Y. C. Fung, Biomechanics: Mechanical properties of living tissues, Springer Science & Business Media, 2013.

[22] J. M. Guccione, A. D. McCulloch, Finite element modeling of ventricular mechanics, in: Theory of Heart, Springer, 1991, pp. 121–144.

[23] K. D. Costa, J. W. Holmes, A. D. McCulloch, Modelling cardiac mechanical properties in three dimensions, Philosophical Transactions of the Royal Society of London A: Mathematical, Physical and Engineering Sciences 359 (2001) 1233–1250.

[24] G. A. Holzapfel, R. W. Ogden, Constitutive modelling of passive myocardium: a structurally based framework for material characterization, Philosophical Transactions of the Royal Society of London A: Mathematical, Physical and Engineering Sciences 367 (2009) 3445–3475.

[25] J. E. Marsden, T. J. R. Hughes, Mathematical foundations of elasticity, 1994.

[26] J. M. Ball, Convexity conditions and existence theorems in nonlinear elasticity, Archive for Rational Mechanics and Analysis 63 (1976) 337–403.

[27] J. M. Ball, Energy-minimising configurations in nonlinear elasticity, Archive for Rational Mechanics and Analysis 63 (1976) 337–403.

[28] J. M. Ball, Geometry, Mechanics and Dynamics, Springer, pp. 3–59.

[29] J. Schröder, P. Neff, Invariant formulation of hyperelastic transverse isotropy based on polyconvex free energy functions, International Journal of Solids and Structures 40 (2003) 401–445.

[30] J. Schröder, P. Neff, D. Balzani, A variational approach for materially stable anisotropic hyperelasticity, International Journal of Solids and Structures 42 (2005) 4352–4371.

[31] R. Ortigosa, A. J. Gil, J. Bonet, C. Hesch, A computational framework for polyconvex large strain elasticity for geometrically exact beam theory, Computational Mechanics (2015).

[32] J. Bonet, A. J. Gil, C. H. Lee, M. Aguirre, R. Ortigosa, A first order hyperbolic framework for large strain computational solid dynamics - Part I: Total Lagrangian isothermal elasticity, Computer Methods in Applied Mechanics and Engineering 283 (2015) 689–732.

[33] J. Bonet, A. J. Gil, R. Ortigosa, On a tensor cross product based formulation of large strain solid mechanics, International Journal of Solids and Structures 84 (2016) 49–63.

[34] A. L. Hodgkin, A. F. Huxley, Propagation of electrical signals along giant nerve fibres, Proceedings of the Royal Society of London. Series B, Biological Sciences (1952) 177–183.

[35] N. A. Trayanova, J. J. Rice, Cardiac electromechanical models: from cell to organ, Frontiers in Physiology 2 (2011).

[36] L. Tung, A bidomain model for describing ischemic myocardial DC potentials., Ph.D. thesis, Massachusetts Institute of Technology, 1978.

[37] B. J. Roth, J. P. Wikswo, A bidomain model for the extracellular potential and magnetic field of cardiac tissue, IEEE Transactions on Biomedical Engineering (1986) 467–469.

[38] R. M. Bordas, K. Gillow, D. Gavaghan, B. Rodríguez, D. Kay, A bidomain model of the ventricular specialized conduction system of the heart, SIAM Journal on Applied Mathematics 72 (2012) 1618–1643.

[39] L. J. Leon, B. M. Horáček, Computer model of excitation and recovery in the anisotropic myocardium: I. rectangular and cubic arrays of excitable elements, Journal of Electrocardiology 24 (1991) 1–15.

[40] S. Göktepe, S. Acharya, J. Wong, E. Kuhl, Computational modeling of passive myocardium, International Journal for Numerical Methods in Biomedical Engineering 27 (2011) 1–12.

[41] B. Baillargeon, N. Rebelo, D. D. Fox, R. L. Taylor, E. Kuhl, The living heart project: a robust and integrative simulator for human heart function, European Journal of Mechanics-A/Solids 48 (2014) 38–47.

[42] M. Potse, B. Dubé, J. Richer, A. Vinet, R. M. Gulrajani, A comparison of monodomain and bidomain reaction-diffusion models for action potential propagation in the human heart, IEEE Transactions on Biomedical Engineering 53 (2006) 2425–2435.

[43] R. FitzHugh, Mathematical models of threshold phenomena in the nerve membrane, The Bulletin of Mathematical Biophysics 17 (1955) 257–278.

[44] F. Fenton, A. Karma, Vortex dynamics in three-dimensional continuous myocardium with fiber rotation: filament instability and fibrillation, Chaos: An Interdisciplinary Journal of Nonlinear Science 8 (1998) 20–47.

[45] R. R. Aliev, A. V. Panfilov, A simple two-variable model of cardiac excitation, Chaos, Solitons & Fractals 7 (1996) 293–301.

[46] C. H. Luo, Y. Rudy, A dynamic model of the cardiac ventricular action potential. ii. afterdepolarizations, triggered activity, and potentiation., Circulation Research 74 (1994) 1097–1113.

[47] V. Iyer, R. Mazhari, R. L. Winslow, A computational model of the human left-ventricular epicardial myocyte, Biophysical Journal 87 (2004) 1507–1525.

[48] L. Priebe, D. J. Beuckelmann, Simulation study of cellular electric properties in heart failure, Circulation Research 82 (1998) 1206–1223.

[49] K. H. ten Tusscher, A. V. Panfilov, Alternans and spiral breakup in a human ventricular tissue model, American Journal of Physiology-Heart and Circulatory Physiology 291 (2006) H1088–H1100.

[50] L. A. Taber, R. Perucchio, Modeling heart development, Journal of Elasticity 61 (2000) 165–198.

[51] M. P. Nash, A. V. Panfilov, Electromechanical model of excitable tissue to study reentrant cardiac arrhythmias, Progress in Biophysics and Molecular Biology 85 (2004) 501–522.

[52] J. Wong, S. Göktepe, E. Kuhl, Computational modeling of chemo-electro-mechanical coupling: A novel implicit monolithic finite element approach, International Journal for Numerical Methods in Biomedical Engineering 29 (2013) 1104–1133.

[53] J. Wong, S. Göktepe, E. Kuhl, Computational modeling of electrochemical coupling: a novel finite element approach towards ionic models for cardiac electrophysiology, Computer Methods in Applied Mechanics and Engineering 200 (2011) 3139–3158.

[54] M. Aguirre, A. J. Gil, J. Bonet, A. A. Carreño, A vertex centred finite volume Jameson-Schmidt-Turkel (JST) algorithm for a mixed conservation formulation in solid dynamics, Journal of Computational Physics 259 (2014) 672–699.

[55] G. Scovazzi, B. Carnes, X. Zeng, A simple, stable and accurate tetrahedral finite element for transient, nearly incompressible, linear and nonlinear elasticity: A dynamic variational multiscale approach, International Journal for Numerical Methods in Engineering (2015).

[56] M. Cervera, M. Chiumenti, R. Codina, Mixed stabilized finite element methods in nonlinear solid mechanics: Part I: Formulation, Computer Methods in Applied Mechanics and Engineering 199 (2010) 2559–2570.

[57] T. Elguedj, Y. Bazilevs, V. Calo, T. Hughes, B-bar and F-bar projection methods for nearly incompressible linear and non-linear elasticity and plasticity using higher-order nurbs elements, Computer Methods in Applied Mechanics and Engineering 197 (2008) 2732–2762.

[58] A. J. Gil, R. Ortigosa, A new framework for large strain electromechanics based on convex multi-variable strain energies: variational formulation and material characterisation, Computer Methods in Applied Mechanics and Engineering 302 (2016) 293–328.

[59] R. Ortigosa, A. J. Gil, A new framework for large strain electromechanics based on convex multi-variable strain energies: Conservation laws, hyperbolicity and extension to electro-magneto-mechanics, Computer Methods in Applied Mechanics and Engineering 309 (2016) 202–242.

[60] R. Ortigosa, A. J. Gil, A new framework for large strain electromechanics based on convex multi-variable strain energies: Finite Element discretisation and computational implementation, Computer Methods in Applied Mechanics and Engineering 302 (2016) 329–360.

[61] R. de Boer, Vektor- und Tensorrechnung für Ingenieure, Springer-Verlag, 1982.

[62] S. Rossi, R. Ruiz-Baier, L. F. Pavarino, A. Quarteroni, Orthotropic active strain models for the numerical simulation of cardiac biomechanics, International Journal for Numerical Methods in Biomedical Engineering 28 (2012) 761–788.

[63] M. P. Nash, P. J. Hunter, Computational mechanics of the heart, Journal of Elasticity and the Physical Science of Solids 61 (2000) 113–141.

[64] P. Flory, Thermodynamic relations for high elastic materials., Transaction of the Faraday Society 57 (1961) 829–838.

[65] C. Sansour, On the physical assumptions underlying the volumetric-isochoric split and the case of anisotropy, European Journal of Mechanics-A/Solids 27 (2008) 28–39.

[66] D. Nolan, A. Gower, M. Destrade, R. Ogden, J. McGarry, A robust anisotropic hyperelastic formulation for the modelling of soft tissue, Journal of the mechanical behavior of biomedical materials 39 (2014) 48–60.

[67] A. N. Annaidh, M. Destrade, M. Gilchrist, J. Murphy, Deficiencies in numerical models of anisotropic nonlinearly elastic materials, Biomechanics and modeling in mechanobiology 12 (2013) 781–791.

[68] J. M. Ball, F. Murat, $W^{1,p}$-quasiconvexity and variational problems for multiple integrals, Journal of Functional Analysis 58 (1984) 225–253.

[69] G. A. Holzapfel, R. W. Ogden, On the tension–compression switch in soft fibrous solids, European Journal of Mechanics-A/Solids 49 (2015) 561–569.

[70] K. Li, R. W. Ogden, G. A. Holzapfel, Computational method for excluding fibers under compression in modeling soft fibrous solids, European Journal of Mechanics-A/Solids 57 (2016) 178–193.

[71] A. Kamgoué, J. Ohayon, Y. Usson, L. Riou, P. Tracqui, Quantification of cardiomyocyte contraction based on image correlation analysis, Cytometry Part A 75 (2009) 298–308.

[72] J. Strobeck, E. Sonnenblick, Myocardial contractile properties and ventricular performance, The Heart and Cardiovascular System (1986) 31–49.

[73] A. J. Gil, C. H. Lee, J. Bonet, M. Aguirre, A stabilised Petrov-Galerkin formulation for linear tetrahedral elements in compressible, nearly incompressible and truly incompressible fast dynamics, Computer Methods in Applied Mechanics and Engineering 276 (2014) 659–690.

[74] A. J. Gil, C. H. Lee, J. Bonet, R. Ortigosa, A first order hyperbolic framework for large strain computational solid dynamics - Part II: Total Lagrangian compressible, nearly incompressible and truly incompressible elasticity, Computer Methods in Applied Mechanics and Engineering 300 (2016) 146–181.

[75] M. Crouzeix, P. A. Raviart, Conforming and nonconforming finite element methods for solving the stationary stokes equations I, Revue Française d'Automatique Informatique Recherche Opérationnelle. Mathématique 7 (1973) 33–75.

[76] F. Bertrand, M. Gadbois, P. Tanguy, Tetrahedral elements for fluid flow, International Journal for Numerical Methods in Engineering 33 (1992) 1251–1267.

[77] R. Ortigosa, A. J. Gil, C. H. Lee, A computational framework for large strain nearly and truly incompressible electromechanics based on convex multi-variable strain energies, Computer Methods in Applied Mechanics and Engineering 310 (2016) 297–334.

[78] S. Land, V. Gurev, S. Arens, C. M. Augustin, L. Baron, R. Blake, C. Bradley, S. Castro, A. Crozier, M. Favino, et al., Verification of cardiac mechanics software: Benchmark problems and solutions for testing active and passive material behaviour, in: Proc. R. Soc. A, volume 471, The Royal Society, p. 20150641.

[79] J. M. Guccione, A. D. McCulloch, L. Waldman, et al., Passive material properties of intact ventricular myocardium determined from a cylindrical model, Journal of Biomechanical Engineering 113 (1991) 42–55.

[80] C. J. Chuong, Y. C. Fung, Residual stress in arteries, in: Frontiers in biomechanics, Springer, 1986, pp. 117–129.